Synthesis and Characterization of Magnetic Nanowires

Prepared by Chemical Vapor Deposition

A Dissertation Presented for the
Doctor of Philosophy
Degree
The University of Tennessee, Knoxville

Siwei Tang
May 2014

DEDICATION

To my wife, my parents, my parents in law and my daughter

ACKNOWLEDGEMENTS

First, I would like to thank my mentors and advisors Dr. David G Mandrus and Dr. Zheng Gai for their priceless guidance, inspiring discussion, and constant support and encouragement during my graduate career. The excellent examples they set inspired me to always do better. I would also like to thank my dissertation committee members, Dr. Bin Hu and Dr. David C. Joy for giving their valuable time to read and provide advice on my dissertation.

Second, I would like to thank several of my colleagues who helped me with my research. Dr. Ivan I. Kravchenko shared with me his extensive experience and knowledge of nanofabrication. Dr Jane Howe, Dr. Miao-Fang Chi, and Dr. Cheng Ma helped with transmission electron microscopy measurements. Jieyu Yi gave me valuable insights during many discussions. Dr. Guixin Cao helped me with several magnetic measurements, Dr. Jiaqiang Yan gave me advice on vapor growth. I have enjoyed and benefited from working with them. Thanks to Ling Li and Hui Yang for their valuable friendship. Dr. Yueying Wu helped with laser irradiation of some of my samples. Peizhi Liu and Mengkun Tian provided valuable discussions of TEM data. Dr. Zac Ward helped with transport measurements. Dr. Dale Hensley, Dr. Jihua Chen, Dr. Andrew Payzant, Dr. Mingwei Lin, Dr. Kai Xiao, Dr. Anping Li, Dr. Qing Li, Dr. Minghu Pan, Dr. Liang Qiao and Dr Veerle M. Keppens helped with data analysis. I appreciate the people who work in the Center for Nanophase Materials Sciences at Oak Ridge National Laboratory who were always helpful and friendly.

Lastly, I would like to thank my wife, my parents, my daughter, and my parents-in-law. I often gain encouragement and confidence after talking with them when I am depressed and lonely. My wife Tian Tang sacrificed her job in China to stay with me in the U.S. for almost four years. And she brings me a precious gift, my small angel, my daughter Yuxi Tang. I am very appreciative of the happiness brought by my daughter.

ABSTRACT

Various metal silicide and germanide magnetic nanowires were synthesized using a home-built CVD [chemical vapor deposition] system. The morphology, composition, and magnetic properties of the nanowires were studied and correlated with growth parameters such as temperature, pressure, time, and source-substrate distance.

One of the compositions targeted for synthesis was MnSi [manganese silicide]. In bulk, this material orders helimagnetically at T_c [curie temperature] = 30K, with a helical pitch of about 20 nm. After extensive study, we learned that the thickness of the silicon dioxide layer on the substrate is a critical parameter for the growth of MnSi nanowires. An oxide assisted one-dimensional growth mechanism was proposed. A growth diagram was created that shows the effect of various growth parameters on the products. The nanowires were characterized magnetically in a SQUID [superconducting quantum interference device] magnetometer using AC [alternating current] susceptibility. These measurements confirmed helimagnetic ordering and skyrmion lattice formation in the nanowires.

Another composition targeted for synthesis was $FeGe_2$ [iron digermanide]. In bulk, $FeGe_2$ undergoes a spin density wave transition at 289 K. Nanowires of $FeGe_2$ have not been previously reported. We were able to grow $FeGe_2$ nanowires on a Ge substrate. The $FeGe_2$ nanowires were identified by selected area diffraction using a transmission electron microscope. The growth direction was determined to be

[110]. $FeGe_2$ nanowires were integrated into four-probe nanodevices, which were fabricated through an e-beam lithography system via beam dose correction and a double-layer geometry. The combined magnetic and electronic transport measurements show that while the antiferromagnetic spin density wave is still present along the $FeGe_2$ nanowire long axis, ferromagnetism was identified in other directions.

TABLE OF CONTENTS

CHAPTER 1 INTRODUCTION 1
CHAPTER 2 THEORETICAL PRINCIPLES AND BACKGROUND 6
2.1 Theory of nanowires prepared with the vapor method 6
2.2 Helimagnetic structure and skyrmion 9
2.2.1 Theory of helimagnetic structure 9
2.2.2 Skyrmion and its particularity 14
2.2.3 Skyrmion and domain wall motion 23
2.3 Spin density wave 28
2.3.1 Formation of spin density wave 28
2.3.2 Verification of spin density wave 31
CHAPTER 3 DESIGN OF THE CVD SYSTEM FOR NANOWIRE GROWTH 34
3.1 Nanostructure prepared in chemical vapor deposition with leaks 34
3.2 CVD System setup 41
3.2.1 Tube furnace heating curve 43
3.2.2 Pressure gauge calibration 46
3.2.3 Flow meter calibration 48
3.2.4 Oxide layer growth on silicon wafer 48
3.3 Characterization Tools 48
3.3.1 Morphology, structure and composition 48
3.3.2 Magnetic and electronic properties 51
3.3.3 Device fabrication 54
CHAPTER 4 OPTIMIZATION OF THE E-BEAM NANOFABRICATION PROCESS FOR NANODEVICES 58
4.1 Standard procedure for device fabrication via e-beam lithography 58
4.1.1 Preparation of transferring wafer 58
4.1.2 Transferring and measuring nanowires, and designing electrodes 59
4.1.3 E-beam writing 61
4.1.4 Deposit electrodes and lift off 62
4.2 Problem in the process 65
4.3 E-beam energy dose correction and double layers of e-beam resist 65
CHAPTER 5 SYNTHESIS AND CHARACTERIZATION OF METAL SILICIDE NANOWIRES VIA OXIDE-ASSISTED GROWTH 72
5.1 Previous preparation of MnSi nanowires 72

5.2 Principle of oxide-layer assisted growth of silicide nanowires 75
5.3 Experiment details and characterization of MnSi nanowires 77
5.4 Magnetic measurement and verification of skyrmion 89
CHAPTER 6 SYNTHESIS AND CHARACTERIZATION OF IRON GERMANIDE NANOWIRES 95
6.1 Nanostructures synthesis in initial stage 95
6.2 Structure verification and chemical composition of $FeGe_2$ nanowires 104
6.3 Transport properties and magnetic measurement of $FeGe_2$ nanowires 111
CHAPTER 7 OTHER NANOWIRES PREPARED BY CVD 121
7.1 Fe_2Si and Cr_5Si_3 nanowires 121
7.2 Synthesis of $Fe_{2.5}Ge$ nanowires 124
7.3 Fe_3Ge nanowires 127
CHAPTER 8 CONCLUSION 129
REFERENCES 131
VITA 137

LIST OF TABLES

Table 1 Magnetic characteristic length scales.....4
Table 2 Composition of Mn:Si in samples prepared by atmosphere CVD 36

LIST OF FIGURES

Figure 1 The importance of studying nanomagnetism. 2
Figure 2 Domain wall velocities versus the external field in permalloy nanowires of various diameters [2]..... 5
Figure 3 Temperature and supersaturation ratio competition between one-dimensional and two-dimensional growth. 8
Figure 4 Plot of free energy in left and right hand chiral calculated from quadratic function. 12
Figure 5 (a)Helimagnetic structure with in plane rotation (b) The definition of pitch of helix [23]. 13
Figure 6 (a) Magnetic phase diagram of MnSi [22] (b) Skyrmion is a quantized vortex-like magnetic structure [26]. 16
Figure 7 (A)Neutron diffraction data of the helical magnetic ordering in MnSi single crystal at 27K (B) Hexagonal skyrmion diffraction pattern of MnSi single crystal at 26.5K with field of 0.164T [22]..... 17
Figure 8 (a) “A” phase transition in magnetic moments measurements vs temperature and external field [28] (b) (c)Various magnetic susceptibility vs temperature measured under different fields (d) AC susceptibility versus field [30]. 19
Figure 9 (a) Skyrmion lattice on thin plate of FeGe under Lorentz TEM (b) Size of a single skyrmion [31]. 22
Figure 10 Current-driven domain wall motion [3]. 25
Figure 11 Spin transfer torque at ultra-low current density of MnSi single crystal [34]. 26
Figure 12(a) Charge density wave (b) Spin density wave (c) Comparison of normal metal, CDW and SDW [41]. 30
Figure 13 Conductance measurement of SDW [47]. 32
Figure 14 (a) Resistivity changes when applying current and field along [110], from bottom up each curve represents a temperature: 260, 263.6, 264, 265,266.1,267,268.5,269K (b) Constructed magnetic phase diagram [51]. 33

Figure 15 Different morphologies observed in CVD when leaks are in the system: (a) Three narrow bands (b) Details in narrow bands (c) Details of outermost band with scattered particles (d) Innermost nanowires band. ……35
Figure 16 (a)"Hexagonal roll" structure; (b) Morphology of nanowires prepared in system open to air (c) Details of Mn head with SiO_2 hairs.……39
Figure 17 Nanowires growing around the melted SiO_2.……40
Figure 18 (a)(b)Two geometries of chemical vapor deposition in nanowires' growth, (c) the CVD system's design.……42
Figure 19 Temperature profile vs. position in tube furnace used for CVD.……44
Figure 20 Relationship between displayed Ar pressure and real Ar pressure. ……47
Figure 21 (a) Powder X-ray diffraction (b) Zeiss Merlin VP SEM equipped with EDS (c) Zeiss Libra 120 TEM.……50
Figure 22 (a) SQUID used for magnetic measurements (b) PPMS used for transport properties measurements. ……53
Figure 23 (a) Multiple-speed spin coater (b) Dual electron beam metal evaporator. ……56
Figure 24 JEOL 9300FS 100kV electron beam lithography system.……57
Figure 25 Nanowires transferred in each 31*31 pattern. ……60
Figure 26 (a) Distance from the center of the nanowire to gold marks measured (b) Designed electrodes using Layout software (c) Real PMMA pattern after e-beam exposure.……63
Figure 27 The Procedure of fabricating nanowire devices.……64
Figure 28 (a) Thick nanowire before spin coating (b) Thick nanowire after spin coating (c) Thick nanowire after depositing metal film.……67
Figure 29 Lift-off issue after the metal layer was deposited on the pattern. ……68
Figure 30 (a) Double layers with PMMA in bottom (b) Copolymer in bottom.……69
Figure 31 Four-probe nanowire integrated nanodevice used to measure transport properties.……71
Figure 32 Mn-Si phase diagram [58].……74

Figure 33 (a) Controlled parameter in oxide layer assisted CVD (b)-(e) Morphology comparison of nanowires prepared on substrate with different oxide thicknesses: 100nm, 300nm, 500nm, 1000nm (f)their XRD pattern. 78
Figure 34 (a) Morphology of nanowires prepared under optimized parameters (b)-(e) Chemical composition mapping (f) Mn/Si composition comparison in different samples (g) Mn/Si ratio curves change with oxide thickness. 80
Figure 35 (a) EDX comparison (b) Magnetic measurement on nanowires prepared during different time periods: 40, 80 and 160 mins. 82
Figure 36(a)-(d) Morphology comparison (e)Composition comparison (f) Magnetic measurement on nanowires prepared during different distances from source to substrate: 100, 500 and 1500 μm. 83
Figure 37 (a)-(d)Morphology comparison (e)Composition comparison (f) Magnetic measurement on nanowires prepared during different reaction temperatures: 750, 850, 900 and 950 °C. 84
Figure 38 (a) Mn-Si nanowires growth phase diagram at various temperatures and times (b) Mn-Si nanowires growth phase diagram at various source-substrate distances and times. 86
Figure 39 DC and ac magnetizations of the MnSi nanowires. (a) In and out of the plane anisotropic magnetizations (see text for definition) under DC field of 10 Oe. The kink around 29 K is the signature of helical magnetic. The inset shows the field dependent of the magnetization at 10K. (b) Comparison of the ac susceptibility Re $\boldsymbol{\chi}_{\mathbf{ac}}$(blue), Im $\boldsymbol{\chi}_{\mathbf{ac}}$(red) with the susceptibility μ_0dM/dB calculated from the field dependence magnetization M (purple, right Y axis) at 28K. The isothermal ac susceptibility is as a function of field measured under excitation field of 1 Oe and 8Hz ac magnetic field applied in-plane at 28K. (c) Evolution of the Re $\boldsymbol{\chi}_{\mathbf{ac}}$ approaching from 26 K to T_c 29 K. The blue and red dash-lines are guiding lines for the B_{c1}, B_{c2} and $\mathbf{B}_{\boldsymbol{A1}}^{-}$,$\mathbf{B}_{\boldsymbol{A2}}^{+}$ 90
Figure 40 Fe-Ge phase diagram [77]. 97
Figure 41 (a) 9 nm Cr thin film deposited on Ge wafer (b) Nanoparticles prepared after laser irradiation (c) Diameter of a nanoparticle (d) Nanorod structure growth by direct deposit Cr-FeGe on Cr-Ge wafer at 570°C. 100

Figure 42 (a)SEM image showing morhology of $FeGe_2$ layered structure (b)XRD pattern of thick layer prepared on 700°C and 850°C(760 Torr) and 600°C(1200 Torr)..... 103
Figure 43 Souce-substrate geometry with Ar works as carrier gas 106
Figure 44 (a)Nanowires prepared with the thick $FeGe_2$ layer in the middle. (b)The diamter of $FeGe_2$ nanowire..... 107
Figure 45 Indexed XRD pattern shows the peaks matching $FeGe_2$..... 108
Figure 46 (a) High resolution TEM images of $FeGe_2$ nanowires. The inset is the FFT of HRTEM images (b) Growth direction of nanowires is identified as [110]. The inset is the diffraction pattern with zone axis [001]..... 109
Figure 47 Relative height of iron peak compared to Ge peak along $FeGe_2$ nanowires. 110
Figure 48 (a) Four-probe nanodevice (b) Resistivity measured with a magnetic field of 0 and 6 Telsa. Both of them include a cooling and heating process. 112
Figure 49 Resistivity measurement at 0T cooling from 310K to 10K: Two temperature points (10K and 230K) were chosen to compare magnitudes in two separate constant resistivity ranges (0-180K and 218-237K). Each temperature point has two curves with magnetic field rising from 0-9T and returning to 0T..... 113
Figure 50 Resistivity measurement at 0T cooling from 310K to 10K: Three temperature points (203K, 208K and 246K) were chosen to compare transition in peak resistivity regimes. Each temperature point has two curves with the magnetic field rising and falling. A smooth fit was used to eliminate noises..... 114
Figure 51 (a) The magnetoresistance and magnetic moments reveal two transition temperatures at 205.5K and 252.4K. 115
Figure 52 (a) M-H hysteresis curves at 30K, (b) Enlargement of M-H hysteresis curves from -1500oe to 1500oe. 116
Figure 53 (a) Magnetic-field direction and current-flow direction in transport measurements (b) Magnetic-field direction in magnetic measurement..... 120
Figure 54 (a) Fe_2Si nanowires (b) Cr_5Si_3 nanowires prepared by metal powder deposited on a silicon wafer with an oxide layer..... 122

Figure 55 Composition of nanowires on carbon tape gives the atomic ratio (a) Fe_2Si (b) Cr_5Si_3. 123
Figure 56 $Fe_{2.5}Ge$ Nanowires prepared with less $FeGe_2$ layer in middle..... 125
Figure 57 (a)Peaks of Fe and Ge measured along the nanowires with atomic ratio at 2.5:1 (b) Magnetic moments versus temperature measured on the whole substrate with magnetic field at 1000 oe. 126
Figure 58 (a) Fe_3Ge nanowires prepared on Ge wafer (b) Composition verified by EDX. 128

CHAPTER 1 INTRODUCTION

Over the past 40 years, great achievements have been made in the studying of nanomaterials, including information storage, computing devices, photovoltaics and sensing. [1] The motivation for the exploration in this work is to study the magnetic properties in one-dimensional nanostructures.

The great achievement in nanomagnetism is attributable to their magnetic properties, which are largely different from bulk magnetic materials, even though both materials have the same chemical formula and structure.

The reasons why magnetic properties of those two materials are different are (a) the dimension of nanomaterials is approximately the same as the magnetic characteristic length;(2) nanomaterial's high portion of surface atoms, and (3)nanomaterial's high percentage of defects. [2] The last two reasons are common properties of nanomaterials (Fig 1).

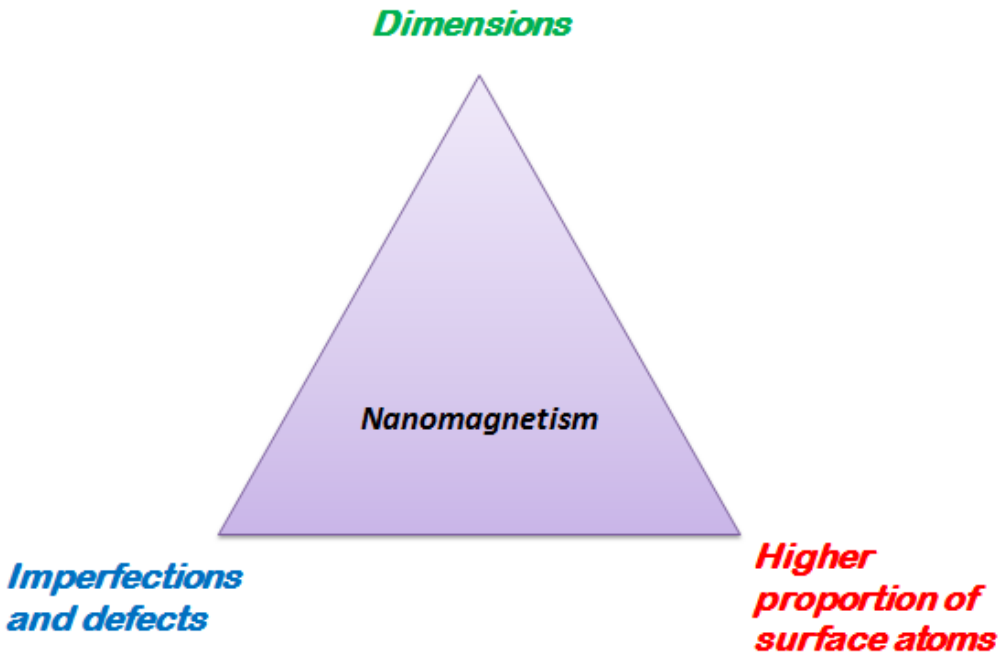


Figure 1 The importance of studying nanomagnetism.

As shown in table 1, almost all of the magnetic characteristic lengths fall in the range of 1-100nm like the domain wall width and the spin diffusion lengths. The question raised here is what will happen when the size of materials is smaller than those characteristic lengths [3] [4] ? Therefore, the purpose of this study is to prepare magnetic nanowires including ferromagnetic nanowires and antiferromagnetic nanowires, which could help with understanding the manipulation of spins in nanowires.

A typical example in Fig 2 shows magnetic domain wall motion in Permalloy nanowires by applying a magnetic field. The velocity is linear with applied field, and the velocity of both the vortex and the transverse domain walls increases with the nanowire's diameter by applying the same magnetic field. Using the diameter to control the velocity shows great potential in electronic applications.

Table 1 Magnetic characteristic length scales

Symbol	Length	Typical scale (nm)
d_a	Interatomic distance (Fe)	$2.5*10^{-1}$
d_{ex}	Range of exchange interaction	$\sim10^{-1}$- ~1
d_{RKKY}	Range of RKKY interaction	$\sim10^{-1}$- ~10
d_c	Domain size	$10\text{-}10^4$
D_{cr}^{spm}	Superparamagnetic critical diameter	~1- $\sim10^2$
D_{cr}	Critical single-domain size	~10- $\sim10^3$
δ_0	Domain wall width	~1- $\sim10^2$
l_{ex}	Exchange length	~1- $\sim10^2$
l_{sd}	Spin diffusion length	~10- $\sim10^2$
λ_{mfp}	Electron mean free path	~1- $\sim10^2$
ζ	Superconducting coherence length	~1- $\sim10^3$
λ_F	Fermi wavelength/metal	$\sim10^{-1}$
λ_F	Fermi wavelength/semiconductor	$\sim10^2$

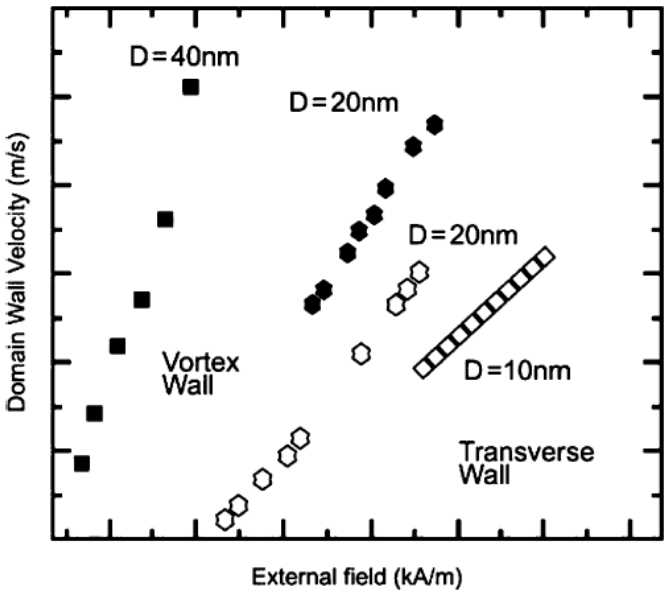


Figure 2 Domain wall velocities versus the external field in permalloy nanowires of various diameters [2].

CHAPTER 2 THEORETICAL PRINCIPLES AND BACKGROUND

Nanostructures were synthesized in many ways, including two strategies: the bottom-up and the top-down. [5] The bottom-up method involves evaporating a precursor's atoms and molecules and then depositing them on the substrate. Methods for assembling a nanostructure from bottom to up include the vapor method and the solution method. In the fabricating a nanodevice, the top-down method is employed to shape nanosize electrodes.

2.1 Theory of nanowires prepared with the vapor method

The vapor-liquid-solid method and vapor-solid method are used commonly in fabricating nanowires. The former often involves a metal catalyst to control growth; the mechanism of the latter is mainly related to the supersaturation ratio. [6–11]

In the vapor-solid method, it is commonly accepted that the two-dimensional nucleation probability on a whisker's surface is:

$$P_N = Bexp(-\frac{\pi\sigma^2}{k^2T^2In\,\alpha})$$

where B-constant

σ-surface energy of a solid whisker

k-Boltzmann constant

T-absolute temperature

α-supersaturation ratio (p/p_0) where p is actual vapor pressure and p_0 is equilibrium vapor pressure corresponding to T. [12,13]

In order to achieve one-dimensional growth, two-dimensional growth should be suppressed, reducing the two-dimensional nucleation in this formula by lowering the temperature and reducing supersaturation ratio α (Fig 3). However, the supersaturation ratio should not be too small so as to have enough material deposited on the substrate. That is,

$$\alpha_{powder}^{3D\ growth} > \alpha_{thin\ film}^{2D\ growth} > \alpha_{nanowire}^{1D\ growth}.$$

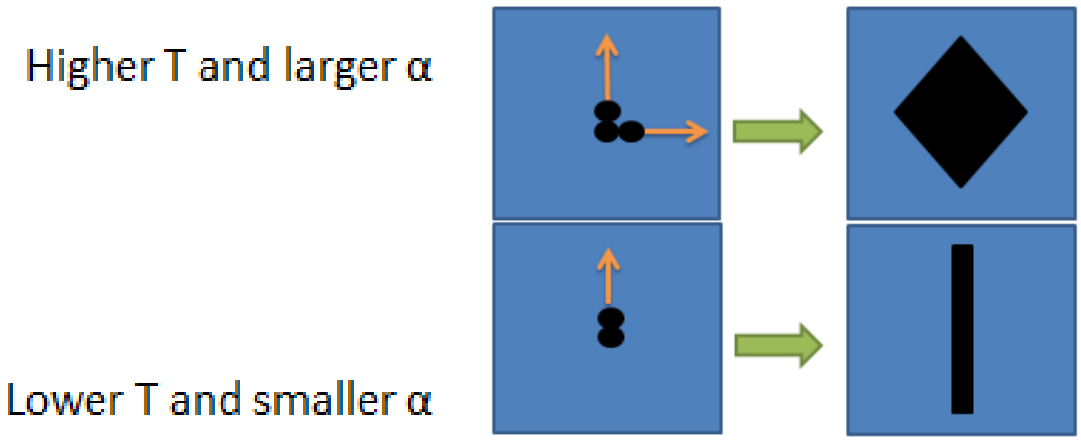


Figure 3 Temperature and supersaturation ratio competition between one-dimensional and two-dimensional growth.

2.2 Helimagnetic structure and skyrmion

2.2.1 Theory of helimagnetic structure

Based on the Landau-Ginzburg equation of free energy in terms of spin density in magnetic materials [14–21]:

$$F(r) = \frac{1}{2}A\left(S_x^2 + S_y^2 + S_z^2\right) + bS \cdot (\nabla \times S) + \frac{1}{2}B_1\left[(\nabla S_x)^2 + \left(\nabla S_y\right)^2 + (\nabla S_z)^2\right] + \frac{1}{2}B_2\left[\left(\frac{\partial S_x}{\partial x}\right)^2 + \left(\frac{\partial S_y}{\partial y}\right)^2 + \left(\frac{\partial S_z}{\partial z}\right)^2\right] + C\left(S_x^2 + S_y^2 + S_z^2\right)^2 + D(S_x^4 + S_y^4 + S_z^4)$$

The first term is the exchange interaction coupling term, resulting in the magnetic moments alignment (ferromagnetism). The second term is the Dzyaloshinsky-Moriya interaction that is trying to twist the magnetic moments; this interaction often occurs in a system that has broken inversing symmetry. The third and fourth terms are additional softening of the magnetization' amplitude. The fifth and sixth terms are spin-orbit coupling anisotropy energy, especially in $P2_13$ space group (B20 structure). [22]

Near T_c, the free energy is generally minimized by periodic structures of the form

$$S(r) = \frac{1}{\sqrt{2}}[S_k \exp(ik \cdot r) + S_k^* \exp(-ik \cdot r)]$$

$$F(k) = \frac{1}{2}A|S_k|^2 + ibk \cdot (S_k \times S_k^*) + \frac{1}{2}B_1 k^2 |S_k|^2 + \frac{1}{2}B_2 (k_x^2 |S_{kx}|^2 + k_y^2 \left|S_{ky}\right|^2 + k_z^2 |S_{kz}|^2)$$

$$S_k = \alpha_k + i\beta_k$$

$$S(r) = \alpha_k \cos(k \cdot r) - \beta_k \sin(k \cdot r)$$

F(k) is minimized when α_k is perpendicular to β_k and $|\alpha_k|=|\beta_k|$ and k is antiparallel to α_k x β_k (b>0)

$B_2 < 0$ k is parallel to (111)

$B_2 > 0$ k is parallel to (100)

$$F(r) = \frac{1}{2}A|S_k|^2 + ibk \cdot (-2\alpha_k \times i\beta_k) + \cdots$$

$$F(r) = \frac{1}{2}A|S_k|^2 + 2bk(|\alpha_k||\beta_k|\sin(\alpha_k \hat{} \beta_k))\cos(k \hat{} (\alpha_k \times \beta_k)) + \cdots$$

$$F(r) = \frac{1}{2}A|S_k|^2 + ibk \cdot (S_k \times S_k^*) + \frac{1}{2}B_1 k^2 |S_k|^2 + \frac{1}{2}B_2 (k_x^2 |S_{kx}|^2 + k_y^2 \left|S_{ky}\right|^2 + k_z^2 |S_{kz}|^2)$$

$$F = \left(\frac{1}{2}A - |b|k\right)|S_k|^2 + (\frac{1}{2}B_1 + \frac{1}{6}B_2)k^2 |S_k|^2$$

which is minimized by

$$k = \frac{|b|}{B_1 + \frac{1}{3}B_2}$$

Based on calculation in Fig 4, the free energy in helimagnets could be plotted versus wave vector k. The free energy clearly has a minimum value on the left and right sides that is correlated to two kinds of chiral structure. [20]

In the helical magnetic structure, magnetic moments in each plane are parallel by exchange interaction coupling but rotate at a constant angle in each plane as a result of the Dzyaloshinsky-Moriya interaction. Then after rotation over many planes, the magnetic moments go back to their original orientation. The distance between the last plane and the original one is called pitch of the helix in helimagnetic materials as is shown in Fig 5. The pitch of the helix is of nanometer size in B20 structure materials (18nm in MnSi, 90 nm in $Fe_{0.5}Co_{0.5}Si$, and 70 nm in FeGe).

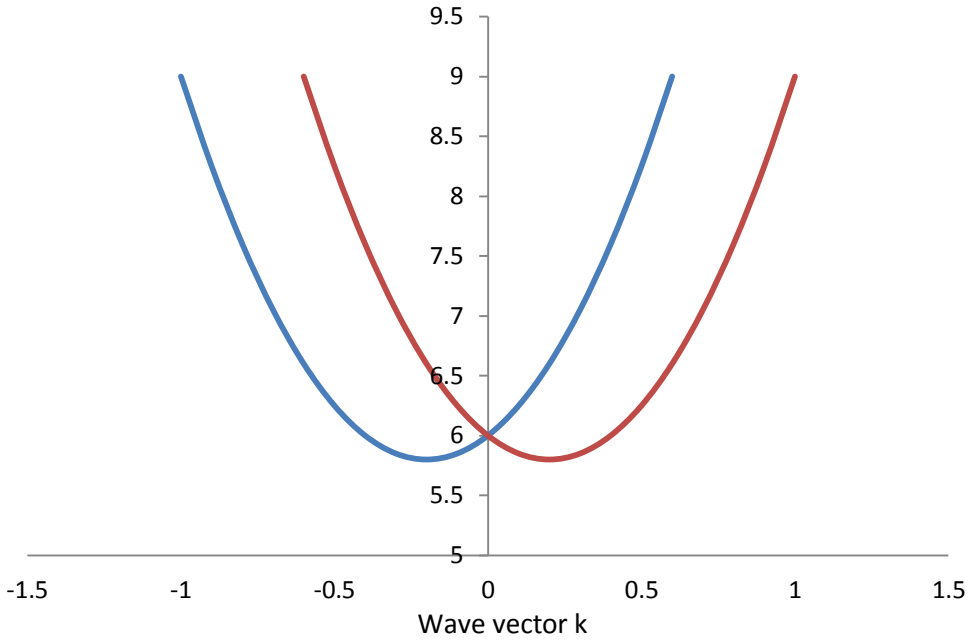


Figure 4 Plot of free energy in left and right hand chiral calculated from quadratic function.

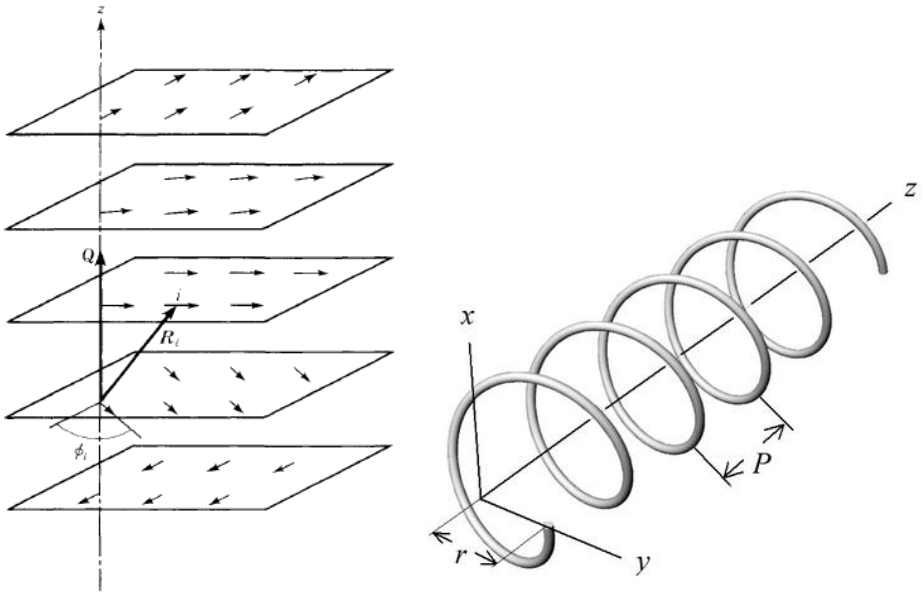


Figure 5 (a)Helimagnetic structure with in plane rotation (b) The definition of pitch of helix [23].

2.2.2 Skyrmion and its particularity

The skyrmion phase is metastable, which is formed from helimagnetic structure. Comparing the energy term of body centered cubic formed from liquid [22]:

$$\sum_{q_1 q_2 q_3} \rho_{q_1} \rho_{q_2} \rho_{q_3} \delta(q_1 + q_2 + q_3)$$

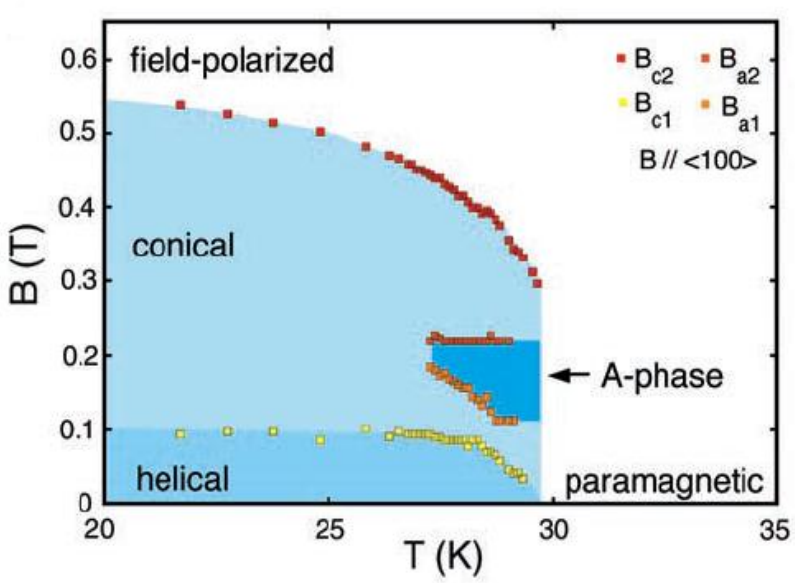
The energy could be maximized by putting $q_1+q_2+q_3$ equals to 0 for $\delta(0)=1$. So with q_1,q_2,q_3 are all moment vectors. They must be rotated 120° from each other because they have the same magnitude. In helimagnetic materials, the same situation could happen:

$$\sum_{q_1 q_2 q_3} (M_f \cdot m_{q_1})(m_{q_2} \cdot m_{q_3}) \delta(q_1 + q_2 + q_3)$$

Thus, the skyrmion formed from the helimagnetic structure could gain energy. So this energy term makes the skyrmion entire hexagonal lattice (Fig 6(b)).

Skyrmion is a quantized vortex-like magnetic structure with center magnetic moments parallel or antiparallel and outermost magnetic moments antiparallel or parallel to the external magnetic field.(Fig 6(b)) Skyrmion is a combination of conical and helical states. [24] Therefore,

in helimagnetic materials, skyrmion is stabilized by a small magnetic field when its temperature is near its magnetic transition point. If the magnetic field is too large, magnetic moments will tilt towards the magnetic field, resulting in the conical state. Then magnetic moments will become field polarized if the field is large enough to align magnetic moments with a magnetic field [25](Fig 6(a)). In neutron scattering, helical states aligning in <111> direction of MnSi could be identified, and the pitch of the helix could be calculated by $p=2\pi/q$ when q is the distance between two <111> spots. After the field is applied, skyrmion shows a hexagonal lattice pattern(Fig 7). [22] Skyrmion's existence is similar to bubble memory, where a thin film of a magnetic material is used to hold small magnetized areas, known as bubbles or domains, each storing one bit of data.



(a)

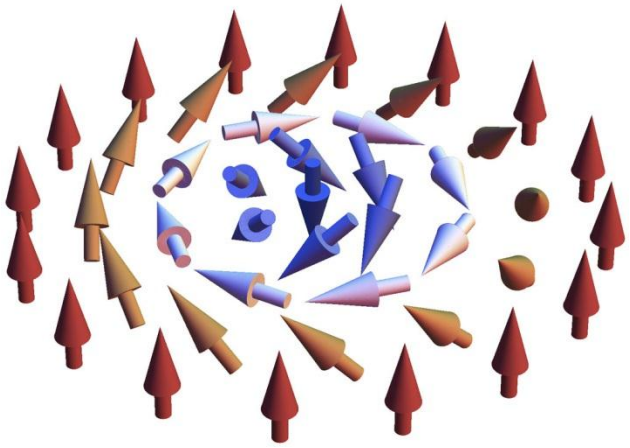


Figure 6 (a) Magnetic phase diagram of MnSi [22] (b) Skyrmion is a quantized vortex-like magnetic structure [26].

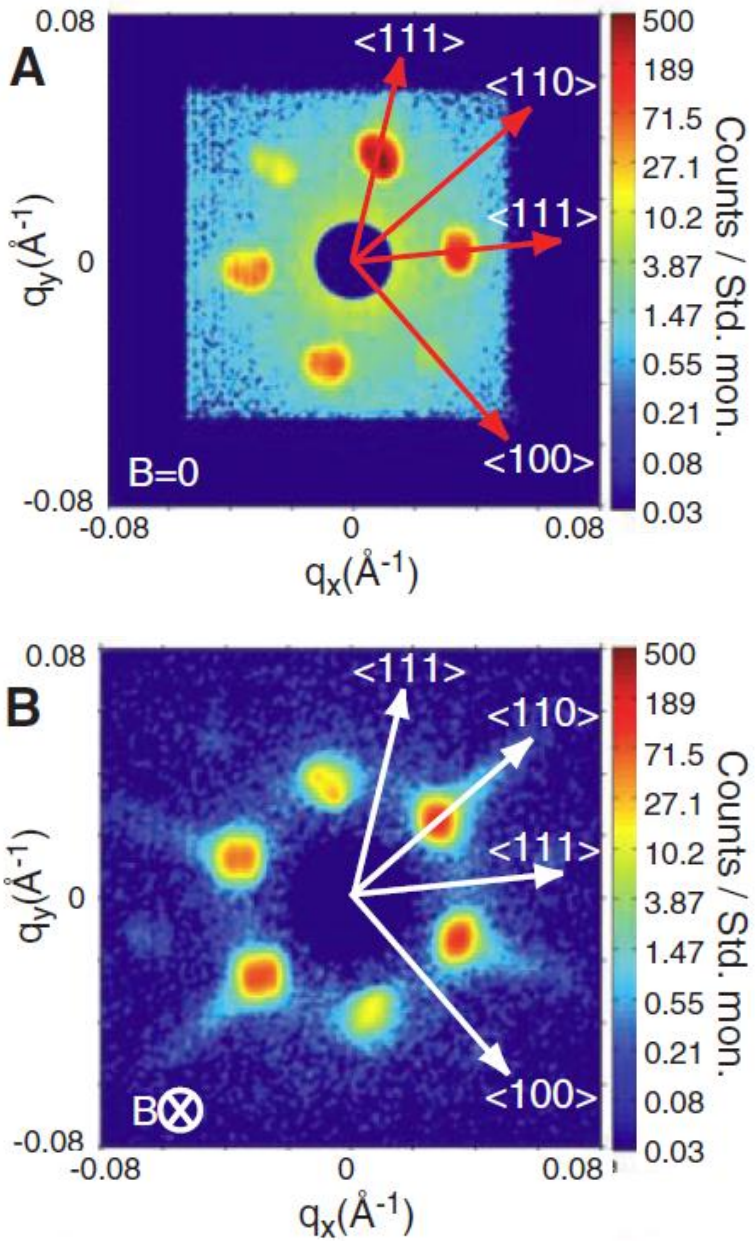
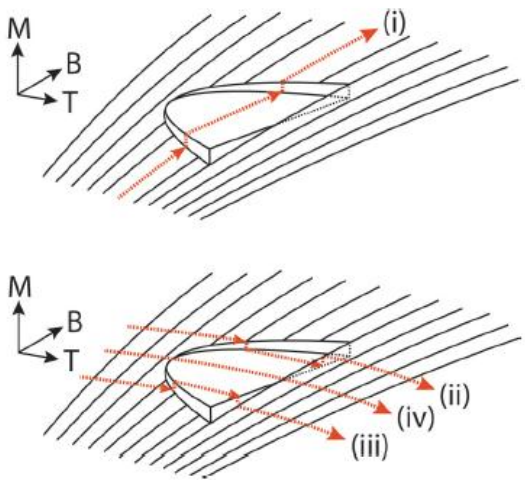


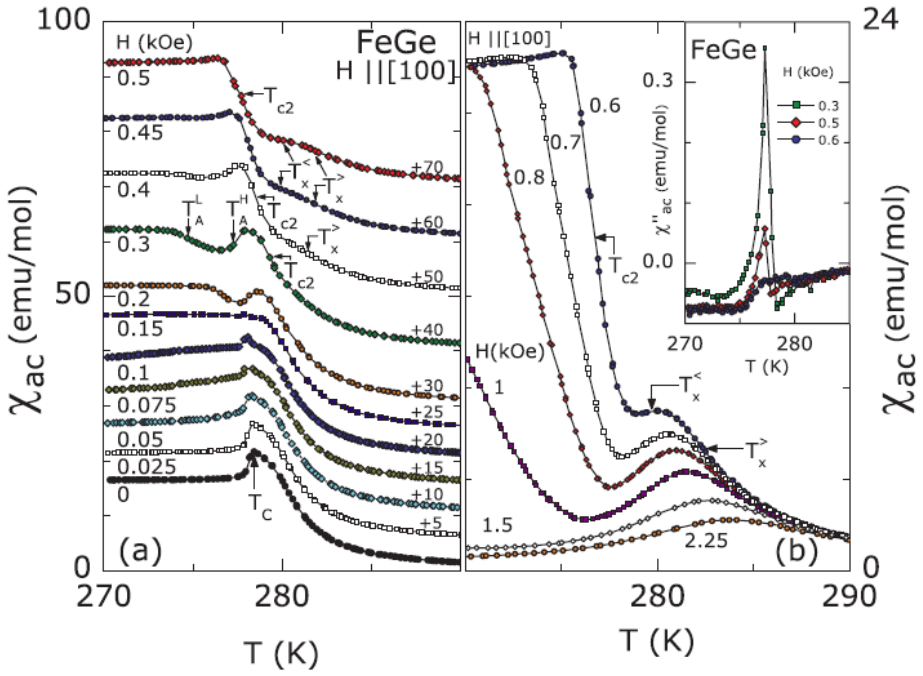
Figure 7 (A)Neutron diffraction data of the helical magnetic ordering in MnSi single crystal at 27K (B) Hexagonal skyrmion diffraction pattern of MnSi single crystal at 26.5K with field of 0.164T [22].

Skyrmion could be characterized using neutron diffraction, Superconducting quantum interference device(SQUID) and Lorentz microscopy TEM. [27] When the magnetization, temperature, and magnetic field are plotted as three axes of a coordinate system, the skyrmion phase could be drawn as a raised plateux (Fig 8(a)) . In the phase boundary, it is discontinuous first order transition [28] and shows a pocket's magnetization. Fig 8(b)(c) Magnetization curves vs temperature with kinks at low field are representative of the helical magnetic phase (Fig 8(d)). In the magnetization curves vs. field, the pocket area between kinks with a small field shows the magnetic structure's boundary. Using multiple points' measurement, AC susceptibility versus field could be plotted at different temperatures close to the transition point. Three-dimensional curves are plotted to reveal the diversification of A-phase, depending on the temperature and the magnetic field. The magnetic phase diagram is also plotted. [29,30] In Lorenz TEM, real images of skyrmion are observed by placing a thin plate of FeGe under an electron beam. [31] The skyrmion lattice in FeGe is shown in Figure 9.

Figure 8 (a) “A” phase transition in magnetic moments measurements vs temperature and external field [28] (b) (c)Various magnetic susceptibility vs temperature measured under different fields (d) AC susceptibility versus field [30].

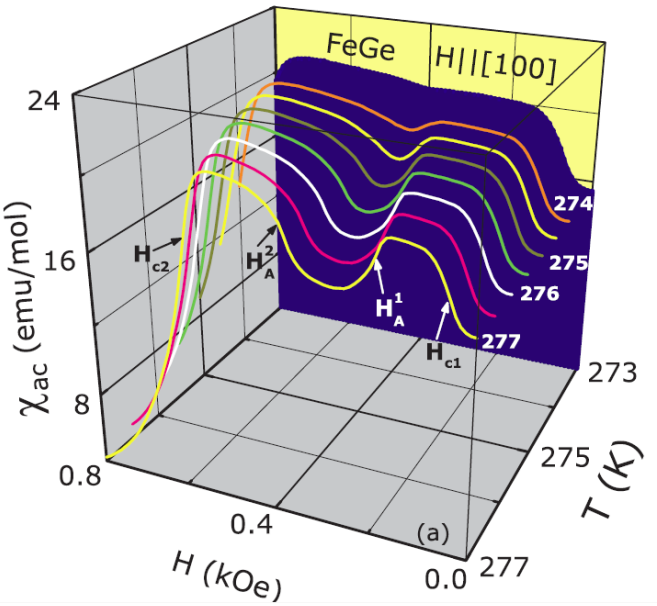


(a)



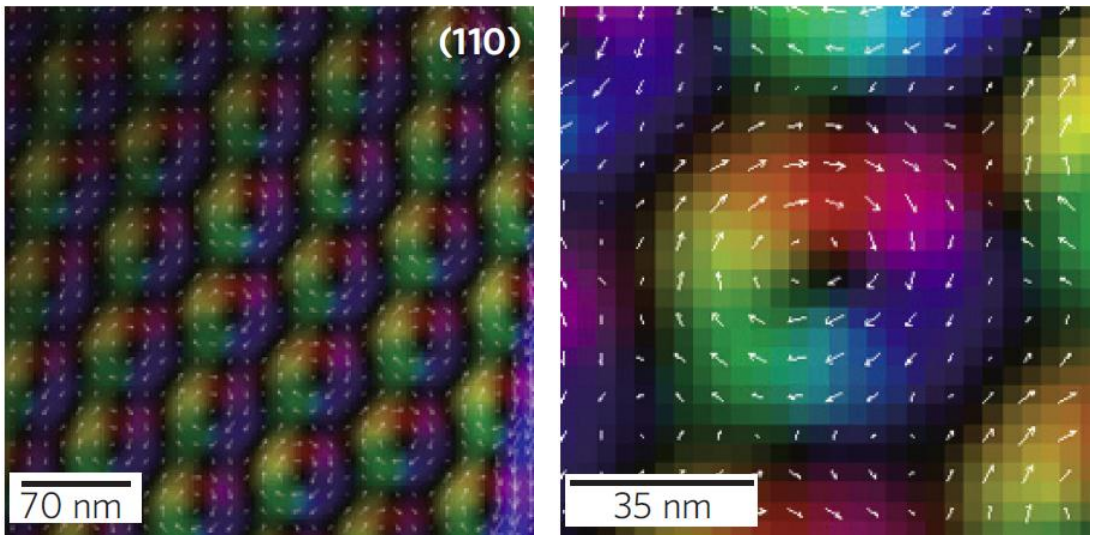
(b) (c)

Figure 8 continued



(d)

Figure 8 continued



(a) (b)

Figure 9 (a) Skyrmion lattice on thin plate of FeGe under Lorentz TEM (b) Size of a single skyrmion [31].

2.2.3 Skyrmion and domain wall motion

A skyrmion and a magnetic domain wall motion share many similarities. Their motion could be driven by the magnetic field or the electrical current. [32–34] In the field-driven domain motion, the domain wall's velocity could be measured by the Giant magnetoresistance (GMR) effect. If a field is applied to the right and wires with magnetic moments orient to the left, the domain begins to grow with, the domain wall moving to the right. The total resistance changes if another layer of known magnetization is covered. The total resistance will act like the GMR effect. A threshold field named the Walker breakdown field is the maximum field that could be applied in a field-driven motion of domain walls because above it; the motion becomes turbulent and oscillates. Below this field, the velocity is almost linearly increased with field strength. [1]

Another way to move a domain wall is through an electrical current. Passing a spin-polarized current to the domain wall, a torque is applied by localized magnetization (Fig 10). And also the spin polarized curent exerts a torque on local magnetization (domain).The domain wall is moved by the spin transfer torque ,and domain wall motion can be seen in several ways, including magnetic soft X-ray microscopy, spin

polarized scanning electron microscopy and Magnetic force microscope (MFM). [35–37] By injecting a pulsed current for appoximately several nanosecond, the distance the domain wall travels can be measured, and domain wall's velocity can be calculated.

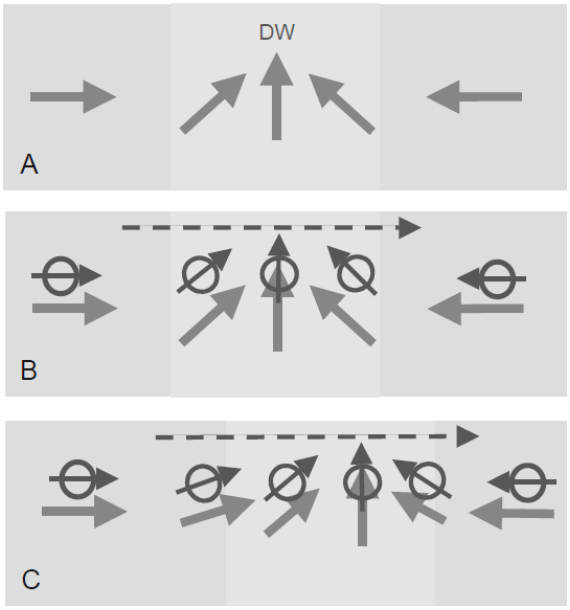


Figure 10 Current-driven domain wall motion [3].

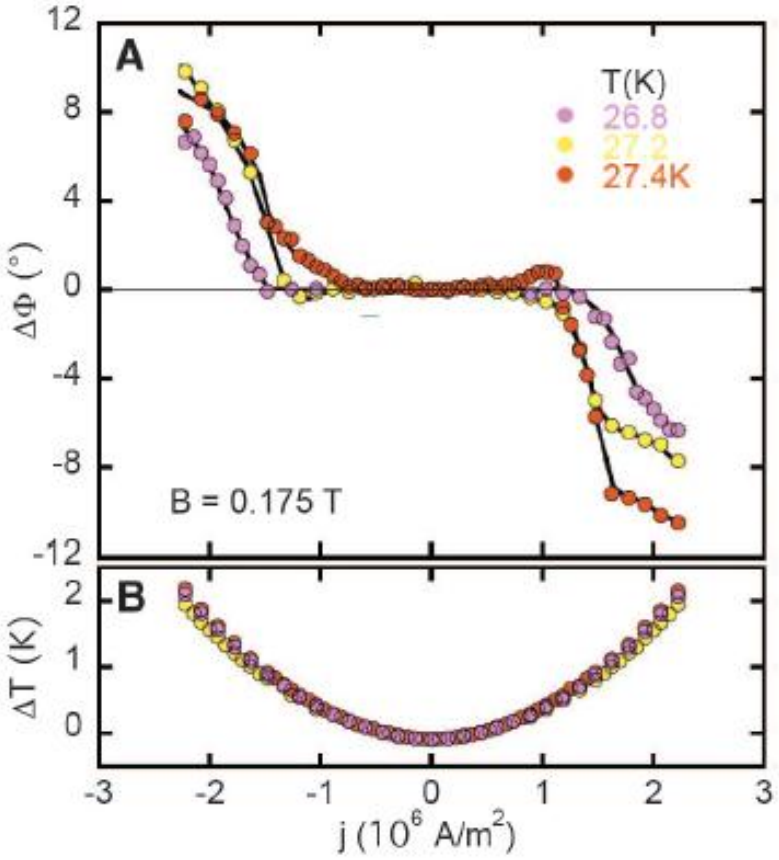


Figure 11 Spin transfer torque at ultra-low current density of MnSi single crystal [34].

In traditional ferromagnetic materials, a current density of $10^{11}Am^{-2}$ was required to move domain walls. However, a current density of only $10^{6}Am^{-2}$ was needed to rotate a skyrmion with spin-polarized current. [32] [38] The rotation was observed through neutron data. The rotation angles versus current density and threshold current density at different temperatures are shown in Figure 11. This low current density suggests exploring the spin transfer torque in nanowires because much heating is avoided when a small current passes through. [32,34] A skyrmion could be written and deleted by the tunneling current [39]. Researchers have proposed aligning domain wall along a nanowire track, and using a reading head measure its magnetoresistance or a writing head to inject current. This method shows great potential for next generation of data storage device. [40] Because it is cheaper, more energy efficient, and faster. Replacing the domain wall with skyrmion, much less energy would be consumed.

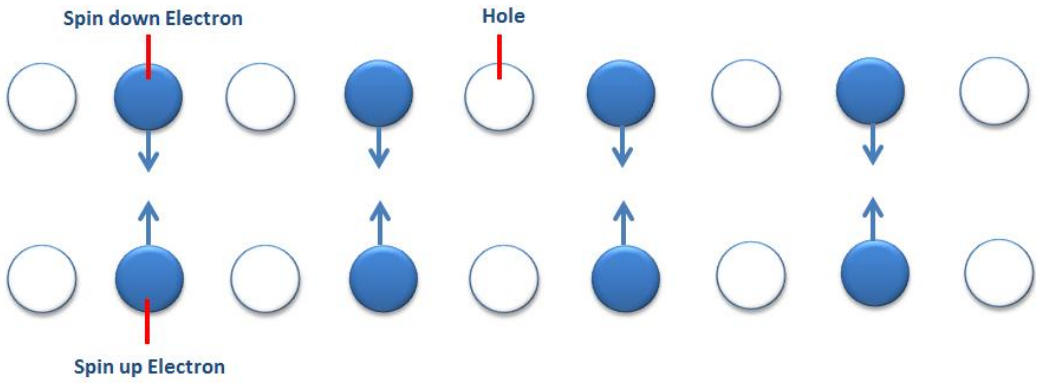
2.3 Spin density wave

2.3.1 Formation of spin density wave

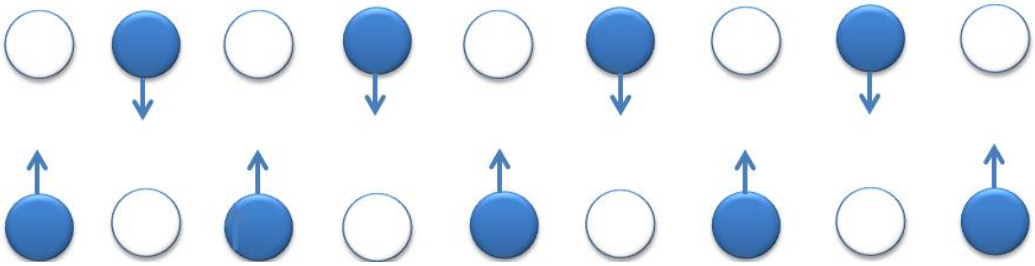
Spin density wave (SDW) is a low-temperature ordered state such as ferromagnetism, antiferromagnetism and superconductivity. [41–43] SDW is formed by electron-electron pairs which should repel to each other.

In Fig 12, the normal state, charge density wave state and spin density wave state are plotted. In normal metal, the number of spin-up electrons equals the number of spin-down electrons. Therefore, the total spin density is zero, and the total charge is constant. In charge density wave (Fig 12 (a)), electrons with opposite spin direction are paired up with charge density's wave distribution. However, in spin density wave (Fig 12 (b)), the spin of electrons has been separated, which makes spin density's wave distribution. Because the spin density's wavelength is determined by electrons, incommensurate SDW is named for SDW's wavelength mismatching with ion spacing-lattice constant. If the SDW's wavelength is fit to the lattice constant, it is commensurate SDW. [43] In $FeGe_2$, as the temperature is lowered, a magnetic curve passes through

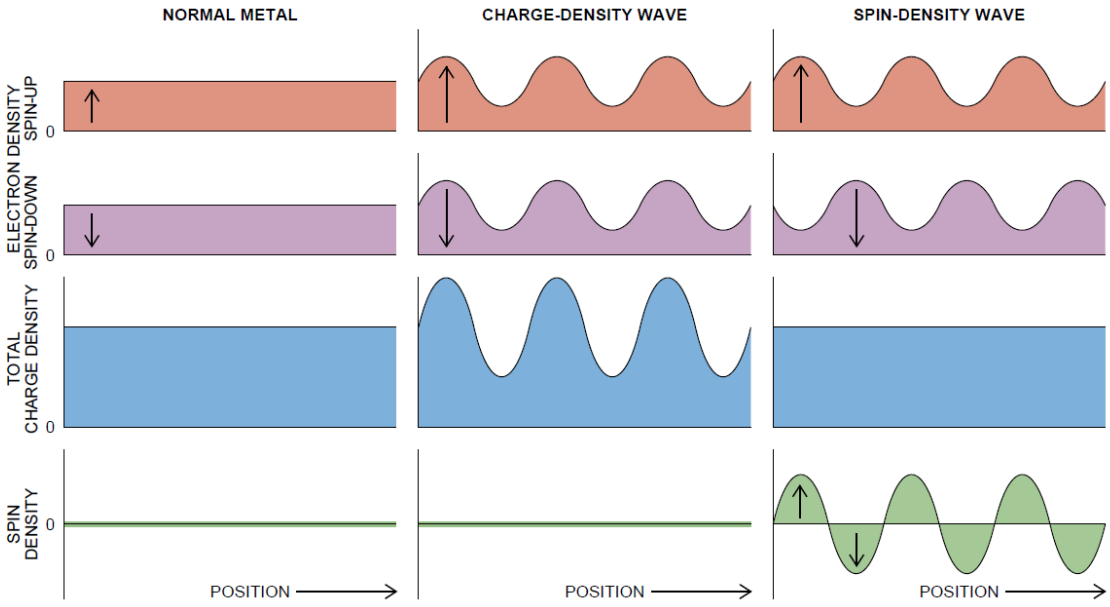
paramagnetism to incommensurate SDW at 289K, and then reaches commensurate SDW at 263K. [44–46]



(a)



(b)



(c)

Figure 12(a) Charge density wave (b) Spin density wave (c) Comparison of normal metal, CDW and SDW [41].

2.3.2 Verification of spin density wave

To identify the emergence of spin density waves, several methods were employed: conductivity measurement [44], neutron scattering [45–49] and nuclear magnetic resonance. Conductance is obviously easier to measure in nanowires.

As illustrated in Fig 13, when the temperature is lowered, the conductance will increase. That response could be explained by decreasing metal resistivity with temperature. However, after cooling, the materials will reach the SDW state. Then the electrons will have been paired and refuse to move freely. Then the conductance drops abruptly leading to insulator behavior. [41] This sudden transition is a clear sign of SDW.

$FeGe_2$ is a very special material having two types of SDW: incommensurate SDW and commensurate SDW. The transition from paramagnetic to incommensurate SDW is at 289K, and the transition from incommensurate to commensurate SDW is at 263K [45–47,51].In this case, magnetoresistance is considered the best way to identify the SDW phase's boundary because there is a slight shift when it reaches the boundary. (Fig 14)

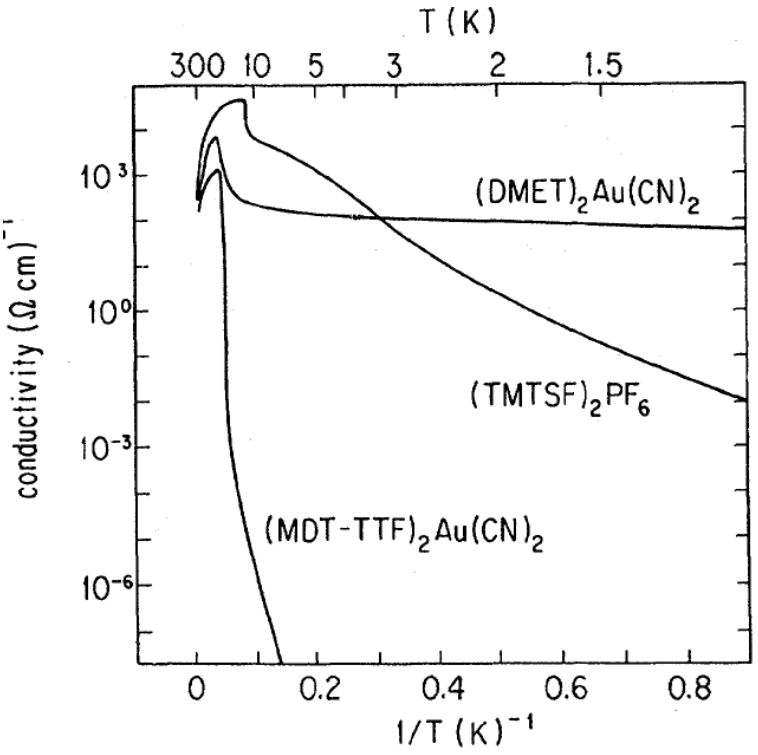
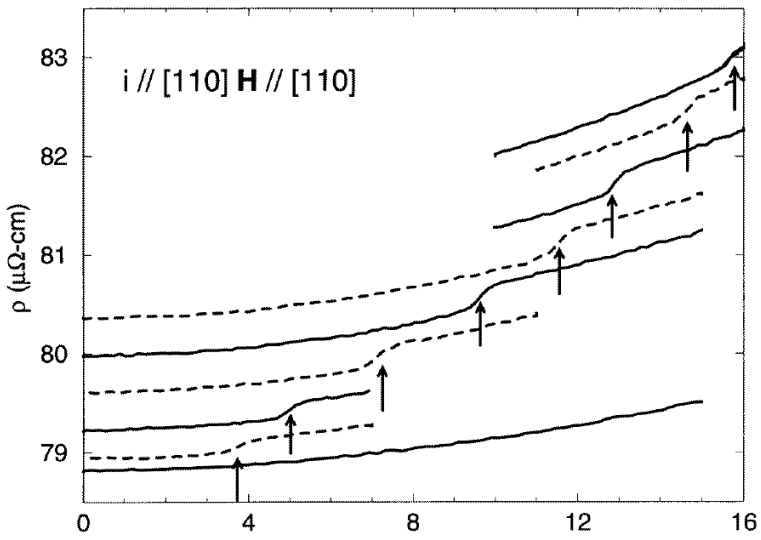
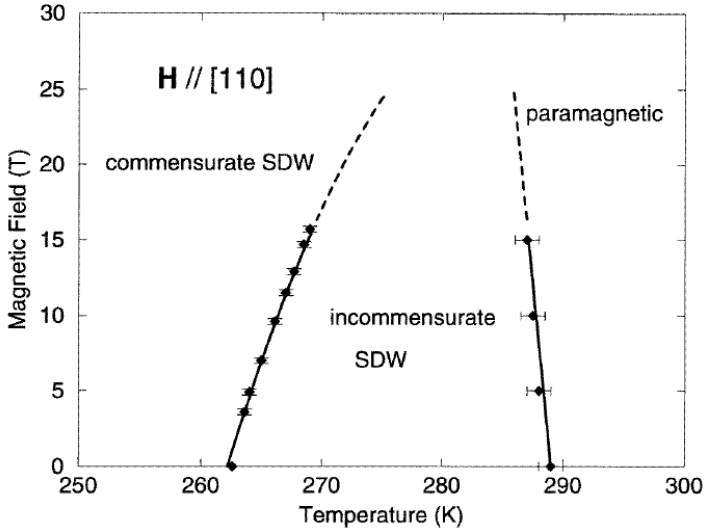


Figure 13 Conductance measurement of SDW [47].



(a)



(b)

Figure 14 (a) Resistivity changes when applying current and field along [110], from bottom up each curve represents a temperature: 260, 263.6, 264, 265,266.1,267,268.5,269K (b) Constructed magnetic phase diagram [51].

CHAPTER 3 DESIGN OF THE CVD SYSTEM FOR NANOWIRE GROWTH

3.1 Nanostructure prepared in chemical vapor deposition with leaks

Nanowires of MnSi compounds could be prepared through directly evaporating Mn powder on a silicon substrate. Many experiments were initially attempted in the CVD system with leaks because the system were sealed by rubber tubes. At the same time, Ar gas was kept flowing to avoid too much air in the system. In that case, nanowires began to grow. However, Mn_4Si_7 crystals were formed on the substrate in a well-sealed system.

In those samples with nanowires, usually four different morphologies were observed: the continuous film, the nanowires, the nanowires plus scattered particle, the particles. Strangely, the wires are located in a narrow area near the edge as shown in Fig 15. EDX were applied to measure the relative composition of Mn deposit on different regions. The same size squares are used to get the spectrum in different bands.

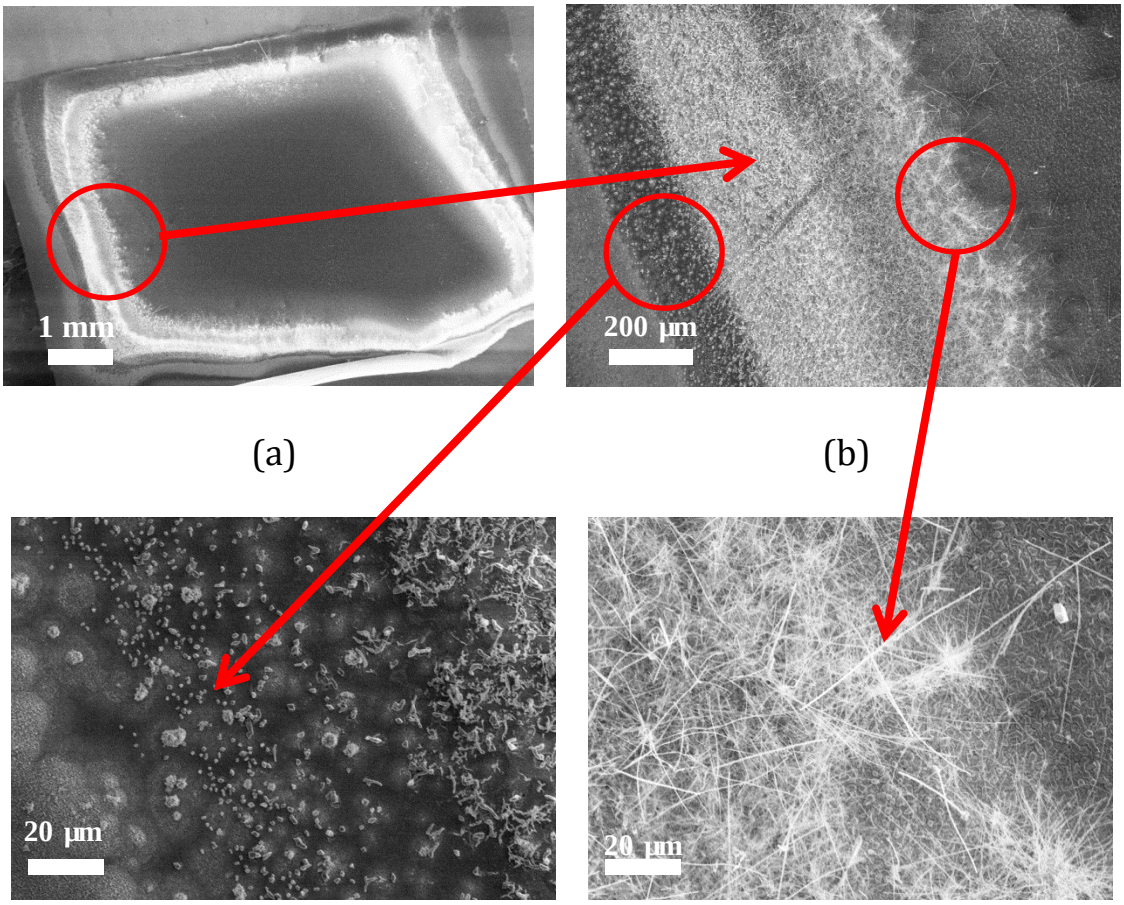


Figure 15 Different morphologies observed in CVD when leaks are in the system: (a) Three narrow bands (b) Details in narrow bands (c) Details of outermost band with scattered particles (d) Innermost nanowires band.

Table 2 Composition of Mn:Si in samples prepared by atmosphere CVD

Name (from outside to inside)	**Mn % (atomic)**	**Si % (atomic)**	**Relative Mn:Si (Atomic composition)**
First band (scattered particles)	10.15	89.85	0.113:1
Second band (Nanowires plus scattered particles)	22.43	77.57	0.289:1
Third band (Nanowires)	32.2	67.8	0.475:1
Inner band (Continuous film)	30.71	69.29	0.443:1

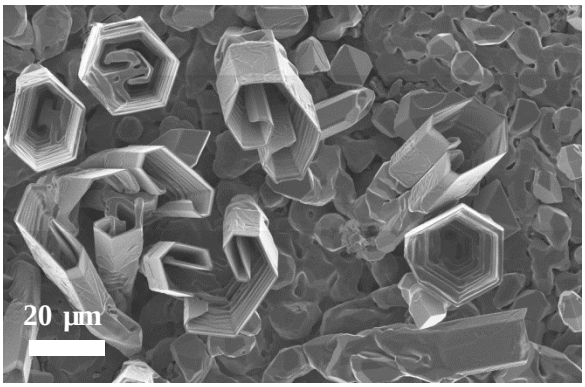
The data shows Mn composition increased from outside to inside. At the same time, samples were prepared for the Mn powder directly touching the silicon substrate's surface. Several Mn-Si multiple symmetric structures formed like "rolls" (Fig 16 (a)); their composition was around 50% Mn and 30% Si. Based on the experiment conducted in the pumped CVD system, it is concluded that "something" formed in the substrate edge that could promote the one-dimensional growth. Neither too much Mn nor too much silicon promotes nanowire growth.

The nanowires were prepared with different gas flow directions, but no differences resulted.

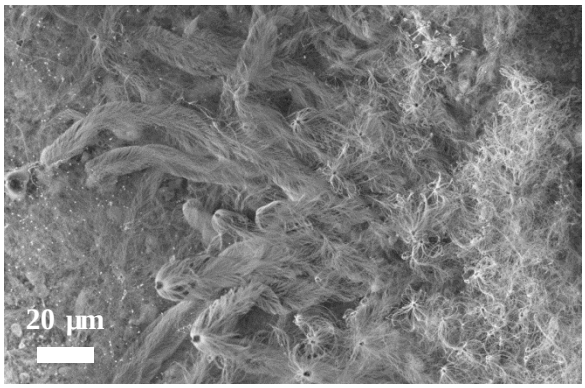
Excluding the flow direction effect, another reason may be the role of oxygen. If oxygen reacts with the silicon substrate in the system, it should be near the edge since other places have a high percentage of Mn vapor. To verify this mechanism, experiments were conducted with the system open to air. The result is shown in Fig 16 (b)(c).

In this experiment, many octopus structures were formed with Mn head and SiO_2 tentacles, indicating, wire structures prefer oxygen-rich surroundings. However, with too much oxygen in the system, nanostructures became too oxidized. Therefore, the amount oxygen should be less and controlled. In this case, proper oxides may be

another option to promote nanowire's growth. To identify, a thin glass slide (SiO_2) 100μm thick was used as a substrate in a sealed system. In this case, the SiO_2 melted immediately after being deposited onto the Mn vapor. However, in the region near the melted SiO_2, the nanowires appeared and located around the melted area (Fig 17). Because Mn-Si nanowires very likely growing on the SiO_2 , synthesizing them using substrates with SiO_2 thin film with a well-sealed system was attempted.



(a)



(b)



(c)

Figure 16 (a)"Hexagonal roll" structure; (b) Morphology of nanowires prepared in system open to air (c) Details of Mn head with SiO_2 hairs.

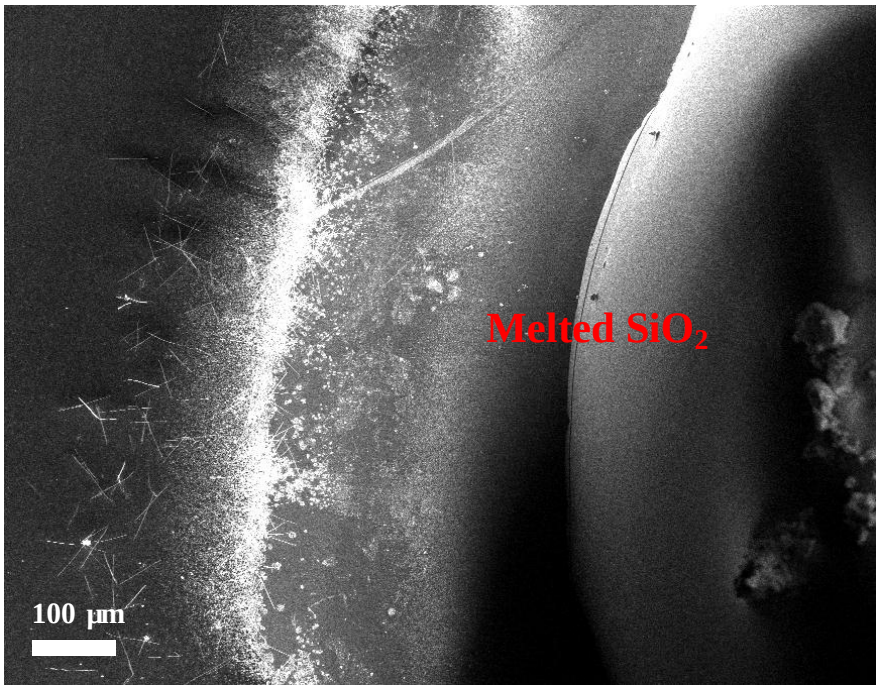
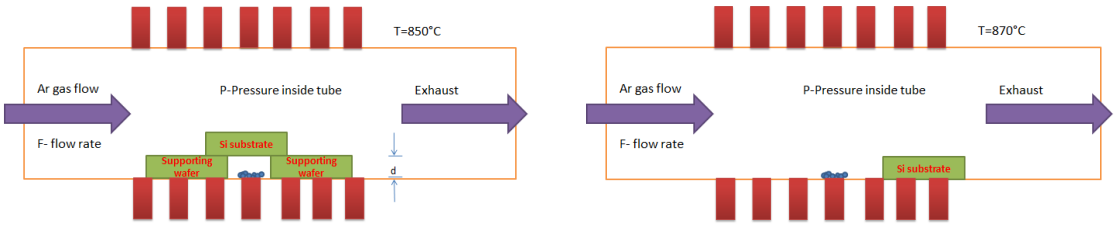


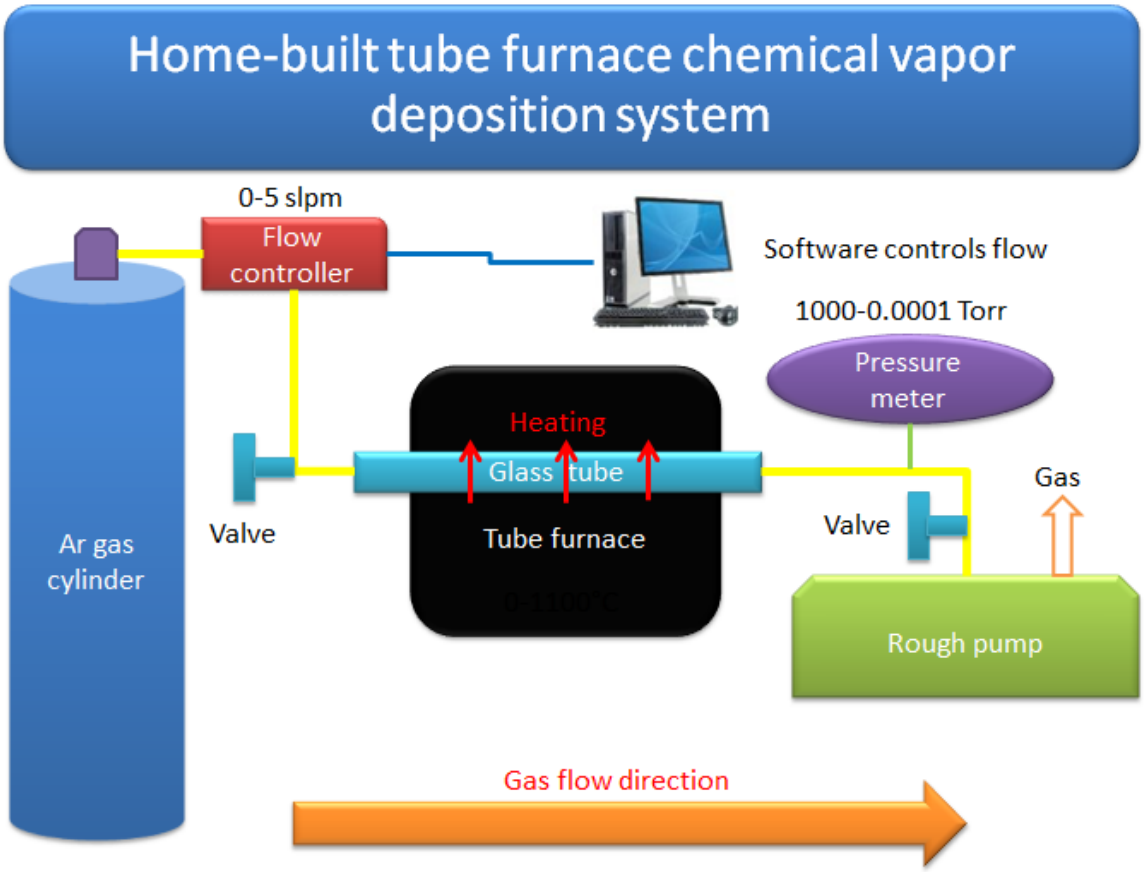
Figure 17 Nanowires growing around the melted SiO_2.

3.2 CVD System setup

In this study, a homemade tube furnace chemical vapor deposition system was used. This system has a flow controller, pressure gauge, mechanical pump with a needle valve to control pumping speed, and a tube furnace for temperature control. Substrates were Si wafers with a thermal growth of SiO_2 layer hundreds of nm thick. Two geometries of source and substrate locations are shown in Fig 18 (a)(b). Choosing them depended on the source material's evaporate rate. The system's design is shown in Fig 18 (c).



(a) (b)



(c)

Figure 18 (a)(b)Two geometries of chemical vapor deposition in nanowires' growth, (c) the CVD system's design.

3.2.1 Tube furnace heating curve

Temperature is a critical parameter for controlling growth. Usually the precursor of evaporating temperature is different from that for substrate deposition. Halides are preferred in nanowire synthesis because of their low melting and boiling points; however, metal powders require more heat to evaporate. In the substrate's location, the temperature should be kept in the range where the expected phase is stable. Thus, the temperature curve of this study's tube furnace was essential to growing the right phase of the nanowire. Pressure, flow rate, geometry, and substrates together could suppress the supersaturation ratio, which enables one-dimensional growth.

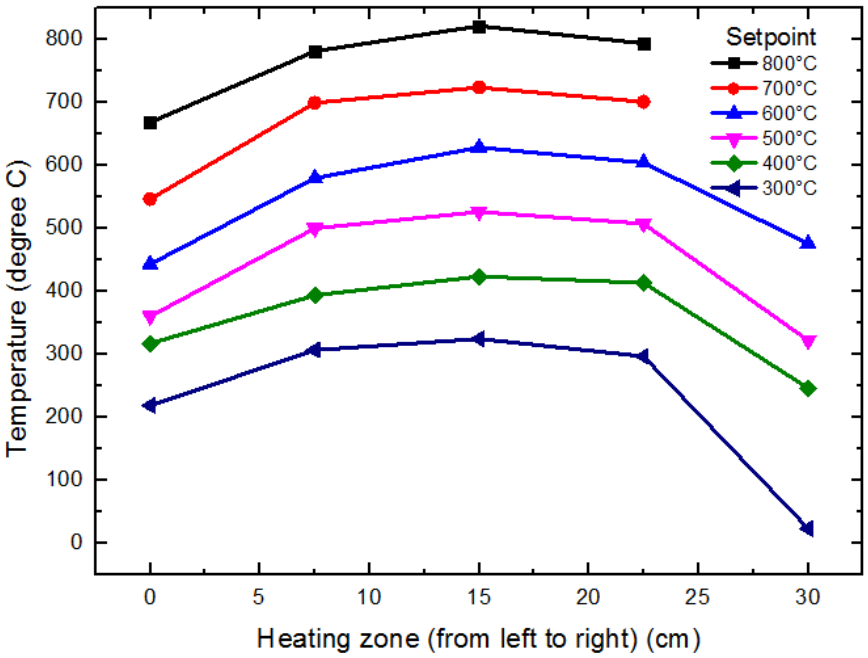


Figure 19 Temperature profile vs. position in tube furnace used for CVD.

Fig 19 shows, the tube furnace's temperature profile is shown. Each color represents a set temperature, displayed in the tube furnace's control panel. The actual temperature was measured by thermocouple each time moving its tip 5 cm in one direction. Clearly, the real temperature was not consistent with the set temperature. In the middle of the furnace, the actual temperature was 20°C higher than the displayed temperature; however, the temperature on both sides, 7.5 cm from the middle, was very close to the set temperature. At the end of the heating zone, temperature drops greatly at 100-200°C. In the experiment process, the Argon gas flowed into the whole tube and carried away heat. Therefore, the real temperature gradient should be larger in the side connecting to the gas cylinder. There is situation when there is a temperature competition between the precursor and product. Two-zone or even three-zone furnaces have often been used to control the temperature of both the source material and the substrate. By placing the sample and the substrate in different locations inside the glass tube, temperature could be controlled in the same way.

3.2.2 Pressure gauge calibration

The convection vacuum gauge (KJLC 275i) was purchased from Kurt J. Lesker Company. The measurable pressure range is 1 mTorr to 1000 Torr; Its factory setting is calibrated with N_2 and air. The carrier gas employed here was Argon (Ar); thereofre, further calibration was required. Based on the table in this pressure gauge's manual, a curve was plotted and a function fitted with this curve. Any real Ar pressure P_{real} could be calculated from $P_{display}$ (Fig 20). When only argon is flowing through the system,the pressure is 760 Torr while the gauge shows 23.8 Torr .

$$P_{real} = 104.88 \times \left|P_{display} - 8.83\right|^{0.68} + 100$$

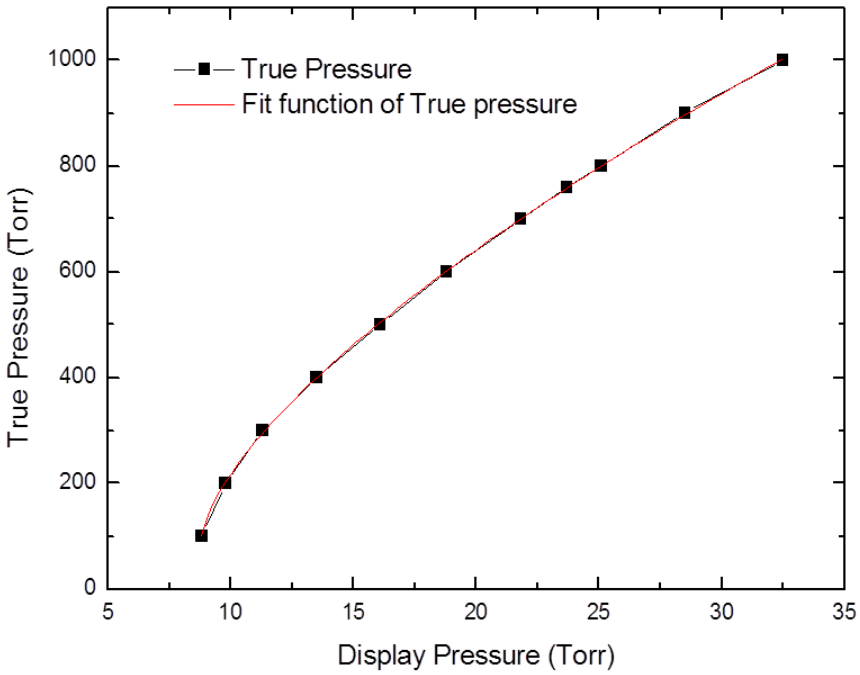


Figure 20 Relationship between displayed Ar pressure and real Ar pressure.

3.2.3 Flow meter calibration

The flow meter was purchased from Sierra Instrument Company. With a cable connected to a computer, the required flow rate was easily adjusted using the installed software. For Ar gas, however, the true flow (F_{true}) rate is shown below:

$$F_{true} = 1.398 \times F_{display}$$

3.2.4 Oxide layer growth on silicon wafer

The oxide layer was synthesized using an atmosphere pressure Chemical Vapor Deposition system at the Center for Nanophase Materials Science, Oak Ridge National Laboratory. The dry method used silicon thermal reacting with slowly oxygen, creating a thin dense film. However, an oxide thickness of more than 200 nm often involved the wet method, in which water reacted with silicon, creating a relatively faster growing speed.

3.3 Characterization Tools

3.3.1 Morphology, structure and composition

Most characterizations were conducted at the Center for Nanophase Materials Science, Oak Ridge National Lab. The Zeiss Merlin VP Scanning

Electron Microscope(SEM) equipped with Energy-dispersive X-ray spectroscopy(EDS) was used to identify the growing structures and compositions, which guided adjustments to the growth parameters. X-ray powder diffraction with a temperature-controlled sample environment was used to identify the main phases on the substrate. The Soft Matter Transmission Electron Microscope(TEM) ,(Zeiss Libra 120 TEM), and FEI Titan S aberration-corrected TEM-STEM were exploited to determine a single nanowire's diffraction pattern and high-resolution image, providing a structure and detailed morphology (Fig 21) .



(a)



(b)



(c)

Figure 21 (a) Powder X-ray diffraction (b) Zeiss Merlin VP SEM equipped with EDS (c) Zeiss Libra 120 TEM.

3.3.2 Magnetic and electronic properties

Superconducting quantum interference device(SQUID) magnetometers in CNMS was utilized to measure the sample's magnetic properties; SQUID's capability is for a unique class of sensitive magnetic measurements in key areas, such as high-temperature superconductivity, biochemistry, and magnetic recording media.(Fig 22(a)) Capable of homogeneity magnet configurations as high as ± 7.0 Tesla; The equipment's functions include the followings:

1. Continuous low-temperature control/temperature sweep with enhanced thermometry and reciprocating sample option (RSO) - DC magnetization absolute sensitivity: 1 x 10^{-8} emu at 2,500 Oe;
2. SQUID AC Susceptibility Measurement, 0.1 Hz to 1 KHz;
3. Horizontal and Vertical Sample Rotators
4. Fiber Optic Sample Holder
5. Magnet Reset

In this study, the equipment was mainly used to measure magnetic transition curves, M-H hysteresis curves, and ac susceptibility. All of the samples have been analyzed to verify the existence of helimagnetic structure, skyrmion and various magnetic properties. Physical property

measurement system(PPMS) was used mainly for the single nanowire device's resistivity and its magnetoresistance (Fig 22(b))



(a) (b)

Figure 22 (a) SQUID used for magnetic measurements (b) PPMS used for transport properties measurements.

3.3.3 Device fabrication

A spin coater was used to cover the wafer with PMMA or copolymer (e-beam resist), the thickness of which was determined by spin speed. After coating, a baking system was used to bake the layer at 100-200°C (Fig 23(a)).

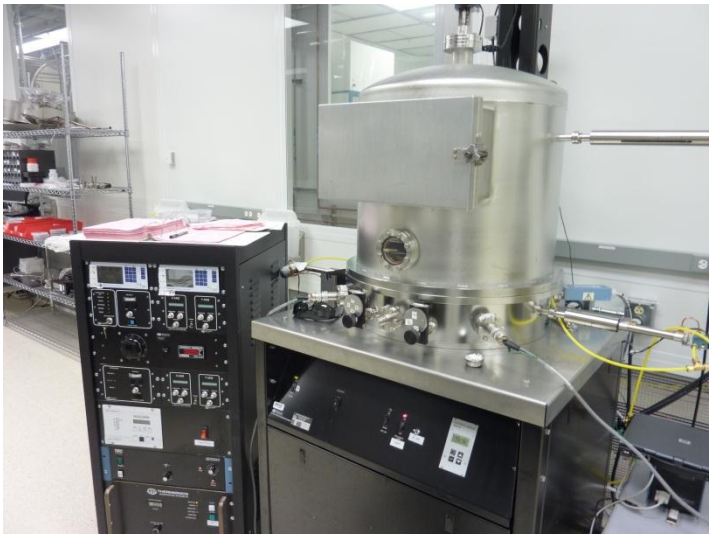
To write the pattern on the surface, the JEOL 9300FS 100kV Electron Beam Lithography System was used. This system writes at rates up to 50 MHz and has a minimum spot size approaching 4nm. Field sizes up to 1mm can be written without stage movement. The layout BEAMER was used for file conversion and proximity correction. High speed, large area writes with limited beam drift and variations across a wafer are a feature of this tool. Operation at high energy (100kV) allows writing on insulated substrates with minimal or no dissipation layer (Figure 24). Chemical solutions of PMMA, Copolymers, MIBK+IPA (the volume percentage of MIBK determing the developing aggressiveness and feature size); isopropanol (used to stop develop); acetone, and a liftoff strip are used to cover the wafer, develop the pattern and liftoff the gold layer.

A dual-beam evaporator was used to deposit the metal film electrodes such as Cr/Au/Ti/W. Electrons were controlled by a magnetic field to

hit the target which evaporating the metal on the substrates. The deposit speed was fast but usually controlled at 1Å/sec. Electron beam deposition has smaller grain size and is more uniform than sputtering(Fig 23(b)).



(a)



(b)

Figure 23 (a) Multiple-speed spin coater (b) Dual electron beam metal evaporator.



Figure 24 JEOL 9300FS 100kV electron beam lithography system.

CHAPTER 4 OPTIMIZATION OF THE E-BEAM NANOFABRICATION PROCESS FOR NANODEVICES

Four-probe devices are widely used to measure nanowire's physical natures such as electrical or magnetic properties. The process involves several steps including transfer, measure, design, coating, exposure, develop, deposit and liftoff. Each step involves more precautions because nanowire is easy to break comparing to bulk materials.

4.1 Standard procedure for device fabrication via e-beam lithography

4.1.1 Preparation of transferring wafer

A clean silicon wafer was used to grow a thin layer of silicon dioxide (around 200nm). The reason for this step was that the silicon dioxide could be used as an insulating intermediate layer between the nanowires above and the silicon wafers below. Gold cross markers were designed and deposited beforehand. The process was the same designing the electrodes, exposing them under an e-beam, and depositing them. In this study, 25 patterns were in one whole piece of

wafer, and each pattern contained 31*31 cross markers. Each marker was 60 μm in width and 200 μm from each other.

4.1.2 Transferring and measuring nanowires, and designing electrodes

Nanowires were scratched from a growth wafer using a clean blade, and then some acetone/ethanol was sprayed on the wafer. A droplet containing several nanowires fell onto each pattern. The wires were easily seen under the scanning electron microscope. The straight wire was found, and, the distance from its middle point to its surrounding four nearest crosses was measured. Then the nanowire's length and diameter were measured. Finally,the column and row was counted in which the nanowire was located so that e-beam could easily find it later (Fig 25).

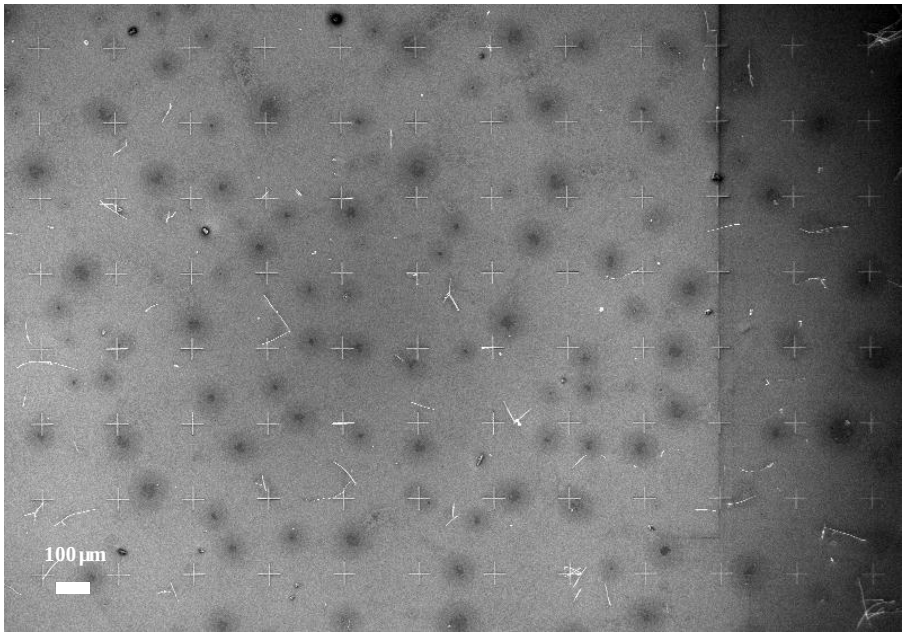


Figure 25 Nanowires transferred in each 31*31 pattern.

Based on the measuring coordinates (Fig 26(a)), four probe devices were designed using software named “Layout”(Fig 26(b)). Designing the electrodes was very complicated because they could not be too small or too big. Square electrodes as big as 500 μm took around 32 hours to run over the 25 patterns using the e-beam system. However, if too small, electrodes were very difficult to attach to outer electric wires for measurements. Designing the spacing between contacts also required caution. Current contacts should be farther from each other and the same with voltage contacts. However, current contacts should be closer to voltage contacts to avoid a large error. However, narrower spacing might cause lift off issue.

4.1.3 E-beam writing

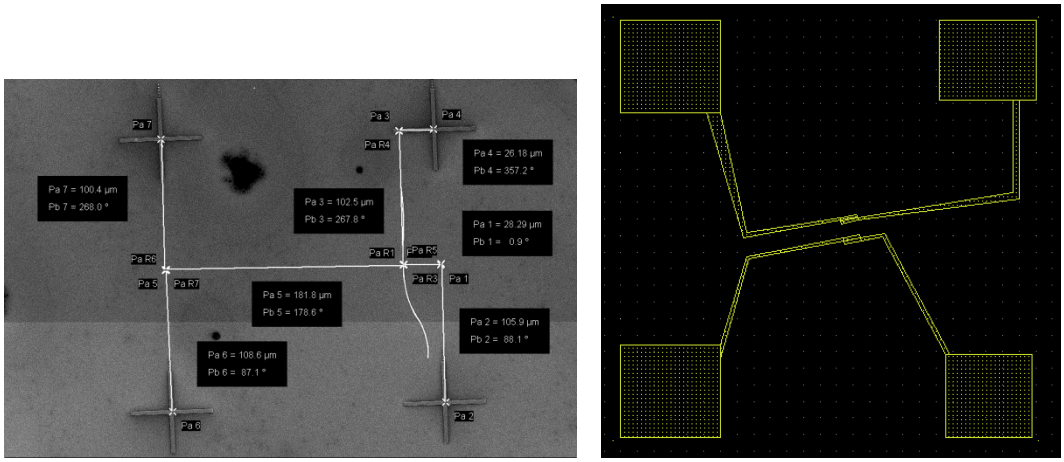
Before exposure, all the designed files should be changed to the e-beam system (JEOL 9300FS 100kV Electron Beam Lithography System) to read the files. Then, a layer approximately 200-300nm of e-beam resist (PMMA) was spin coated onto the transferring wafer before baking it for 1 minutes at 180°C. The thickness depended on the spinning speed. PMMA is a positive e-beam resist, which becomes soft and soluble in the developer after exposure. After loading the wafer, creating the job,

calibrating, and finding the location of nanowires by measured column and rows, the system began writing the electrodes. Later, the piece of wafer was removed and then put into MIBK+IPA (1:3) for development in 35s by cutting the chains of organic materials. Then the shape of devices was visible under optical microscope. Fig 26 (c) shows the designed pattern and the actuall pattern before liftoff.

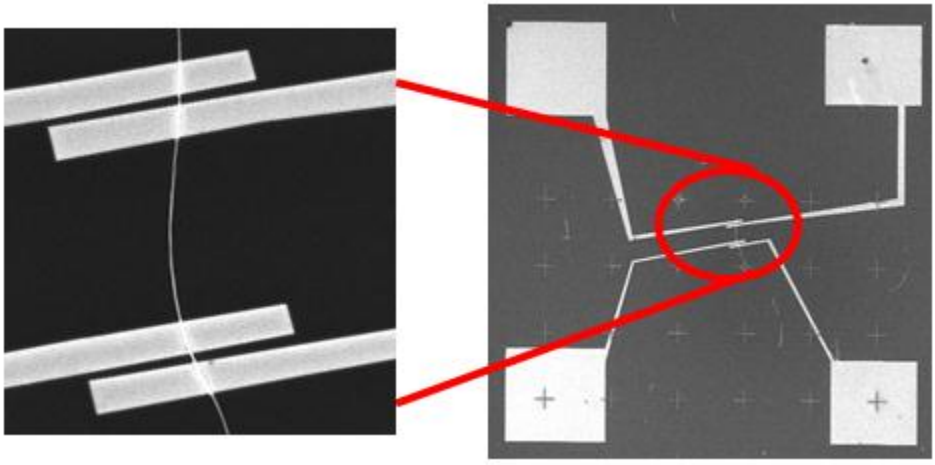
4.1.4 Deposit electrodes and lift off

Materials like Au and Cr were used for electrode. A dual-beam evaporator quickly deposited fast (usually controlled at 1Å/sec) the metal layer onto the pattern. Au is soft and does not stick to the wafer; therefore, 10 nm Cr was often first deposited before depositing 150-250 nm of gold film.

In the end, acetone was used for the liftoff process. The gold layer deposited on PMMA was cast off, leaving the electrodes. The entire process is shown in Fig 27.



(a) (b)



(c)

Figure 26 (a) Distance from the center of the nanowire to gold marks measured (b) Designed electrodes using Layout software (c) Real PMMA pattern after e-beam exposure.

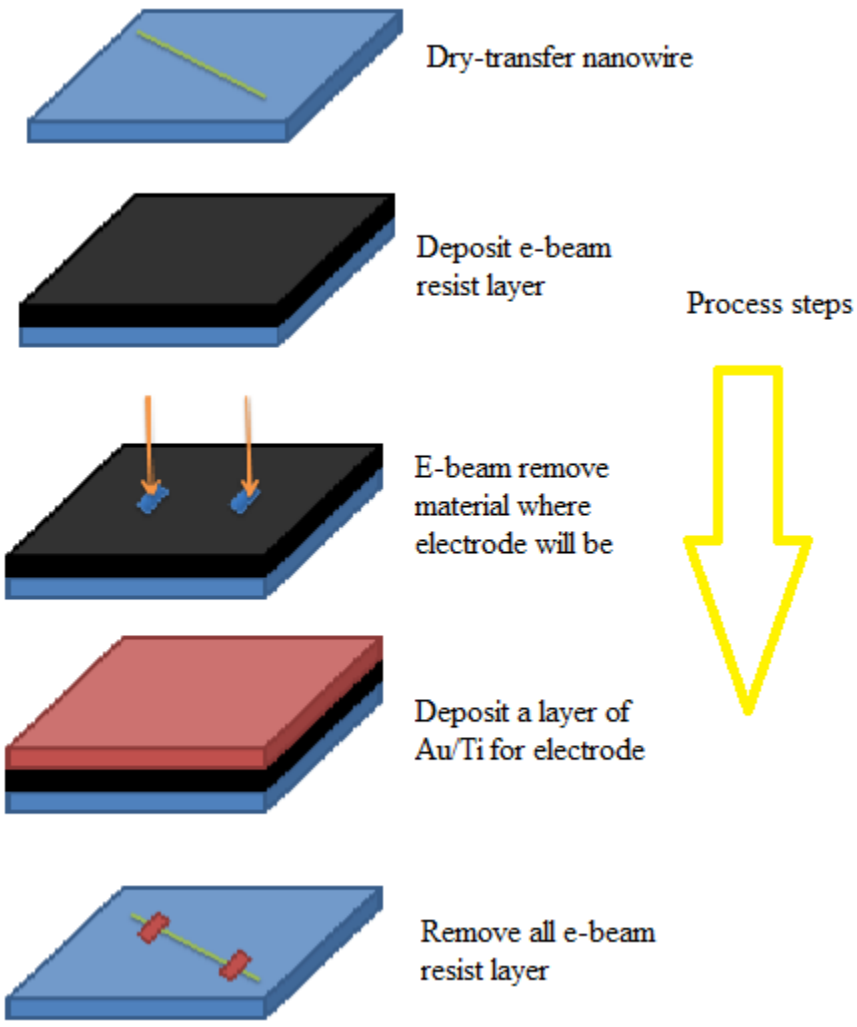


Figure 27 The Procedure of fabricating nanowire devices.

4.2 Problem in the process

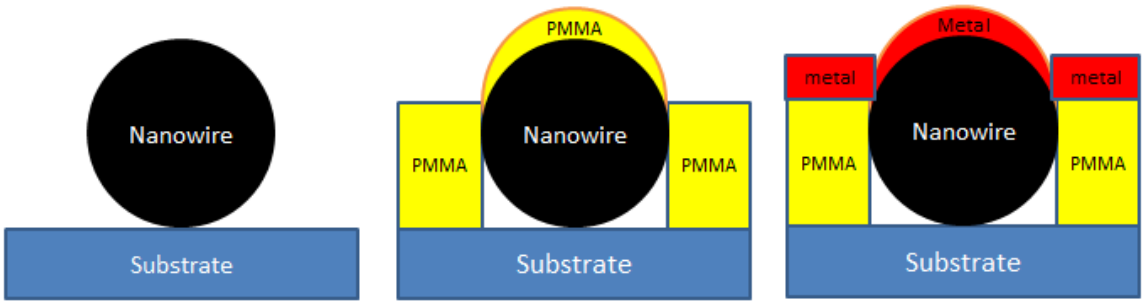
The wires were relatively thick (MnSi wires were 500-800 nm and $FeGe_2$ wires were 100-300 nm); therefore, fabricating the devices via a single layer of PMMA was very challenging. The problem was that the PMMA was so thin compared to nanowires, that after spin coating, the real thickness on the wires was smaller than in other places (Fig 28). Thus, after lithography, the remaining PMMA above the nanowires was gone. However, the PMMA thickness in other places was very thin compared to that of nanowires. Since the firmness of electrodes depends on their thicknesses, a thick metal layer was to make the deposited metal film attached each other result in hard liftoff because acetone could not penetrate the metal film. The SEM images in Fig 29 show this kind of problem.

4.3 E-beam energy dose correction and double layers of e-beam resist

The hard liftoff problem was caused by the thickness of PMMA and metal film. As a result, two methods were tried at the same time to avoid this situation. By adjusting the dose of electron beam, the best square of electrodes with the least PMMA residue could be found. And by adding

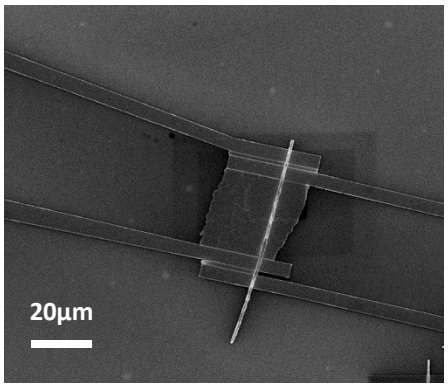
another layer onto PMMA, the attachment of deposited films was prevented. Dose means electric charge ($D=I_{beam}*T_{dwell}$) was exposed on the surface per unit area/length/dot. With only PMMA approximately 200 nm coated on the substrate, the PMMA residue decreased with an increasing dose.

In changing the dose, ordinary steps were followed. After e-beam lithography and development, the sample was put under an optical microscope to see if residue was inside the places which hads been exposed to the e-beam. Residue particle is usually observed, suggesting a higher dose.

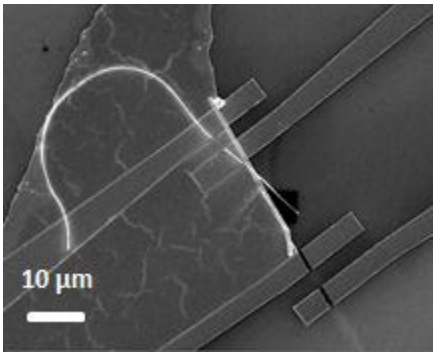


(a) (b) (c)

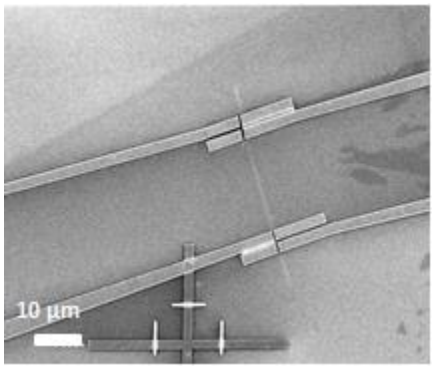
Figure 28 (a) Thick nanowire before spin coating (b) Thick nanowire after spin coating (c) Thick nanowire after depositing metal film.



(a)



(b)



(c)

Figure 29 Lift-off issue after the metal layer was deposited on the pattern.

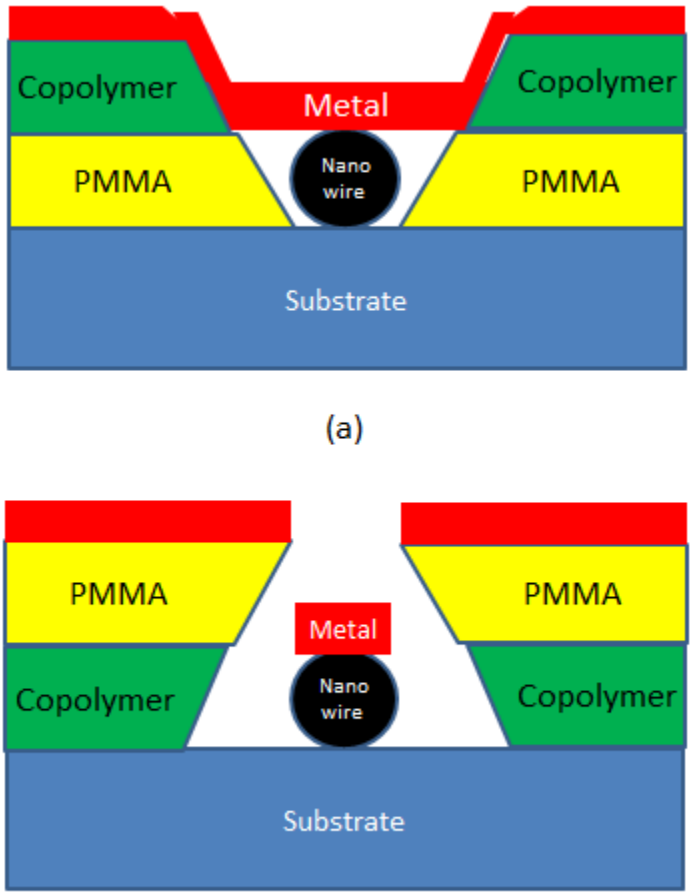


Figure 30 (a) Double layers with PMMA in bottom (b) Copolymer in bottom.

As shown in Fig 30, double layers were used to increase the resist's total thickness (lithography depth). Two geometries of these two layers were analyzed. The copolymer was much more sensitive to the e-beam and developed faster than the PMMA. However, the geometry played another role. The option shown in Fig 30 (a) will attach metal film because copolymer will form a wider feature than PMMA, leading to attachment and surface coverage, not allowing acetone to penetrate. As shown in Fig 30 (b), the PMMA developed more slowly, shadowing the gold layer to go inside. Saw-tooth shapes totally avoided the attachment of gold layers. $FeGe_2$ nanowires approximately 100-300 nm were spin coated with a double layer:first with copolymer and then with PMMA. The bake process was carefully controlled to avoid over baking. Copolymer was baked for 1 min at 150°C and PMMA was baked for 1 min at 180°C. Then MIBK+IPA was used for developing approximately 35s. The dose was optimized at 1050, 1150,1200,1250,1300. The dose of 1300 was used for the best lithography result. Electrodes of Cr-10nm (because gold is so soft) and Au-200 nm were applied after developing since thicknesses above 200nm was hard to liftoff. The final device is shown in Fig 31.

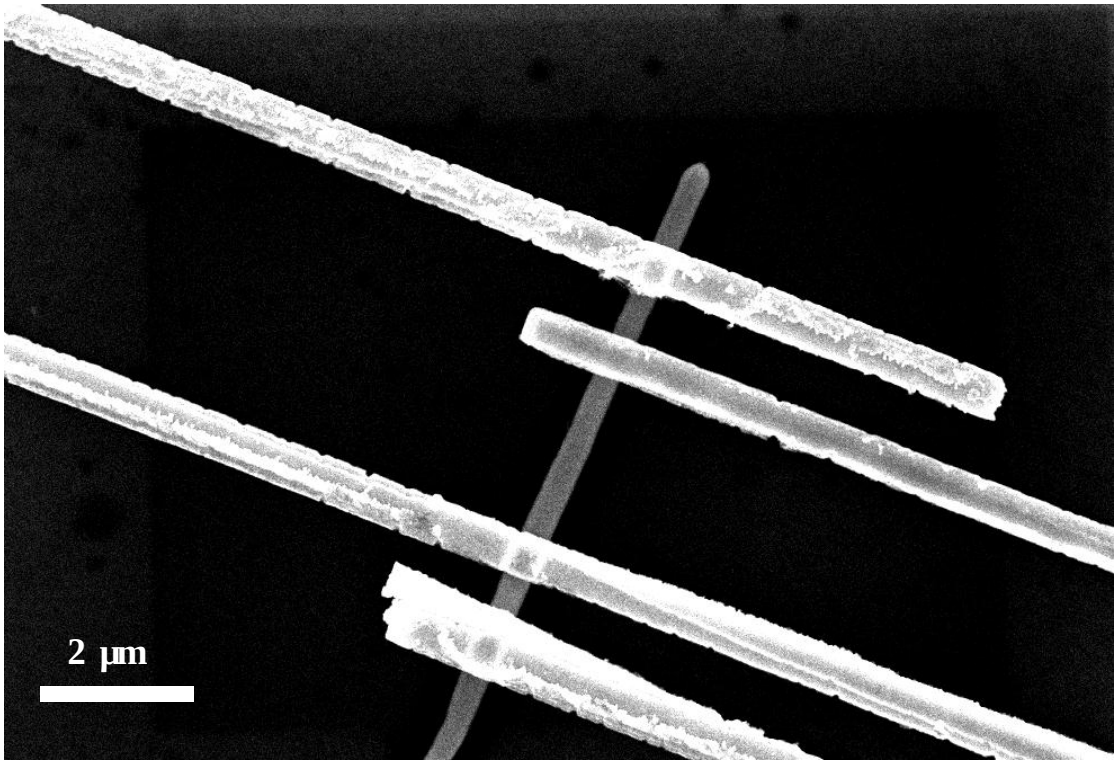


Figure 31 Four-probe nanowire integrated nanodevice used to measure transport properties.

CHAPTER 5 SYNTHESIS AND CHARACTERIZATION OF METAL SILICIDE NANOWIRES VIA OXIDE-ASSISTED GROWTH

5.1 Previous preparation of MnSi nanowires

MnSi nanowires were synthesized by $MnCl_2$ with Si wafer in two groups using CVD system [52,53]. In those two groups, one-zone and two-zone furnaces were used; therefore, different parameters were used. Although, both conditions were attempted in the system, countable nanowires remained in addition to a thick layer of Mn_4Si_7. Manganese powder was also used to prepare Mn_4Si_7 nanowires [54]. Fig 32 is the phase diagram of Mn-Si compounds. MnSi phase is between Mn_4Si_7 and Mn_5Si_3. Based on the reports above, the nanowires with high composition of Si were obtained with Mn vapor. The means of controlling the amount of Si to get MnSi nanowires were optional. Different from the MnSi wire growth and the conventional oxide-assisted growth method employed in growing of Si nanowires [5,55–57], in this study, the SiO_2 layer on Si substrate was used to assist and precisely control the growth process. The thickness of the SiO_2 layer

was found to play a key role in the high yield and the correct stoichiometric and crystalline growth of the B20 MnSi nanowires.

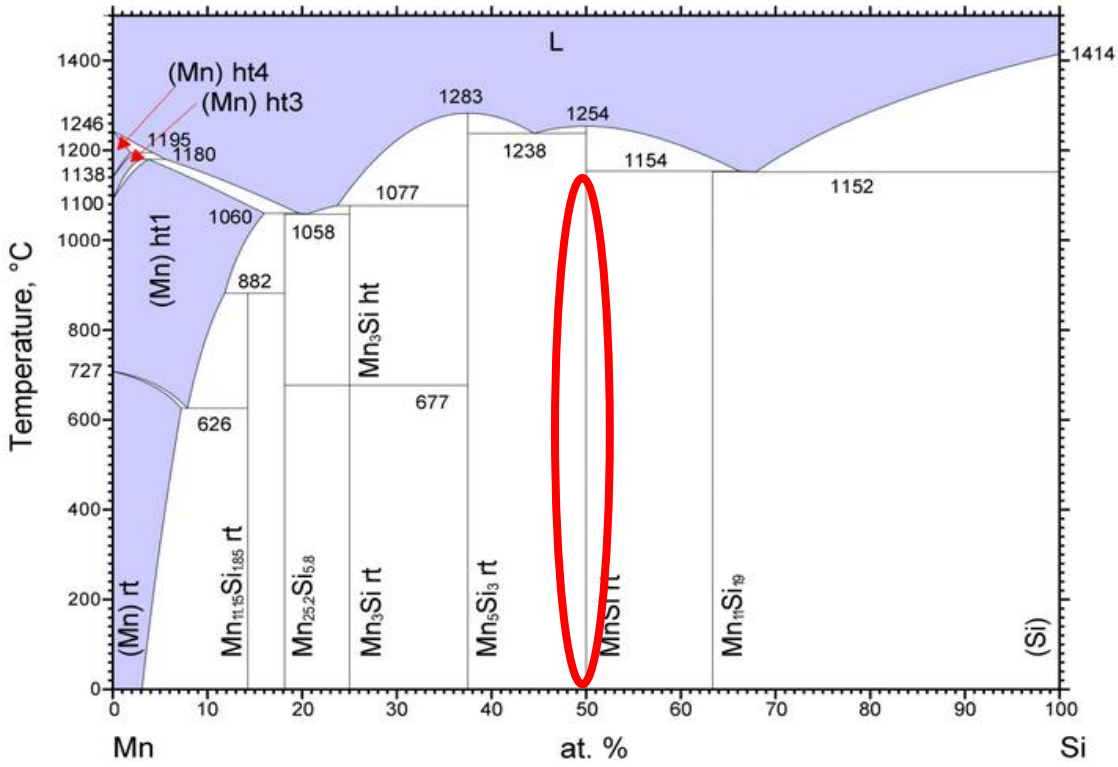


Figure 32 Mn-Si phase diagram [58].

5.2 Principle of oxide-layer assisted growth of silicide nanowires

Synthesizing of free-standing single crystal MnSi nanowires was explored via controlled oxide-assisted chemical vapor deposition. A characteristic signature of skyrmion magnetic ordering in MnSi nanowires was observed via magnetic measurements.

The growth of MnSi nanowires was first tried on a Si wafer with a natural oxidation layer (of few nanometers) and on hydrogen-terminated Si wafers. An oxidation-free Si(001) surface can be achieved after annealing the hydrogen-terminated Si wafer to 600°C. Following the optimized procedure from Refs [52,53], MnSi nanowires were only occasionally found around the ragged cutting edge of wafers or defected areas. The number of nanowires on an oxidation-free Si wafer is very small. Furthermore, while more wires were observed to grow on a wafer with a native oxide layer, the yield was still small. Controlling the thickness of SiO_2 does significantly increase the number of nanowires. The observed existence of an optimum SiO_2 layer thickness for the growth of MnSi nanowires with high yield and correct stoichiometry reveals of the SiO_2 layer's significant role in the growth, which can be understood as oxide-assisted growth. The elemental Si required for the

MnSi wires is unlikely to come from the SiO_2 layer's surface for two reasons: the growth behavior is strongly dependent on the thickness of SiO_2 layer, and the reaction temperature (850 °C) is much lower than the dissociation temperature for SiO_2 (1400 °C). The Si needed for the MnSi growth probably comes from the Si underneath the SiO_2 layer. At an elevated temperature, intermediate product of SiO can be formed by a chemical reaction of $SiO_2+Si \rightarrow 2SiO$ at the interface of Si wafer and the adjunct SiO_2 layer [59–61]. The two key roles that SiO plays during the growth are: first, after diffusing from the interface to the surface of wafer, SiO acts as a nucleation site which adsorbs surrounding Si and Mn atoms for the one-dimension wire growth. As observed previously in Si nanowires' growth using laser ablation, much higher nanowire yield could be achieved by introducing SiO_2 powder into the Si target to form SiO [62]. Secondly, SiO forms at the Si/SiO_2 interface, and then subsequently diffuses through the SiO_2 film. The reverse reaction occurs at the other interface, creating the Si interstitials; and the reaction is repeated at the interface. This diffusion process not only diffuses SiO from the interface to the surface, but also largely enhances Si atoms' self-diffusivity through the SiO_2 layer to the surface [60] to achieve correct Mn and Si stoichiometry. At the surface of SiO_2, chemical

reactions, such as $2SiO+2Mn \rightarrow 2MnSi+O_2$, $2SiO+Mn \rightarrow MnSi+SiO_2$ or $Si+Mn \rightarrow MnSi$ are needed to form the MnSi nanowires. It is worth emphasizing that this growth process involves an oxidation-reduction reaction, or an oxide-assisted synthesis method, to differentiate from other growth methods. [63]

5.3 Experiment details and characterization of MnSi nanowires

To quantitatively control the effect of oxygen on the growth of MnSi wires, the thickness of the SiO_2 layer on the Si substrates was varied. The temperature, gas flow, pressure, distance from sample to precursor and the SiO_2 layer were precisely controlled in a homebuilt system schematically shown in Fig 33(a). Growths were performed on Si wafers with the oxidation layer thicknesses varying from 0 nm up to 1000 nm. The number of wires on the substrate increased dramatically when the SiO_2 layer is introduced.

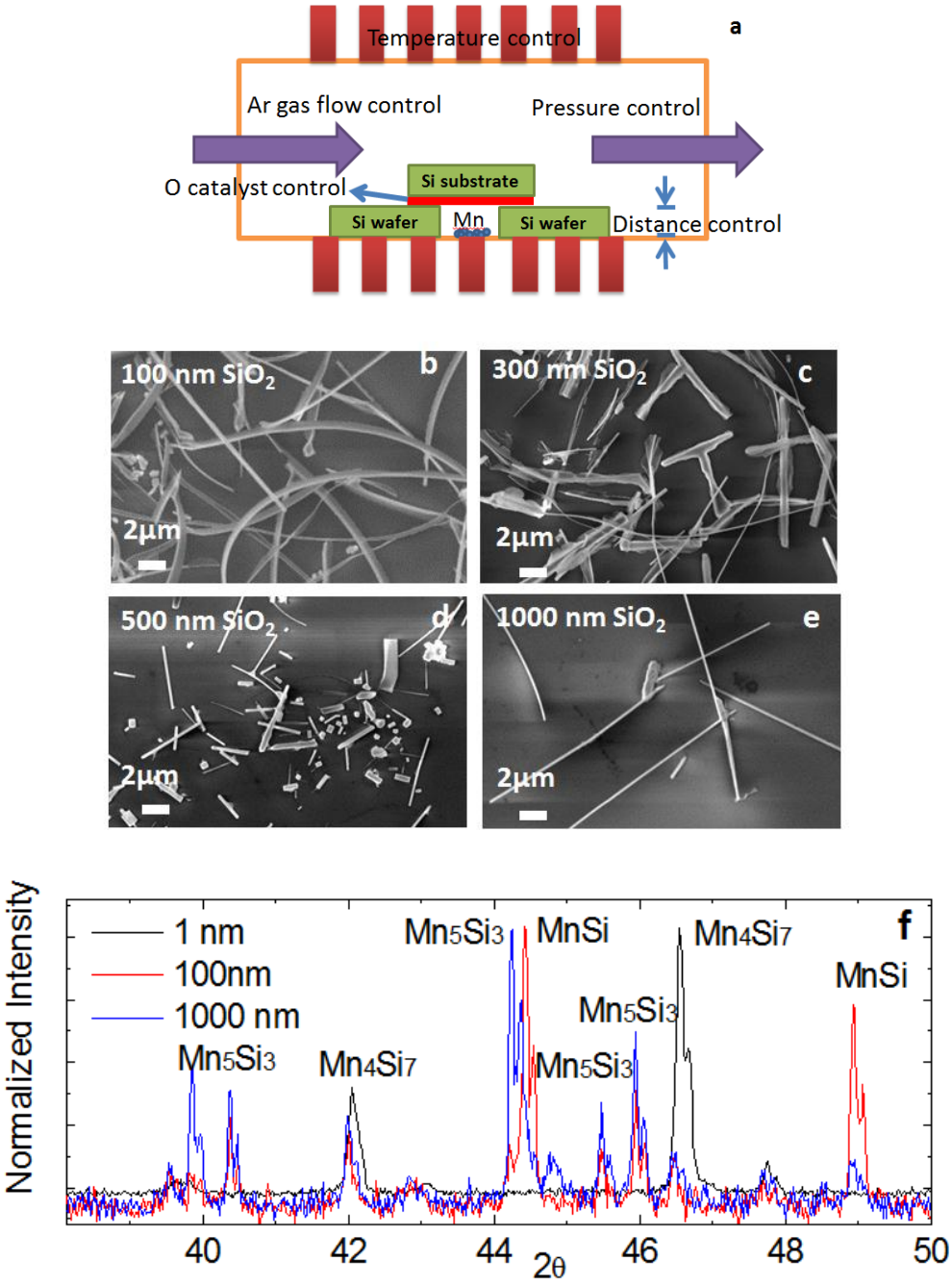


Figure 33 (a) Controlled parameter in oxide layer assisted CVD (b)-(e) Morphology comparison of nanowires prepared on substrate with different oxide thicknesses: 100nm, 300nm, 500nm, 1000nm (f)their XRD pattern.

Fig 33 and Fig 34 show the morphological, crystalline and compositional results from wafers with different oxidation layers. Fig 33(b) to (e) are the wires' SEM images from Si wafers with 100 nm, 300 nm, 500 nm and 1000 nm SiO_2 layers, respectively. Wires from the 100 nm SiO_2 wafer have the best morphology in terms of number, size uniformity and distribution on the surface. The crystalline structures of the wires on various SiO_2 thicknesses are very different too (Fig 33 (f)).

The Mn/Si composition ratio of the wires can be found using EDX analysis. Shown in Fig 34 (a) is a SEM image of nanowires grown on 100 nm SiO_2 at 850°C, for 80 minutes. TEM image and electron diffraction pattern confirm the single crystal nature of the wires. Fig 34 (f) shows the comparison of the EDX spectrum (normalized with Si peak) from samples with different oxide layer thicknesses. The quantified atomic ratio of Mn/Si from EDX depends on SiO_2 layer thickness, Mn/Si ratio varies from 0.6 (low oxide thickness) to around 5:3 (thickness of 200nm and above) (Fig 34 (g)). The EDS in SEM results is consistent with EDS in TEM.

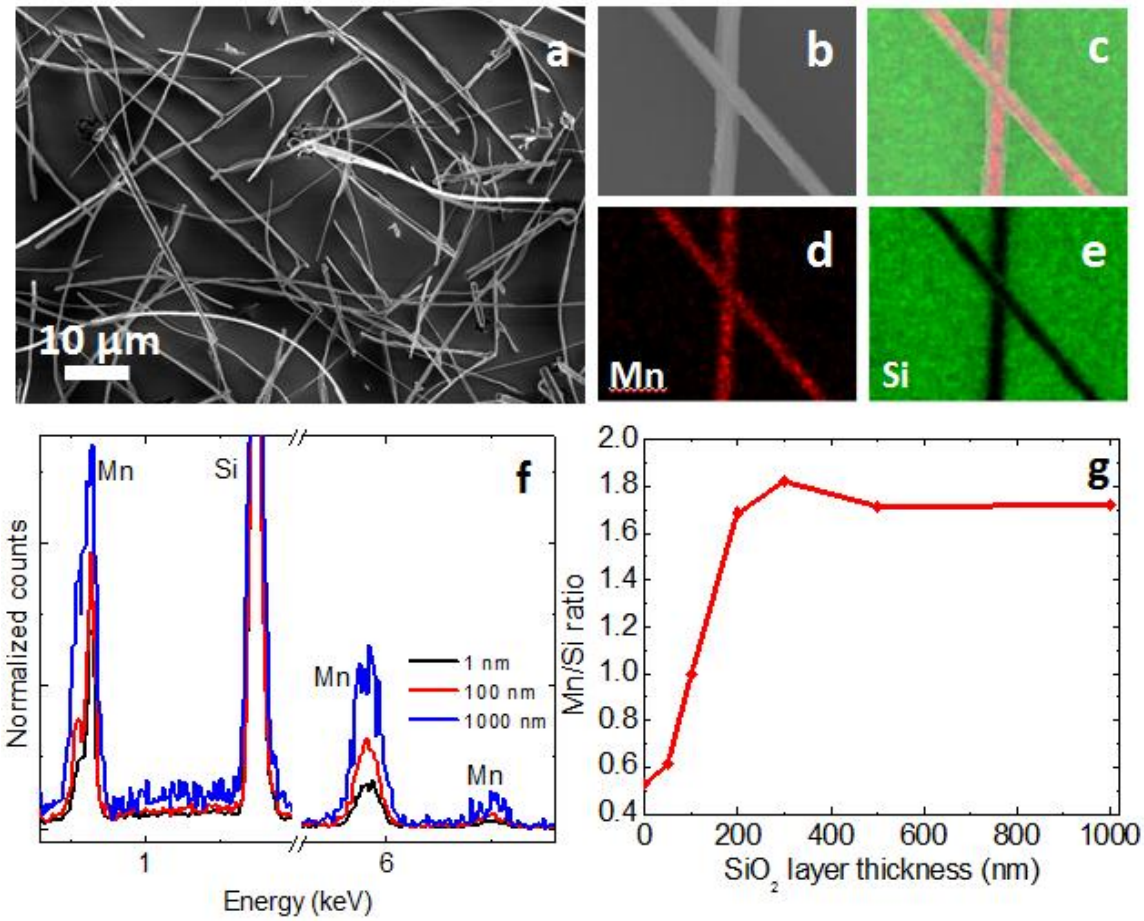


Figure 34 (a) Morphology of nanowires prepared under optimized parameters (b)-(e) Chemical composition mapping (f) Mn/Si composition comparison in different samples (g) Mn/Si ratio curves change with oxide thickness.

Samples were also prepared during different time periods: 40mins, 80 mins and 160 mins. Atomic compositions were compared in Fig 35 (a). The comparison of magnetization moments are shown in Fig 35 (b). The antiferromagnetic transition in 70K became weaker as time period as the time increased.

Samples were prepared at different source-substrate distances: 100μm, 500μm and 1500μm, which were controlled by supporting wafers, whose thickness was 500 μm. Therefore, distances were adjustable by laying one, two, three pieces of silicon wafers,. Nanowires became short, smaller and more oxidized.(Fig 36 (a)-(d)) The composition showed higher concentrations of Mn when the distance was smaller.(Fig 36(e)) Magnetization did not show any differences within those samples (Fig 36(f)).

Samples were prepared at varying temperatures: 750°C, 800°C, 850°C, 900°C, and 950°C. The nanowire's shape became more crystallized and straight when the temperature reached 950°C(Fig 37(a)-(d)); However, the manganese composition increased. (Fig 37(e)) Magnetization showed a transition at 70K decreased and 220K increased with rising reaction temperature (Fig 37(f)).

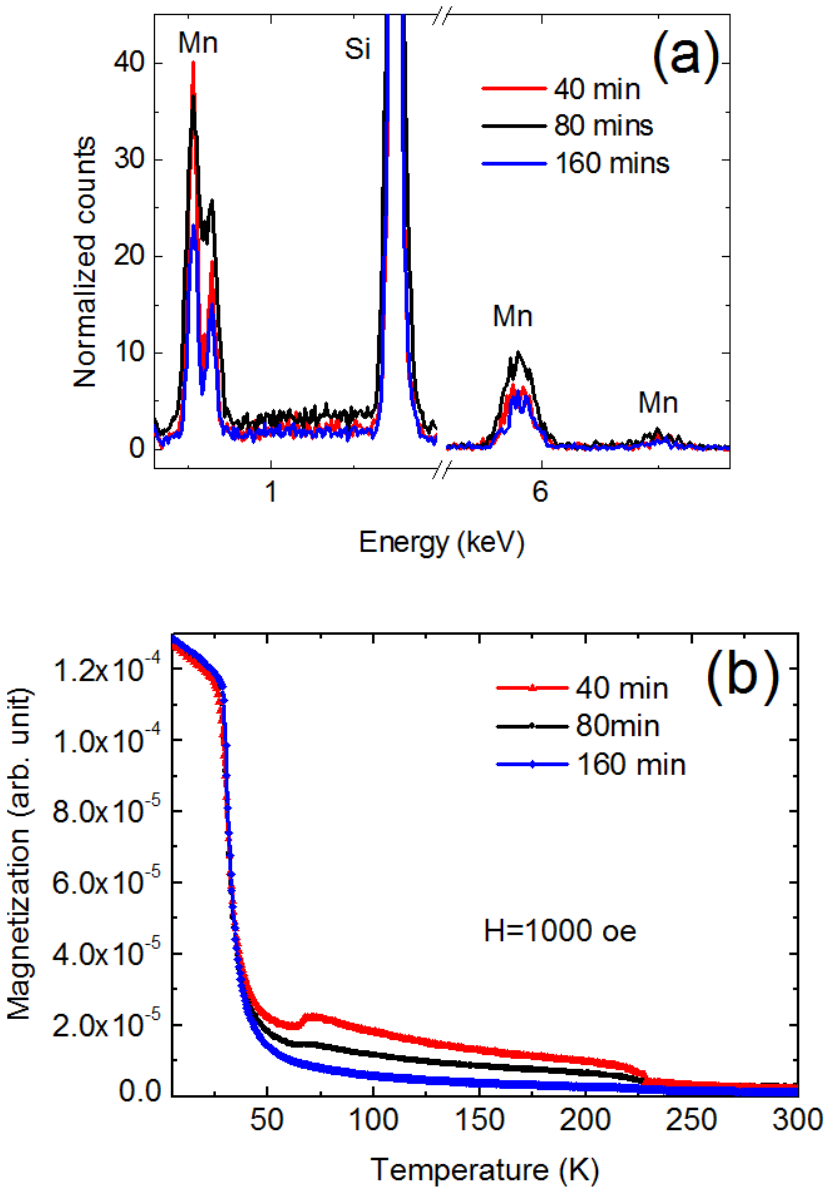


Figure 35 (a) EDX comparison (b) Magnetic measurement on nanowires prepared during different time periods: 40, 80 and 160 mins.

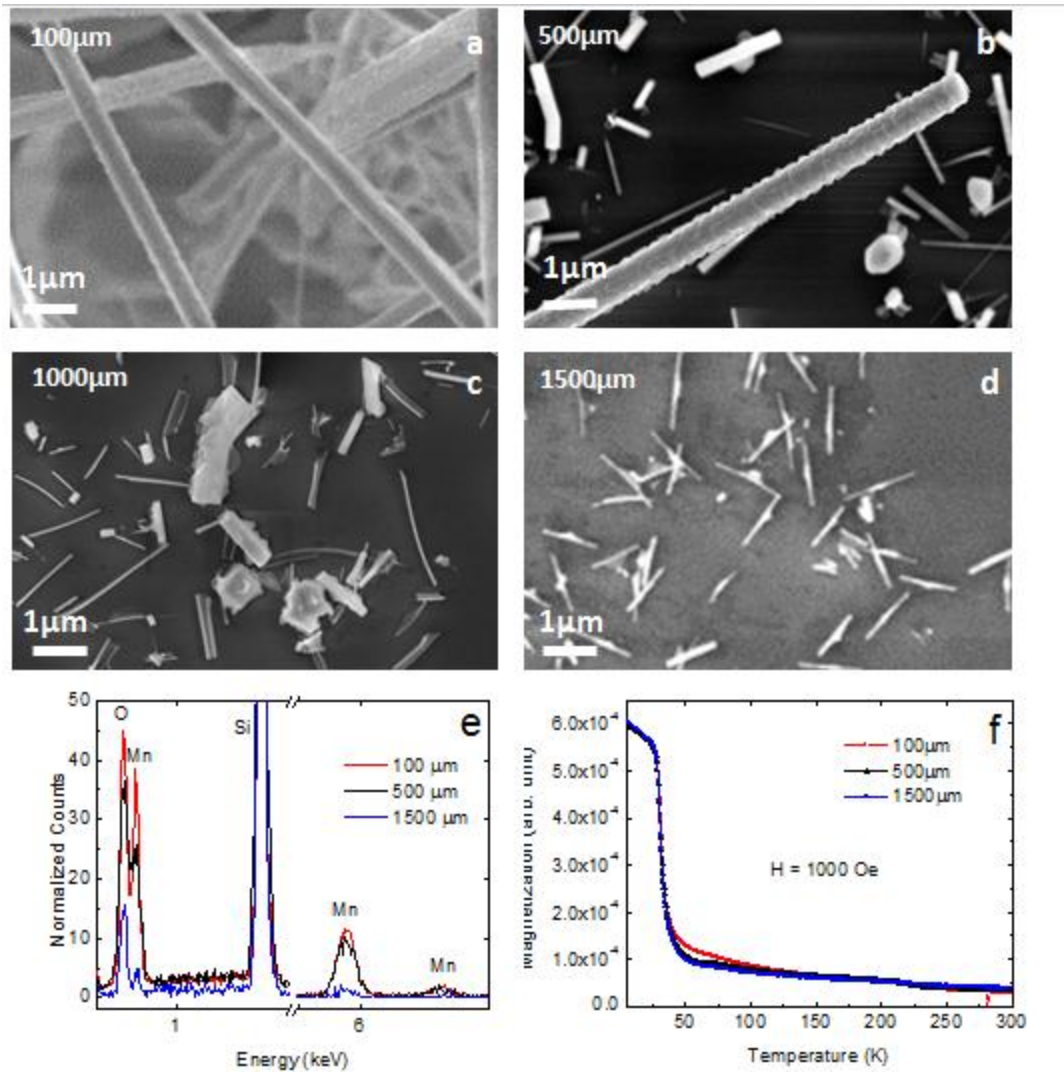


Figure 36(a)-(d) Morphology comparison (e)Composition comparison (f) Magnetic measurement on nanowires prepared during different distances from source to substrate: 100, 500 and 1500 µm.

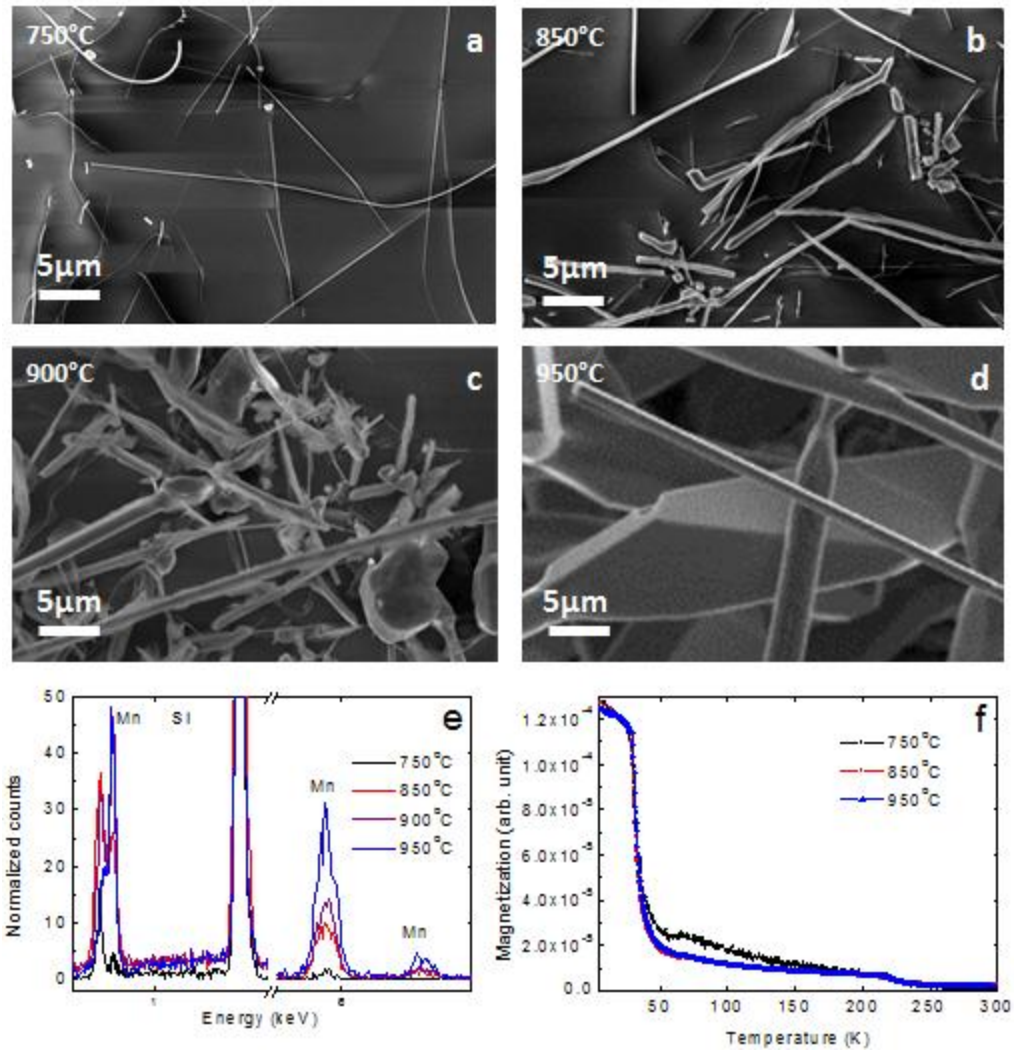
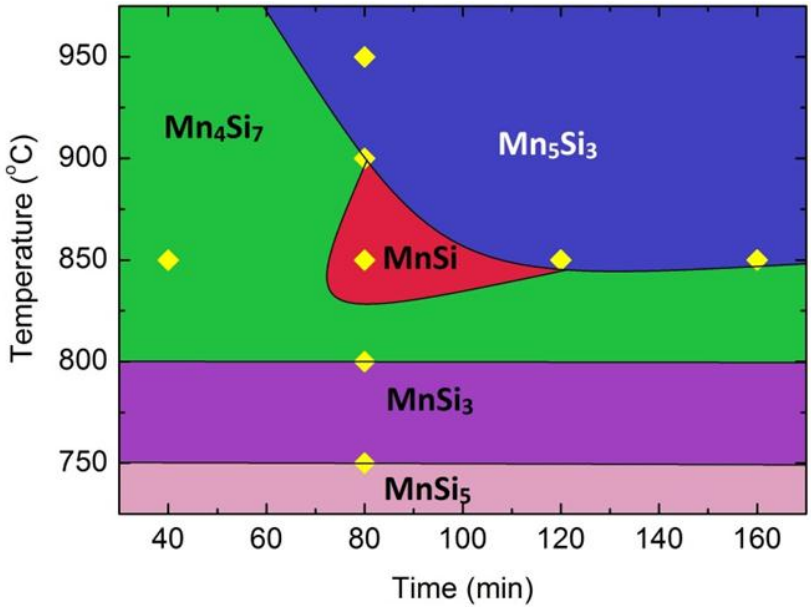


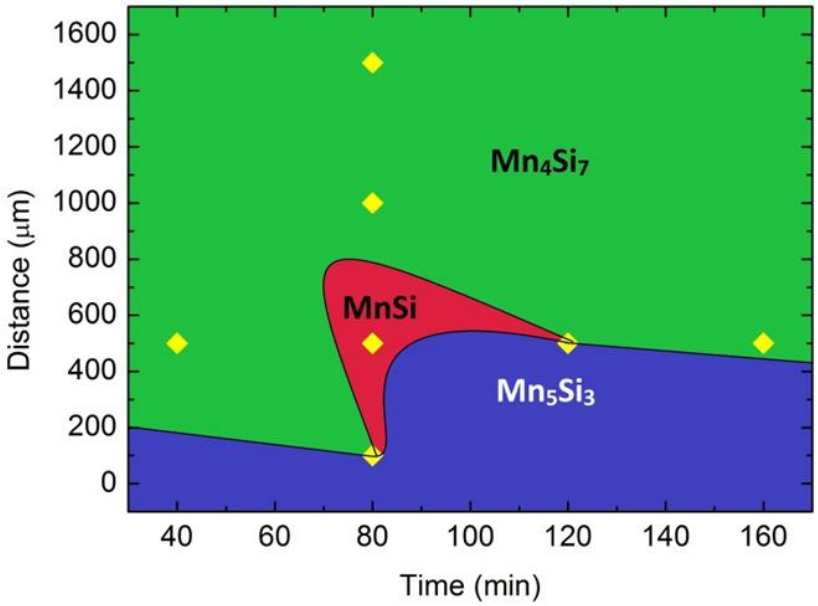
Figure 37 (a)-(d)Morphology comparison (e)Composition comparison (f) Magnetic measurement on nanowires prepared during different reaction temperatures: 750, 850, 900 and 950 °C.

Based on experimetns above, the MnSi nanowires with correct stoichiometry and B20 structure can be grown only under narrow growth conditions; any change of a single parameter leads to the change of the product structure and the composition dramatically because of the complexity of the growth process. A growth diagram (Fig.38 (a) and (b)) which combines multiple tuning parameters is necessary to optimize the growth conditions. Other than the oxidation layer thickness which was discussed above, the growth temperature, reaction time, and the distance between substrate and precursor, the vacuum pressure and gas flow rate were also systematically investigated. From the phase diagram, we can see that the B20 MnSi nanowires can only be grown in the red area. The width of the wires can be tuned from 100 nm to 600 nm by changing the growth temperature within the area.

The high yield one-dimensional growth could be qualitatively explained by the previous supersaturation theory, with the SiO_2 layers acting to control the supersaturation ratio. In order to enhance one-dimensional growth,



(a)



(b)

Figure 38 (a) Mn-Si nanowires growth phase diagram at various temperatures and times (b) Mn-Si nanowires growth phase diagram at various source-substrate distances and times.

Reducing temperature and supersaturation ratio could be two options for one-dimensional growth. While the growth temperature cannot be changed too much because of the activation energy of the phase formation, the supersaturation ratio can be tuned by the thickness of the SiO_2 layer. In this case the thicker the SiO_2 layer becomes the lower Si or SiO concentration becomes as these species need to diffuse from bottom to surface.

The exact experiment parameters are as follows: to pump the vacuum of the system down to a fixed pressure (for example, 3×10^{-2} torr in this study) before filling with Ar is the indispensable procedure to get reproducible growth. Mn powder was spread flat on the bottom of a porcelain crucible, Si (001) wafer with different SiO_2 thickness (0, 1, 50, 100, 200, 300, 500 and 1000 nm) was placed above (avoid direct contact) and face down to the Mn powder. The distance between the Mn powder and Si wafer was adjusted using layers of supporting wafers of Si to avoid contamination from other elements. The Mn powder was evaporated and deposited onto Si wafer under Ar gas flow. The gas flow rate was varied from 140 to 300 sccm (standard cubic centimeters per minute), and the pressure was maintained at 50 to 625 Torr. The syntheses were carried out at temperature between 750°C and 950°C,

lasting from 40 mins up to 160 mins. The hydrogen terminated Si wafers can be produced by HF acid etching which removes the native oxide [64], they are contamination-free and chemically stable for subsequent processing as the surface silicon atoms are covalently bonded to hydrogen. SiO_2 layers were thermally grown on Si substrates. A Zeiss Merlin Scanning electron microscopy (SEM) equipped with a Bruker SDD energy dispersed X-ray spectrometry (EDS) detector were used to characterize the microstructure and composition in this study. Transmission electron microscopy (TEM) was carried out on selected specimens, using a Hitachi HF-3300 TEM/STEM at 300 kV. All the nanowires were confirmed to be single crystal although in some cases wires were covered by an amorphous silicon dioxide layer. X-ray diffraction was used to confirm the primary phase of the samples (peaks of MnSi, Mn_5Si_3 and Mn_4Si_7). As the signal from the wires was very small compared to the substrate, the omega offset was set to 2-3° to minimize the signal from substrates. DC and ac magnetic properties of the synthesized material were characterized with a Quantum Design magnetic property measurement system (MPMS) [65,66].

5.4 Magnetic measurement and verification of skyrmion

The magnetic measurements of the samples support the structural and compositional results. Shown in Fig.39 (a) are the magnetization curves near the 29 K helimagnetic transition plotted on an expanded scale. The transition is clearly apparent for the MnSi wires grown on 100 nm SiO_2 layer measured at 10 Oe. The cusp close to T_c is the clear signature of the formation of the helical state, which only exists at small field (the cusp disappears when the field exceeds 1000 Oe) [22] [67]. The magnetic measurements were done with magnetic field parallel and perpendicular to the surface of the wafer (in-plane and out-of-plane).In this case, nanowires grow randomly, but they have been taped off the original growth substrate and then transfered onto another clean silicon wafer to avoid magnetic signals from growth substrate. The tape has been pressed to assure the nanowires locate on the plane of clean wafer so that in plane and out of

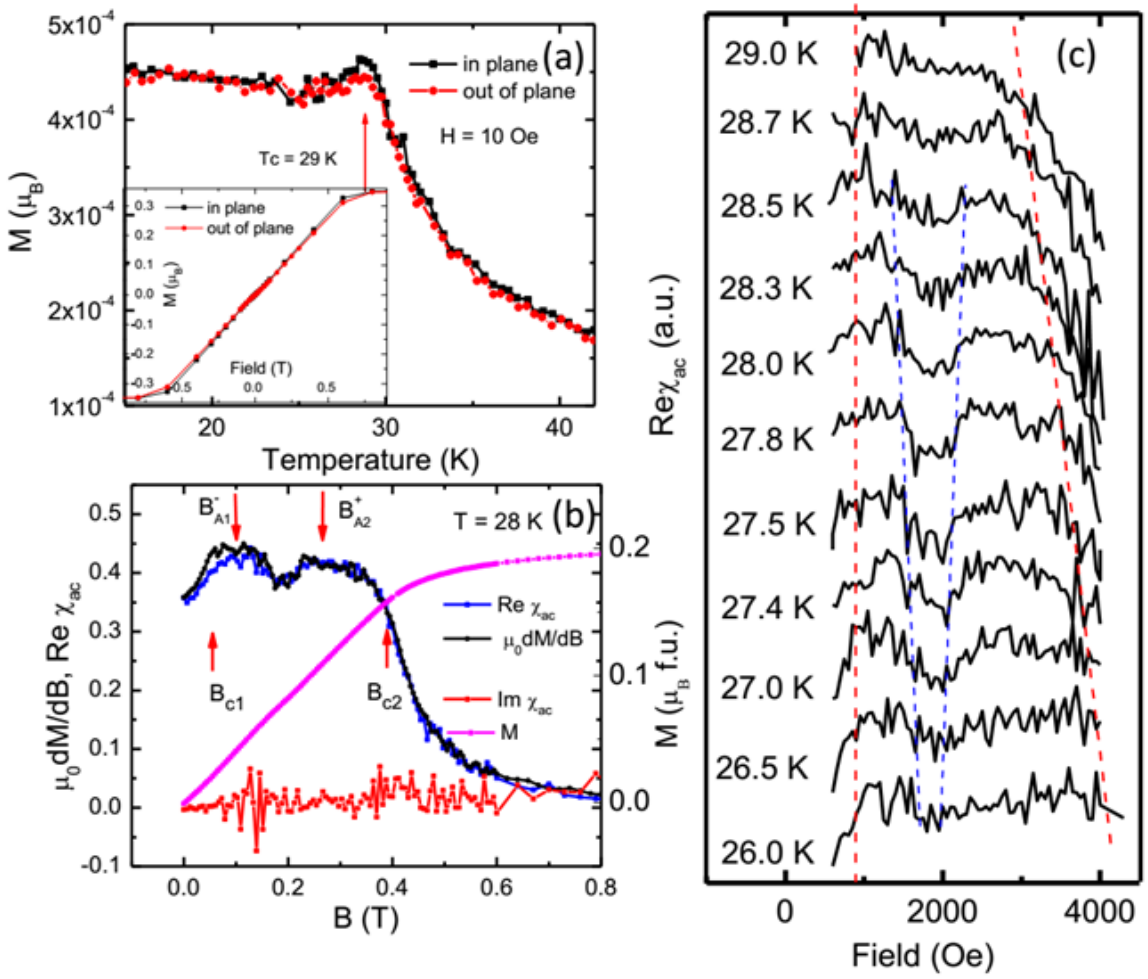


Figure 39 DC and ac magnetizations of the MnSi nanowires. (a) In and out of the plane anisotropic magnetizations (see text for definition) under DC field of 10 Oe. The kink around 29 K is the signature of helical magnetic. The inset shows the field dependent of the magnetization at 10K. (b) Comparison of the ac susceptibility Re $\boldsymbol{\chi_{ac}}$(blue), Im $\boldsymbol{\chi_{ac}}$(red) with the susceptibility μ_0dM/dB calculated from the field dependence magnetization M (purple, right Y axis) at 28K. The isothermal ac susceptibility is as a function of field measured under excitation field of

1 Oe and 8Hz ac magnetic field applied in-plane at 28K. (c) Evolution of the Re $\boldsymbol{\chi_{ac}}$ approaching from 26 K to T_c 29 K. The blue and red dash-lines are guiding lines for the B_{c1}, B_{c2} and $\mathbf{B_{A1}^{-}}$,$\mathbf{B_{A2}^{+}}$.

plane data could be measured. We anticipate the anisotropic magnetization of the wires can be indirectly extracted out by thinking that the majority of the wires are aligned on the surface of wafer, so the out-of-plane data show the property perpendicular to the wires; while the in-plane data show the azimuthal average of all wires. From both temperature dependent and field dependent data in Fig. 39 (a), the magnetic behavior in-plane looks a little bit stronger than out-of-plane. The growth direction of the wires is [110] [53,68], the helical domains point out of the (111) face, which is 35° from (110). So the projection of the helical contribution out-of-plane is around 71% of the in-plane contribution. This is likely the reason for the small difference in the two directions although as addressed above the magnetic data is the average of the wires. Further studies using local techniques such as micro SQUID are necessary to fully quantify the magnetic anisotropy.

The isothermal ac susceptibility and DC magnetization as a function of magnetic field confirm the existence of the skyrmion phase (A phase) in the nanowires. The Fig.39 (b) shows the comparison of the ac susceptibility with the susceptibility $\mu_0 dM/dB$ calculated from the DC magnetization M at 28K, just below the transition temperature. The isothermal ac susceptibility as a function of field was measured under

an excitation amplitude of 1 Oe and 8Hz ac magnetic field applied in-plane. Measurements performed as magnetic field is increasing and decreasing show characteristic features which have been shown to be signatures of the A phase [30] [28,69–72]. Other than the reduced value of ac susceptibility, we also observed the extra peaks in the μ_0dM/dB which is the characteritic feature of the phase transition as detailed explained in Ref [28]. The μ_0dM/dB curve shows two lower kink regions (700-1150 Oe and 1150 -2300 Oe) and three transition maxima (700, 1150, 2300 Oe). By increasing the field, magnetic structure goes through helical to conical (from B_{C1} toB_{A1}^{-}), then conical to A phase (in betweenB_{A1}^{-}, B_{A2}^{+}). At 26.5 K, the first maxima in the μ_0dM/dB which represents the helical to conical transition is still available, but the two peaks relate to the A phase transition almost disappear. Please note that as the mass of the nanowires are much smaller (0.06 mg for the sample shown) than the bulk single crystals, the signal-to-noise ratio of the data is not as good as that of the literature [28]. Other than the extra noise, our data is consistent with the above-mentioned reference.

The field dependence of the ac susceptibility Reχ_{ac} and DC magnetization changes strongly in the narrow temperature window

from 26 K to 28.5K and for B ≤ 4000 Oe. Fig. 39(c) shows the evolution of the $Re\chi_{ac}$ approaching form low T to T_c. The blue and red dash-lines are eye-guiding lines for the B_{c1}, B_{c2} and B_{A1}^{-}, B_{A2}^{+}. At 26K, there is a shallow dip in the middle; a well-pronounced local minimum has developed near 27.8K. The characteristic feature is present up to 28.5K and by 29K is completely smeared.

In conclusion, the growth conditions of Mn-Si nanowires have been studied. Different Mn-Si compositions can be selected by tuning growth parameters. The key parameter for stoichiometric and crystalline correct high yield growth of B20 MnSi wires is the thickness of the SiO_2 layer. A growth phase diagram was constructed that provides a systematic guide for controllable selective growth of nanowires with different compositions. The dM/dH curve along with ac and DC magnetic properties of MnSi nanowires reveal the presence of helimagnetic and skyrmion magnetic ordering in the one-dimensional wires.

CHAPTER 6 SYNTHESIS AND CHARACTERIZATION OF IRON GERMANIDE NANOWIRES

6.1 Nanostructures synthesis in initial stage

Several precursors were tried in Fe-Ge nanowires preparations. [73,74] Solution methods were also used to create iron germanide nanowires. [75]

In chemical vapor deposition, the temperature for powder evaporation and product phase stabilization made controlling morphology, composition and structure difficult. The initial purpose was to prepare the cubic FeGe phase, which has the same structure as MnSi and exhibit skyrimon near room temperature (280K). [31]

The Fe-Ge phase diagram, shown in Figure40, is much more complicated than the Mn-Si phase diagram. When the atomic composition of iron equals germanium, three structures exist: monoclinic, hexagonal and cubic. The temperature boundary between hexagonal and cubic is 630°C. Therefore, the substrate temperature should not exceed 600°C. [76]

Precursors of Fe powder, Ge powder, $GeCl_2$, GeI_2 and Cr-FeGe powder were tried in a vacuum. These precursors were also applied at atmospheric pressure on a Ge wafer, a Ge wafer covered with Cr thin film, an iron foil and a Si wafer with oxide; however, none of the depositions were successful. The temperature was kept relatively low at 600°C.

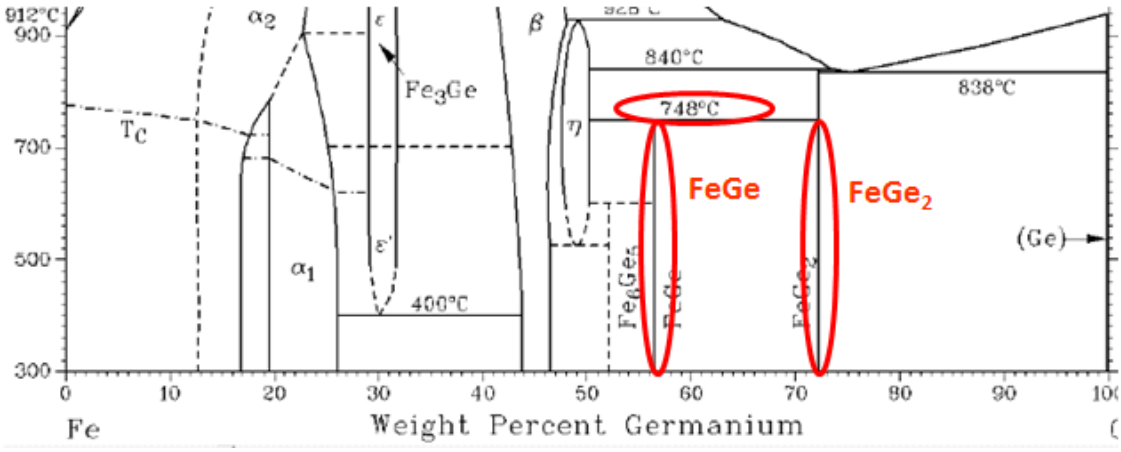


Figure 40 Fe-Ge phase diagram [77].

Successfully prepared Cr-FeGe powder, which showed an X-ray diffraction pattern the same as that of cubic FeGe by adding a small amount of CrGe to hexagonal FeGe powder before annealing for several weeks, was prepared. Hexagonal FeGe seems to follow the structure of CrGe, which is the same structure as MnSi and cubic FeGe. Therefore, a thin layer was deposited approximately 2-9nm on the Ge wafer by using e-beam evaporator, and then the layer is melted using laser irradiation. The purpose of this procedure was to create CrGe nanoparticles on the Ge wafer through laser melting and Ge diffusion. FeGe powder could prefer a growth area where CrGe nanoparticles are located, resulting in longitude one-dimensional growth. In that case, cubic FeGe nanowires' diameter should be determined by the Cr-Ge nanoparticles' size. For Cr film approximately 9 nm thick (Fig 41 (a)), the substrate after laser irradiation showed that the concentration of Cr in this method could be as high as 10% on nanoparticles and 0.1% elsewhere. The maximum particle diameter was approximately 322 nm.

The real challenge, however, was in determining how to make the concentration exactly 1:1 on nanoparticles. Many experiments have been attempted to deposit Cr-FeGe powder directly onto the substrate with Cr or Cr-Ge nanoparticles (Fig 41 (b)(c)). A wire-like structure (Fig

41(d)) has been observed on the substrate after deposition at 570°C, and ,600 Torr for 30 mins. That structure was 200 nm long and 20 nm wide. However, the wire-like structure disappeared after 3 hours of deposition.

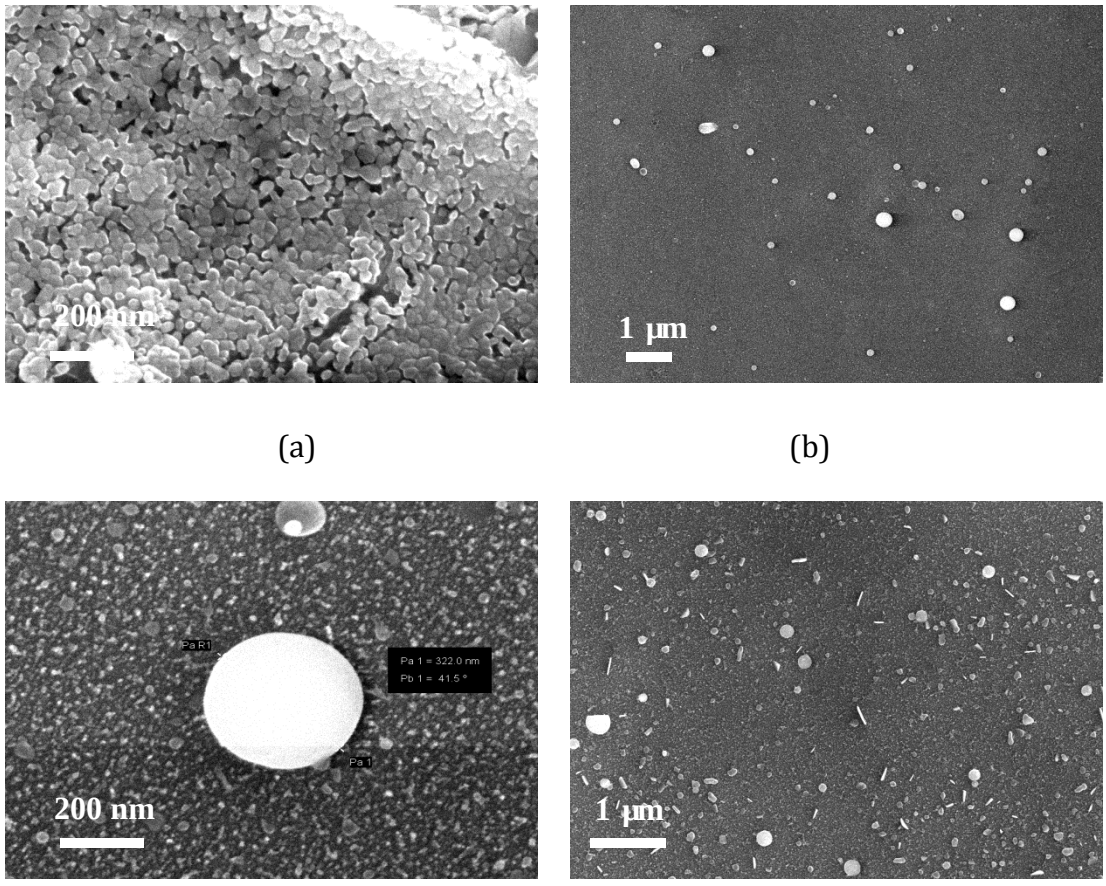
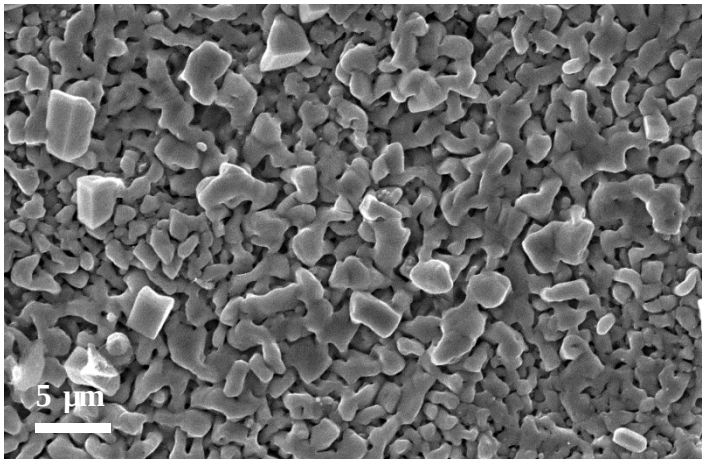


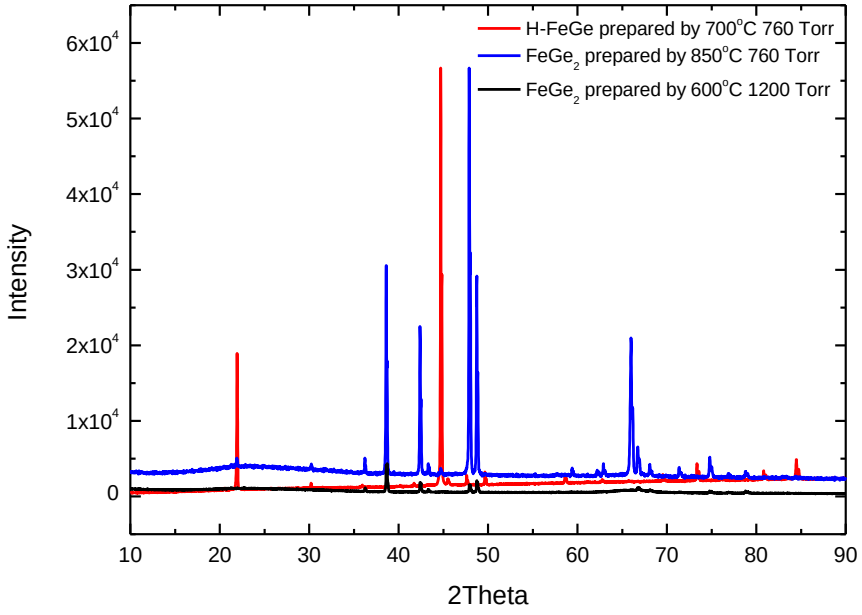
Figure 41 (a) 9 nm Cr thin film deposited on Ge wafer (b) Nanoparticles prepared after laser irradiation (c) Diameter of a nanoparticle (d) Nanorod structure growth by direct deposit Cr-FeGe on Cr-Ge wafer at 570°C.

Metal halide is easy to purchase and prepare in contrast to organometallic compounds ,but it lacks stoichiometry control. Ferric chloride ($FeCl_3$) and ferrous chloride ($FeCl_2$) were both tried in order to promote nanowire growth. They could not be stored in air due to moisture absorption. Using Ferric chloride, in atmospheric pressure, it still resulted in too many iron compounds gathering on the substrate, which formed a very thick layer of $FeGe_2$. This layer could transform from $FeGe_2$ to hexagonal FeGe as the reaction temperature was lowered from 850°C to 700°C with pressure at 760 Torr. The XRD pattern matched these two phases (Fig 42) . However, the main signal from the substrate became $FeGe_2$ again as the inner pressure increased to 2000 Torr at 600°C. This increase could be explained by the mean free path of Fe decreasing with more gas molecules. Thus, less Fe reached the Ge wafer forming $FeGe_2$. The growth boundary between hexagonal FeGe and $FeGe_2$ was about 550°C with 1200 Torr inner pressure. Based on this fact, lower temperature and higher pressure were required for both the cubic phase and one dimensional growing. Though the glass tubes and pressure gauge could not sustain too much inner pressure, growth of overpressure estimated around 935-2000 Torr was attempted in this study. Samples prepared at pressure around 1200±50 Torr finally

showed some nanowire growth. But, resulted in the pressure gauge's malfunction. The Ge wafer was put in the middle of the furnace and $FeCl_3$ powder 1.5cm from the opening. The other parameters used were 600°C, 140 sccm, and 30 mins. The pressure was unstable in this nanowire synthesis.



(a)



(b)

Figure 42 (a)SEM image showing morhology of $FeGe_2$ layered structure (b)XRD pattern of thick layer prepared on 700°C and 850°C(760 Torr) and 600°C(1200 Torr).

6.2 Structure verification and chemical composition of $FeGe_2$ nanowires

$FeGe_2$ nanowires were synthesized for the first time by CVD at 600°C and at pressure approximately 1800Torr (Fig 43). The morphology showed nanowires growing everywhere (Fig 44(a)). The center of the substrate was totally white, and couldnot reflect light. The nanowires' diameter was uniform at approximately 200-300nm, and their length was approximately 10μm.(Fig44(b))

In the X-ray diffraction, the peaks were identified as $FeGe_2$, mainly from the substrate (Fig 45). With nanowires transferred to the copper grid via acetone, TEM was used to identify the nanowires' structure (Fig 46). Comparing the diffraction pattern, the zone axis matched to $FeGe_2$ [001]. The atomic plane was indexed by the diffraction pattern and high resolution TEM images. By comparing the nanowires' relative position to the atomic plane, the growth direction was found to be [110]. Researchers from ORNL's main campus helped with TEM measurements. Five nanowires were measured, and all of their diffraction patterns were identified as $FeGe_2$.

The nanowires were measured by EDX, and the atomic composition of Fe:Ge was very close to 1:2. Typical peaks of iron and germanium are plotted in Fig 47.

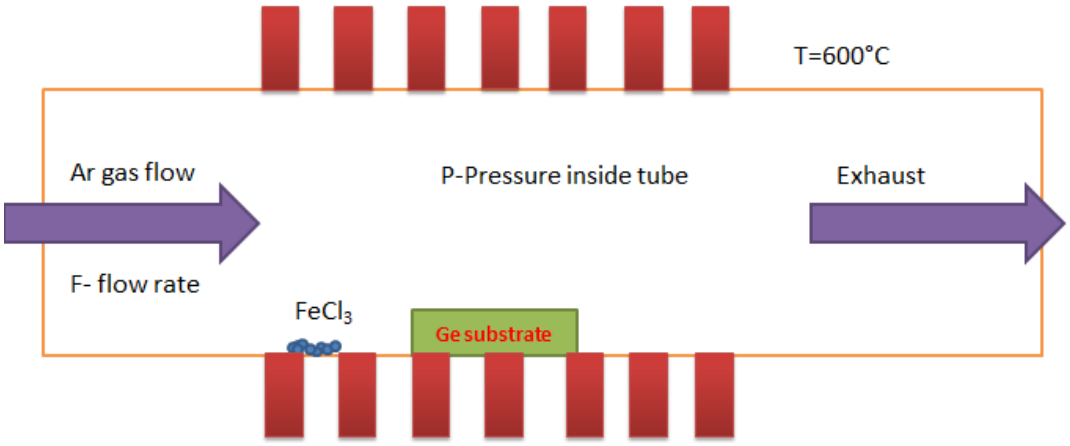
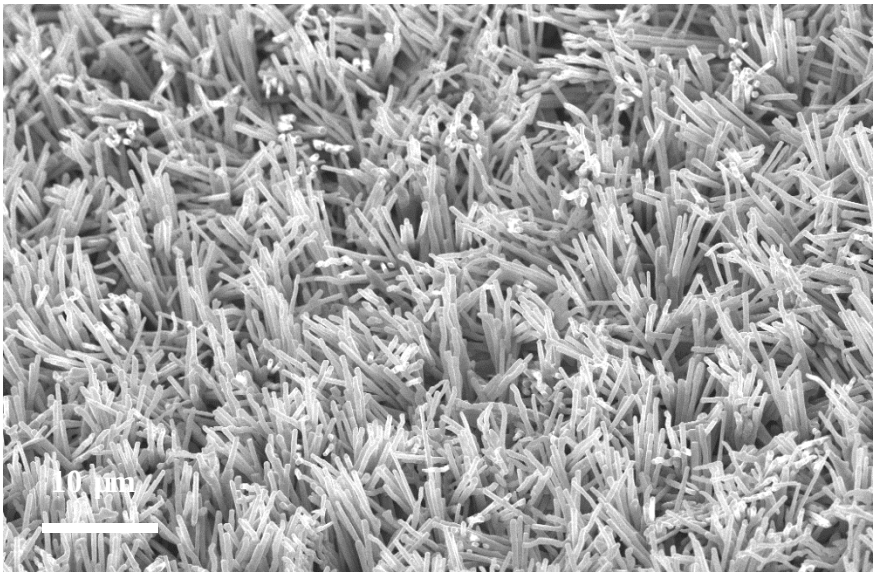
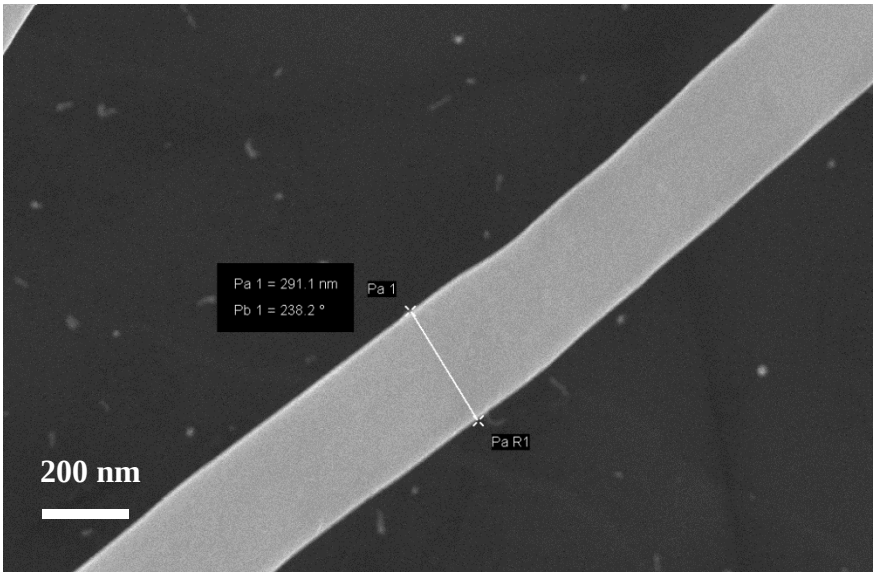


Figure 43 Souce-substrate geometry with Ar works as carrier gas



(a)



(b)

Figure 44 (a)Nanowires prepared with the thick $FeGe_2$ layer in the middle. (b)The diamter of $FeGe_2$ nanowire.

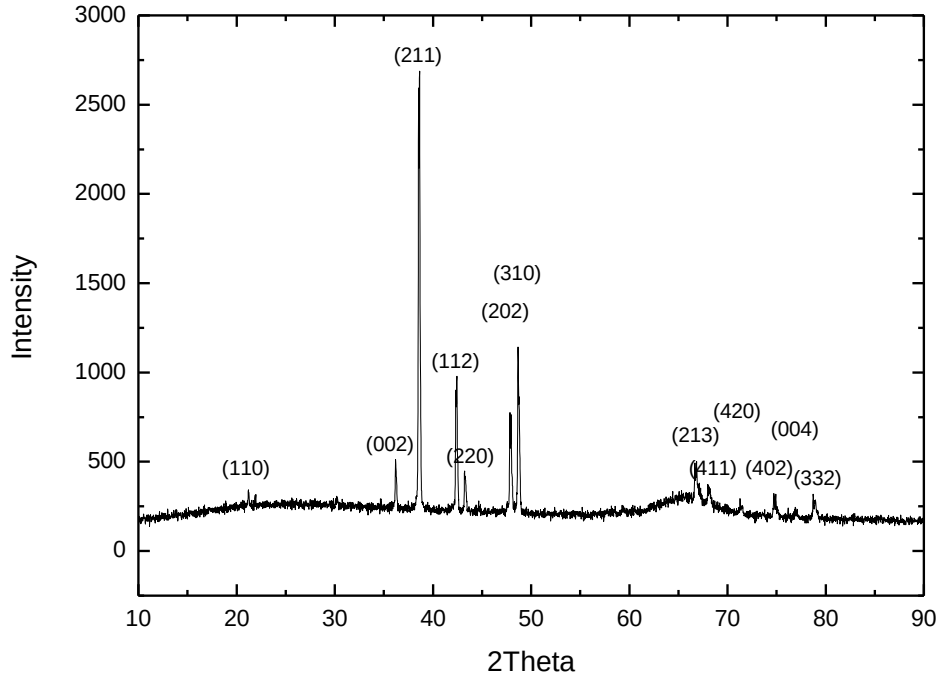
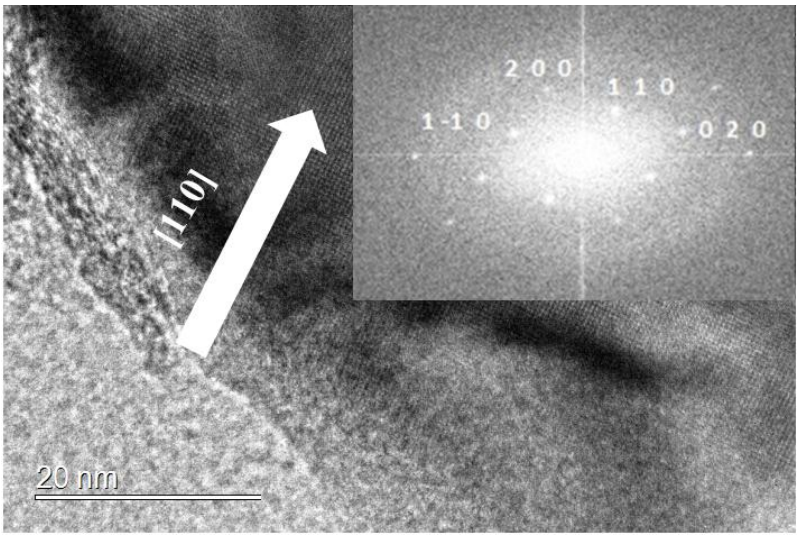
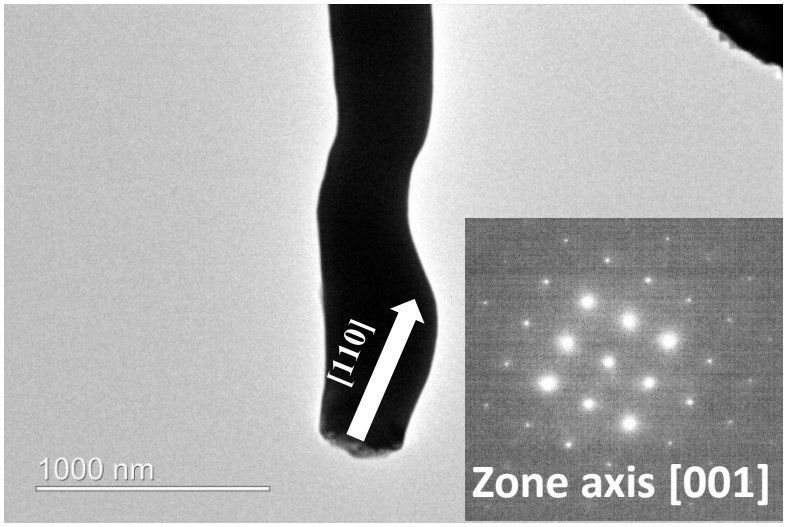


Figure 45 Indexed XRD pattern shows the peaks matching $FeGe_2$.



(a)



(b)

Figure 46 (a) High resolution TEM images of $FeGe_2$ nanowires. The inset is the FFT of HRTEM images (b) Growth direction of nanowires is identified as [110]. The inset is the diffraction pattern with zone axis [001].

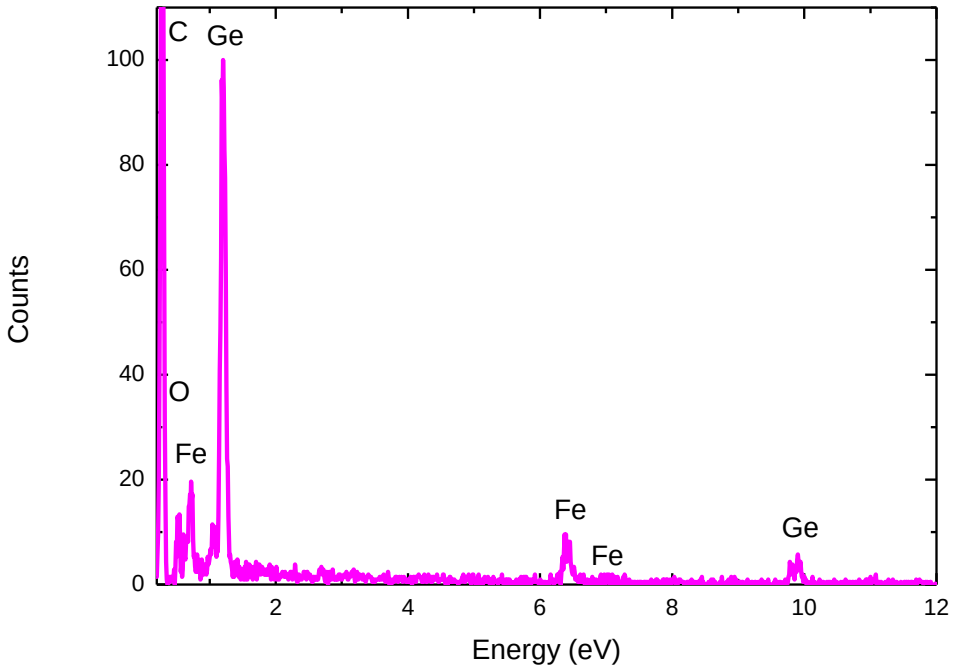


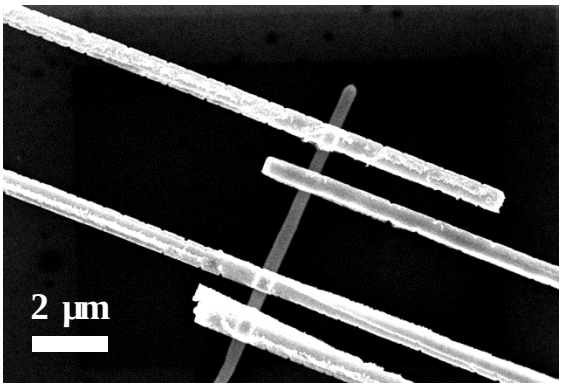
Figure 47 Relative height of iron peak compared to Ge peak along $FeGe_2$ nanowires.

6.3 Transport properties and magnetic measurement of $FeGe_2$ nanowires

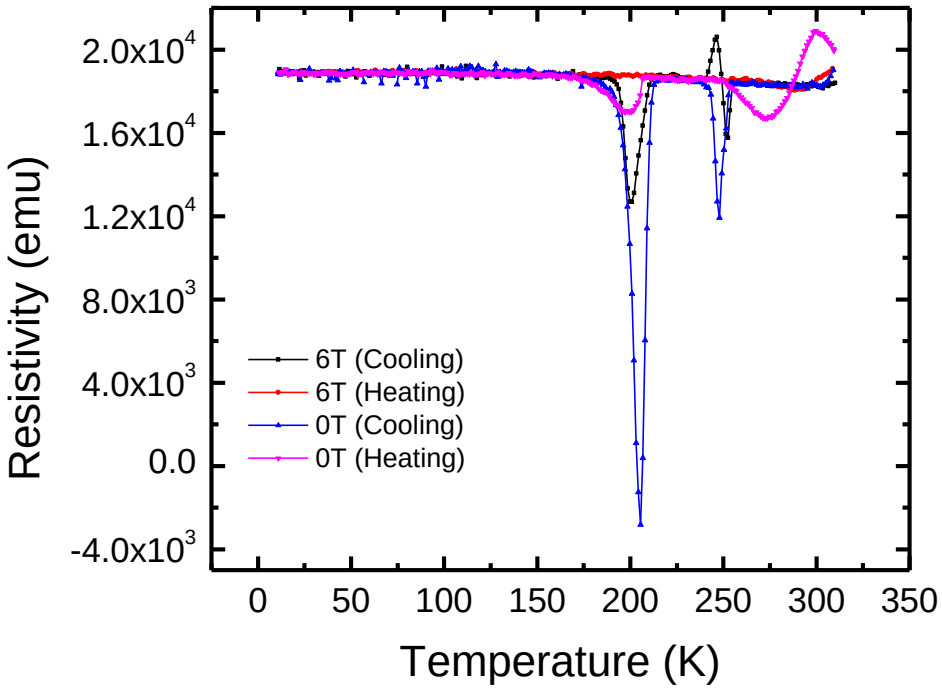
XRD and TEM both verified that the layer and nanowires were $FeGe_2$. The nanowires' growth direction was [110]. Therefore, to measure the nanowires' transport properties, a four-probe single-nanowire device was measured by PPMS at 0 tesla and 6 tesla applied along [001] direction. For each magnetic field, resistance was measured with sample cooling from 310K to 10K and then returning to 310K. The currents of 100nA, 500nA, and 1uA were used; but the background noise was excessive. A current of 2 μA was applied along the nanowires.

The resulting resistance is plotted in Fig 48(b). Cooling from 310K to 10K, the resistance showed two peaks at approximately 200K and 250K. By applying a magnetic field to 6 tesla, the peaks lowered. In the process of warming the sample from 10 to 310K, the peak of 200K appeared at 0T. Both peaks disappeared at 6T.

Furthermore, resistance did not change in two temperature ranges: 0-180K and 218-237K. As a result, to ensure the data was accurate, resistance was measured at several temperature points. As shown in Fig 49, the resistance of 10K was about the same as that of 230K .



(a)



(b)

Figure 48 (a) Four-probe nanodevice (b) Resistivity measured with a magnetic field of 0 and 6 Telsa. Both of them include a cooling and heating process.

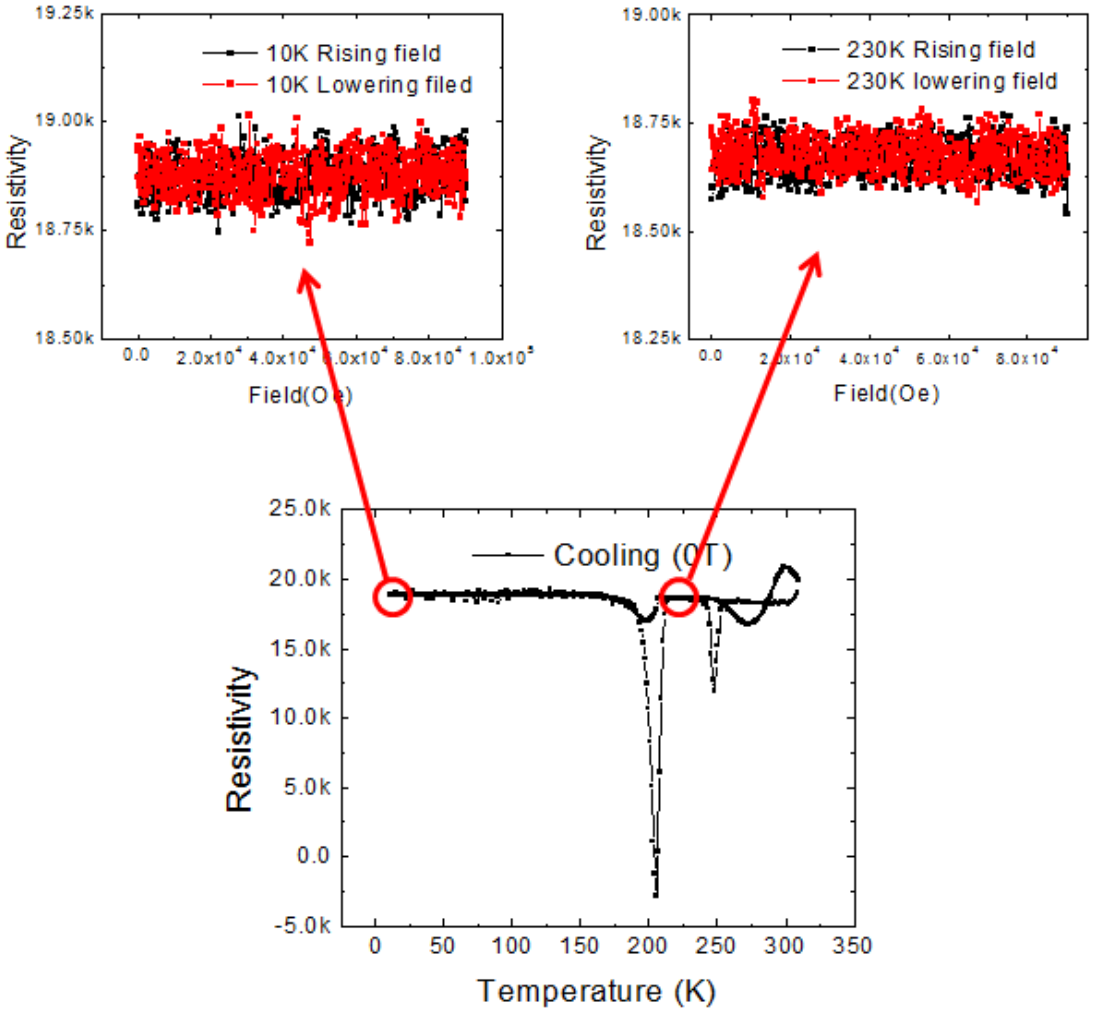


Figure 49 Resistivity measurement at 0T cooling from 310K to 10K: Two temperature points (10K and 230K) were chosen to compare magnitudes in two separate constant resistivity ranges (0-180K and 218-237K). Each temperature point has two curves with magnetic field rising from 0-9T and returning to 0T.

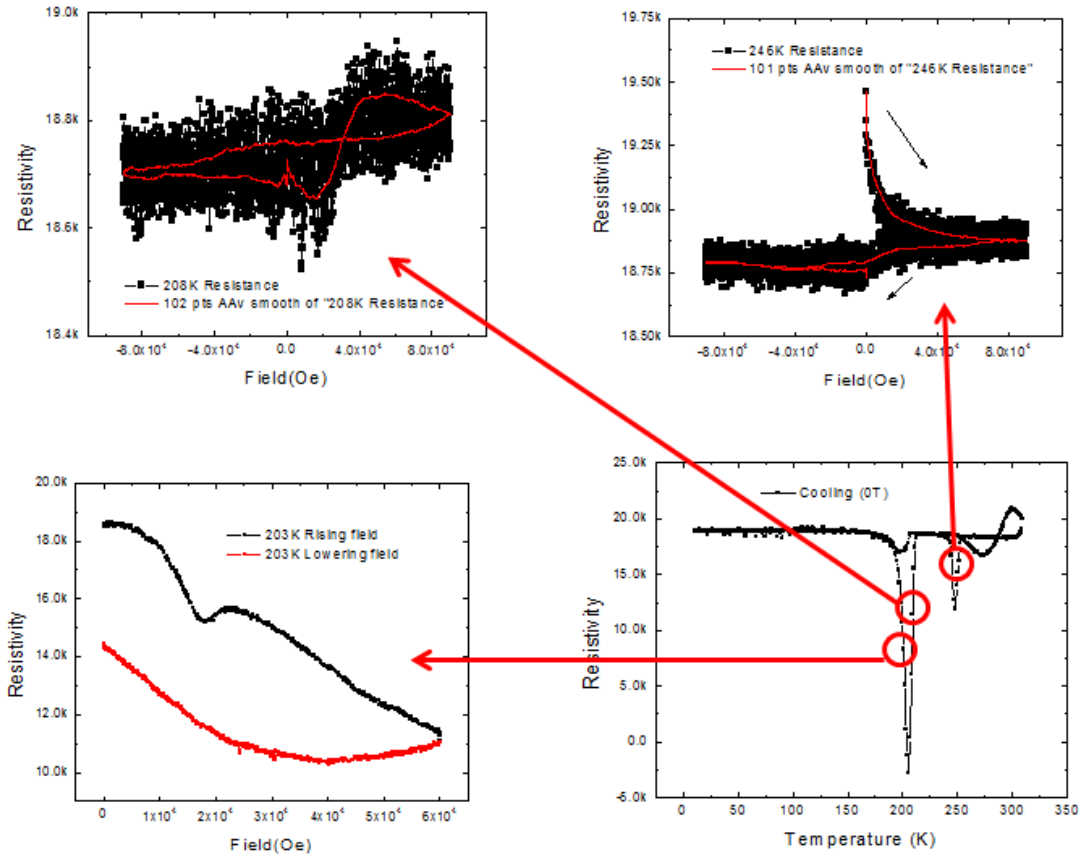
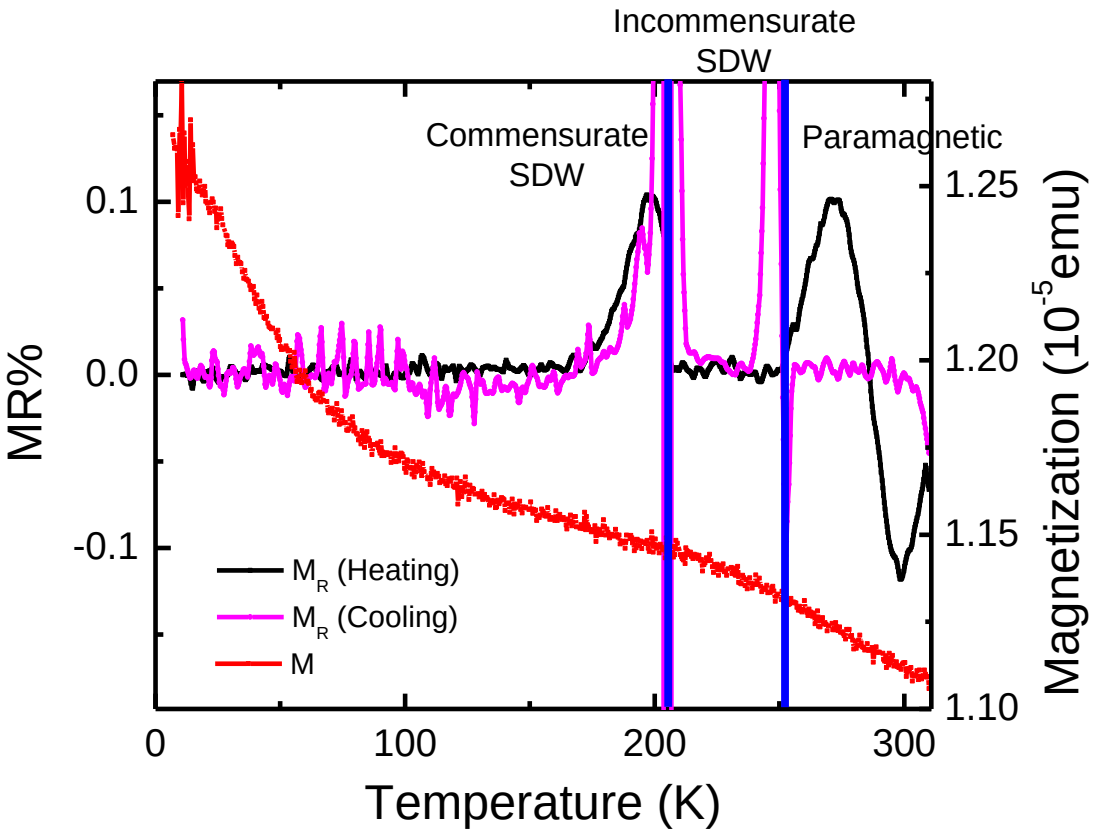
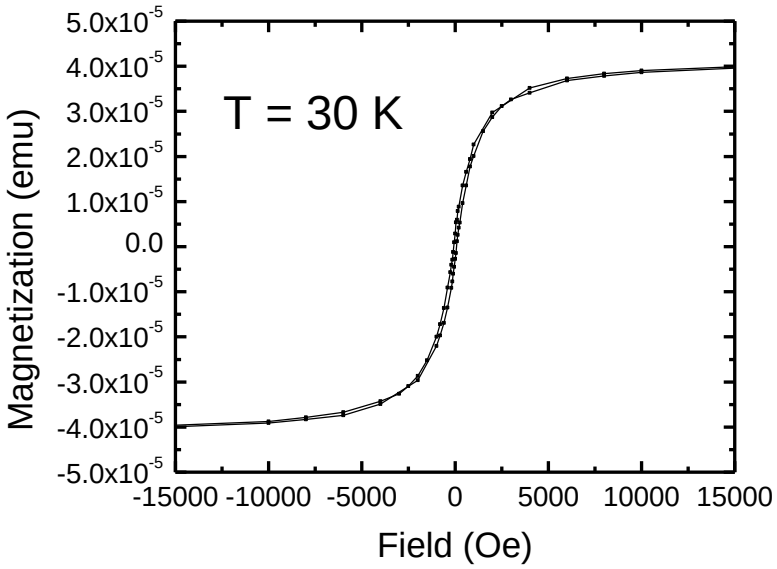


Figure 50 Resistivity measurement at 0T cooling from 310K to 10K: Three temperature points (203K, 208K and 246K) were chosen to compare transition in peak resistivity regimes. Each temperature point has two curves with the magnetic field rising and falling. A smooth fit was used to eliminate noises.

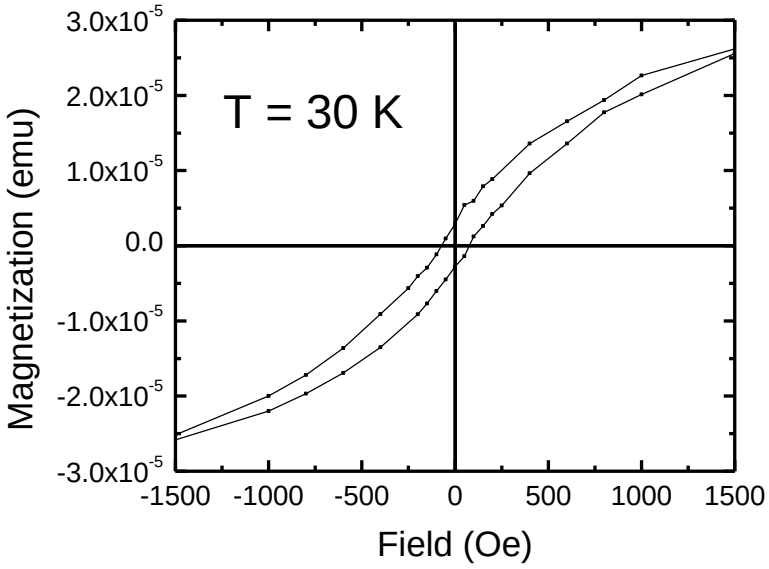


(a)

Figure 51 (a) The magnetoresistance and magnetic moments reveal two transition temperatures at 205.5K and 252.4K.



(a)



(b)

Figure 52 (a) M-H hysteresis curves at 30K, (b) Enlargement of M-H hysteresis curves from -1500oe to 1500oe.

In Fig 50, the resistance shows hysteresis behaviors with a changing magnetic field at temperature points of 203, 208, and 246K. At 203K, when raising the magnetic field, a similar shift of resistance was noticed compared to the bulk $FeGe_2$ measurement. SDW transition should cause this shift. However, the resistance tendency was totally reversed in constrast with bulk.

As shown in Figure 51, magnetoresistance was calculated from the previous resistivity measured under 0T and 6T, clearly showing two sharp peaks of resistivity. By aligning their maximum value, two transition temperatures, 205.5 and 252.4K, were identified.

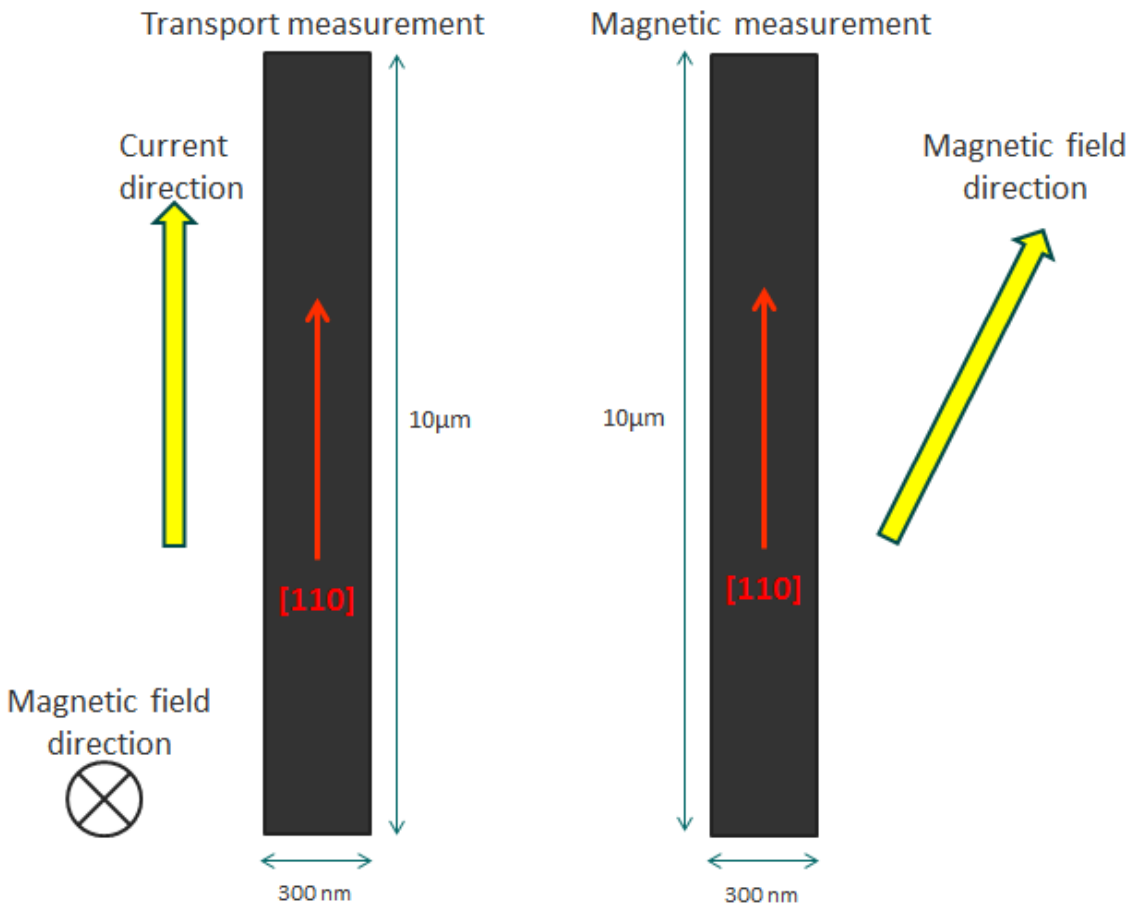
Compared to bulk $FeGe_2$, it was reasonable to conclude these two temperatures mark the boundary of incommensurate SDW and commensurate SDW. Those temperatures in bulk $FeGe_2$ were 263 and 289K. The resistivity changed because the material tranfromed to a magnetic superzone state. The superzone boundaries of magnetic order with periodicity are different from the atomic lattice's chemical periodicity. Therefore, the superzone has extra scattering of charge carriers leading to abnormal resistivity change [51]. In this case, the superzone was incommensurate SDW state.

A carbon tape was used to attach the substrate's surface. Nanowires were attached to the tape which was attached to another clean silicon wafer so that, the magnetization sigals of nanowires could be measured. Magnetic moments versus temperature measured in red lines (Fig 51) represent a ferromagnetic transition around 200K. As shown in Fig 52(a), magnetization was measured with a changing magnetic field at 30K. The magetization showed a saturation at a magnetic field of 5000 oe confirming the ferromagnetism.

The magetic field was applied parallel to the plane of silicon substrate in the magnetic measurement. The nanowires were attached onto this plane, but they were randomly oriented. The magnetic field in the transport measurement was along [001] direction,but the current flowed along [110] direcion.

Therefore, when measuring along the nanowire's elongation direction, the transport data showed that SDW state in antiferromagentism (Fig 53) . The magnetic properties measured were dominated by signals along the nanowire's other direction. The elongation direction was in micrometer range because it grew along [110] direction, but other directions were in nanometer range meaning that the cross-section cut by the magnetic field was hundreds of nanometers. This result could be

explained as nanoscale effect along other directions broke down antiferromagnetism, resulting in ferromagnetism emerged.



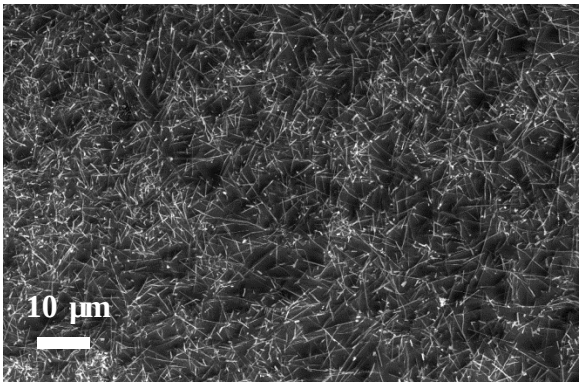
(a) (b)

Figure 53 (a) Magnetic-field direction and current-flow direction in transport measurements (b) Magnetic-field direction in magnetic measurement

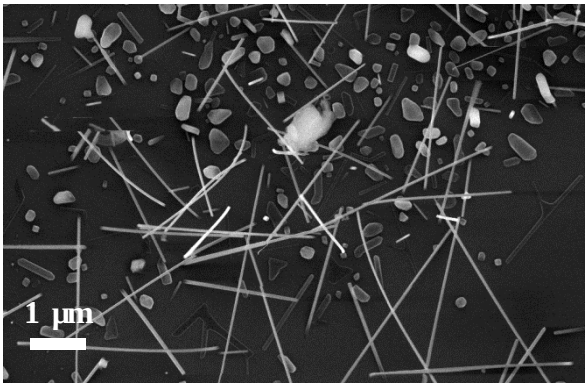
CHAPTER 7 OTHER NANOWIRES PREPARED BY CVD

7.1 Fe_2Si and Cr_5Si_3 nanowires

The oxide synthesize method, might become a common way of synthesizing metal silicide nanowires. Iron powder and chromium powder were deposited on the SiO_2/Si wafer (850°C, 140 sccm, 80 mins, 650 Torr). SiO_2 thin films of 100 nm on silicon wafer was used and nanowires containing Fe-Si and Cr-Si elements were verified (Fig 54) .From EDX data, nanophase of Fe_2Si and $Cr_5Si_3$was estimated to be among the sample. (Fig 55)

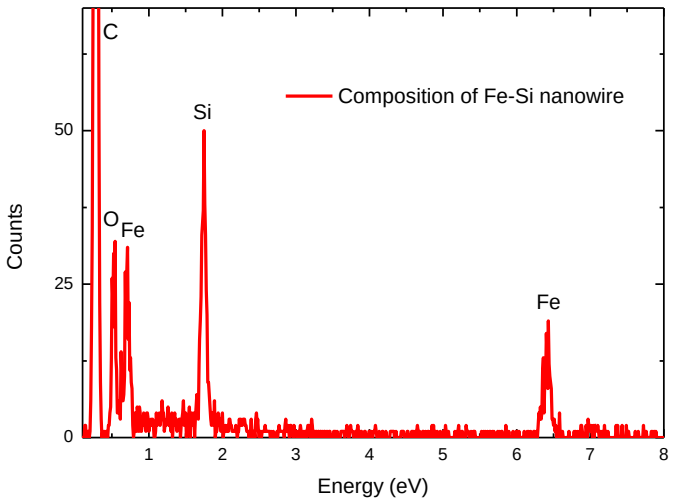


(a)

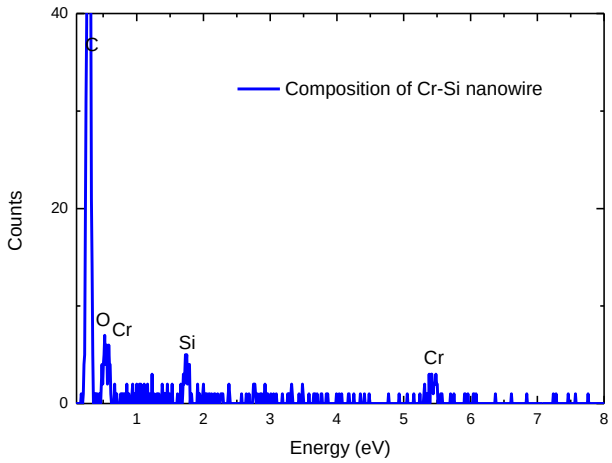


(b)

Figure 54 (a) Fe_2Si nanowires (b) Cr_5Si_3 nanowires prepared by metal powder deposited on a silicon wafer with an oxide layer.



(a)

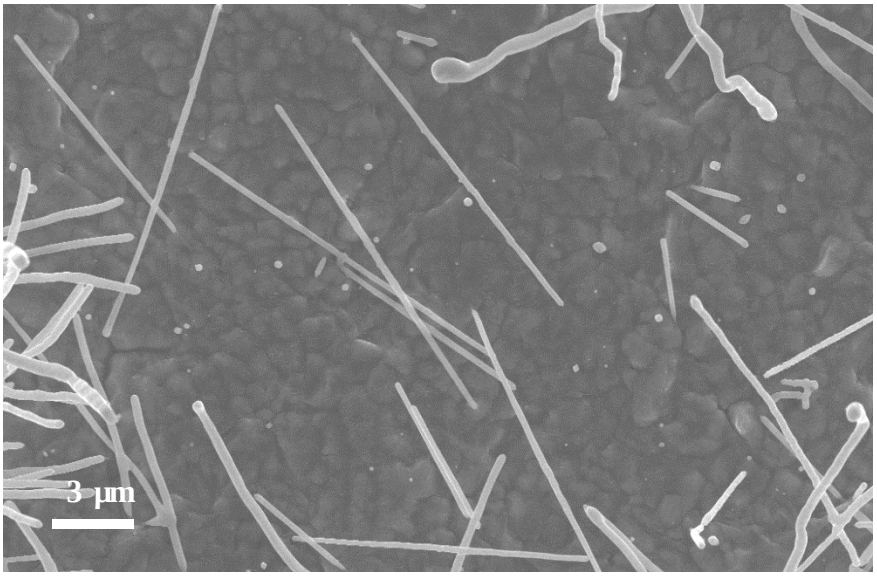


(b)

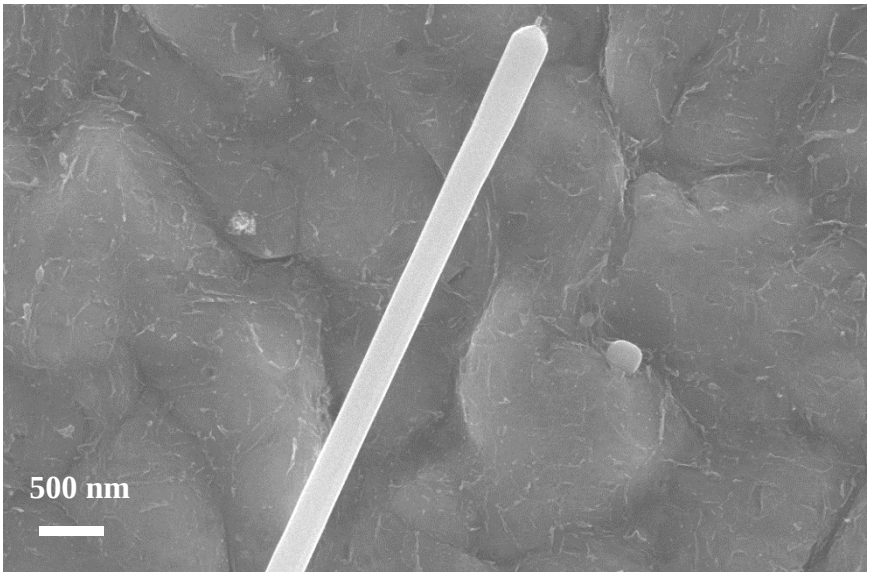
Figure 55 Composition of nanowires on carbon tape gives the atomic ratio (a) Fe_2Si (b) Cr_5Si_3.

7.2 Synthesis of $Fe_{2.5}Ge$ nanowires

With the pressure in the $FeGe_2$ nanowires' preparation reduced to 1200 Torr, the nanowires'morphology was as follows: Nanowires concentrated at the substrate's corners; and the middle substrate showed a very thin layer of $FeGe_2$, which could reflect visible light. Nanowires (diameter of 100-250nm) were very straight and long (10-15μm). (Fig 56); The composition showed a very high percentage of iron contained along these nanowires. The average atomic ratio of Fe:Ge=2.5:1 (Fig 57(a)). Magnetic measurements showed a ferromagnetic transition around 250K in zero field cool; however, T_c of bulk iron germanide as high as 500K has been obtained when the composition of iron reached 1.9. Even higher T_c was expected with iron reach to 2.5 Fig 57(b) [78,79]

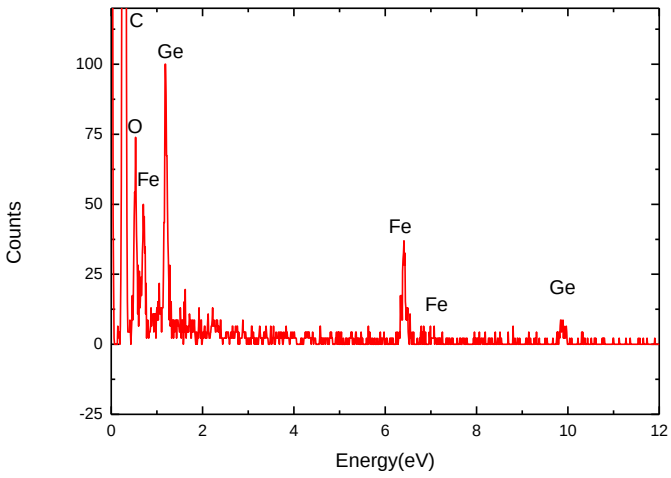


(a)

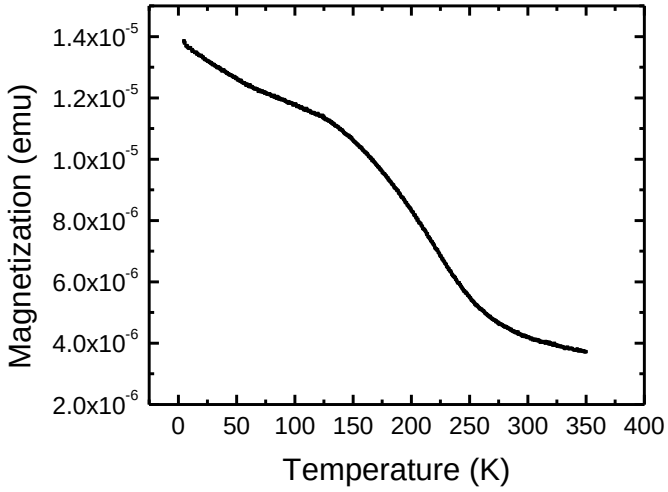


(b)

Figure 56 $Fe_{2.5}Ge$ Nanowires prepared with less $FeGe_2$ layer in middle.



(a)

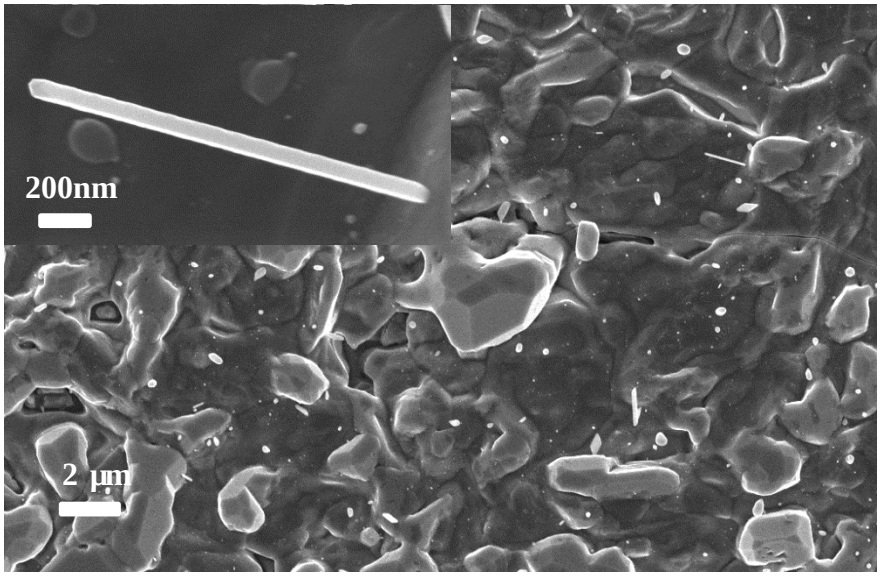


(b)

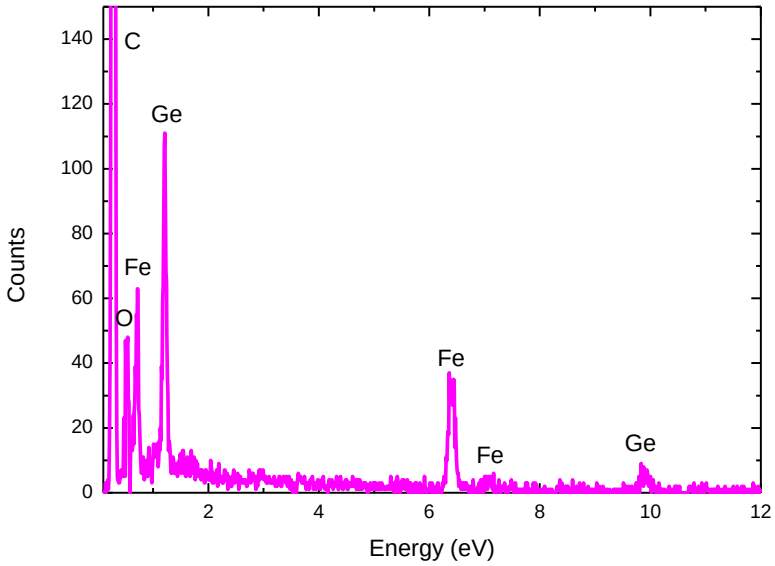
Figure 57 (a)Peaks of Fe and Ge measured along the nanowires with atomic ratio at 2.5:1 (b) Magnetic moments versus temperature measured on the whole substrate with magnetic field at 1000 oe.

7.3 Fe_3Ge nanowires

Small numbers of nanowires have been synthesized in a Ge wafer by directly depositing iron powder onto it. Low pressure around 30-100 mTorr has been applied with and the temperature kept at 600°C. (Fig 58(a)) The nanowires were thin (50-150 nm) and short (1-3 μm). The composition verified by EDS was around 3:1 (Fe:Ge),(Fig 58(b))however, its number was small and needed to be more precisely controlled to get dense growth.



(a)



(b)

Figure 58 (a) Fe_3Ge nanowires prepared on Ge wafer (b) Composition verified by EDX.

CHAPTER 8 CONCLUSION

Magnetic nanowires were prepared in a home-built chemical vapor deposition system, and novel magnetic and electronic transport properties were studied.

1. MnSi and $FeGe_2$ nanowires' massive growth emphasizes the importance of the supersaturation ratio. The initial exploration usually resulted in substrates with thick layer. A combination of source materials and substrate was restricted by adding an intermediate SiO_2 layer and reducing the amount of evaporated iron, both of which suppressed the supersaturation ratio from two-dimensional to one-dimensional growth. The oxide layer assisting nanowires' growth has the potential of becoming a common method of preparing metal silicide nanowires.

2. Based on a controlled amount of Si, the growth diagram on Mn-Si nanowires via oxide-assisted growth was plotted by adjusting other parameters like temperature, pressure, distance from source to substrate, time and flow rate. Low field M-T measurements identified

helimagnetic nanowires. Transformation from helimagnetic structure to skyrmion lattice was observed in ac susceptibility measurements.

3. A single $FeGe_2$ nanowire was fabricated into four probe nanodevices via e-beam lithography. However, lift-off problems existed due to nanowires' large diameter. By adjusting the process's dose and layer geometry, nanodevice was manufactured.

4. The magnetic and transport properties of $FeGe_2$ nanowires showed significant divergence with bulk $FeGe_2$ [80,81]: lowering the SDW transition temperature and broadening the ICSDW phase. When the field was applied on [001] direction and the current flew in [110] direction [82], the SDW was also proven by shift resistance. The magnetic measurements showed ferromagnetism when field was applied along the substrate plane. Ferromagnetism could be interpreted as the nanoscale effect breaking down antiferromagnetism along any directions except [110], resulting in emergnece of ferromagnetism. SDW could be driven to slide with applying a magnetic field or electric field. This sliding showed an option of manipulate electron spins in antiferromagnetic materials. [83–85]

REFERENCES

[1] Farzad Nasirpouri, *NANOMAGNETISM AND SPINTRONICS: Fabrication, Materials, Characterization and Applications* (World Scientific Publishing Co. Pte. Ltd, 2009).

[2] A. P. Guimar˜aes, *Principles of Nanomagnetism* (Springer, 2009).

[3] T. Shinjo, *Nanomagnetism and Spintronics* (Elsevier Science, 2009).

[4] D. L. Mills, *Nanomagnetism* (Elsevier Science, 2006).

[5] Y. Xia, P. Yang, Y. Sun, Y. Wu, B. Mayers, B. Gates, Y. Yin, F. Kim, and H. Yan, Adv. Mater. **15**, 353 (2003).

[6] X. Fang, J. Mater. Sci. Technol. **22**, 1 (2006).

[7] G.W.Sears, Acta Metall. **3**, 361 (1955).

[8] S.S.Brenner, Acta Metall. **4**, 268 (1956).

[9] V. G. Dubrovskii, N. V. Sibirev, J. C. Harmand, and F. Glas, Phys. Rev. B **78**, 235301 (2008).

[10] S. V. N. T. Kuchibhatla, a. S. Karakoti, D. Bera, and S. Seal, Prog. Mater. Sci. **52**, 699 (2007).

[11] Y. Hu, J. Phys. Chem. B **109**, 4398 (2005).

[12] Z.R.Dai, Adv. Funct. Mater. **13**, 9 (2003).

[13] Z. W. Pan, Z. R. Dai, and Z. L. Wang, Science **291**, 1947 (2001).

[14] I. Dzyaloshinsky, J. Phys. Chem. Solids **4**, 241 (1958).

[15] Toru Moriya, Phys. Rev. **120**, 91 (1960).

[16] S. V. Maleyev, J. Magn. Magn. Mater. **310**, 1602 (2007).

[17] S. Chutia, M. Friesen, and R. Joynt, 1 (2006).

[18] K. Matan, B. Bartlett, J. Helton, V. Sikolenko, S. Mat'aš, K. Prokeš, Y. Chen, J. Lynn, D. Grohol, T. Sato, M. Tokunaga, D. Nocera, and Y. Lee, Phys. Rev. B **83**, (2011).

[19] A. S. T. Pires and M. E. Gouve, J. Magn. Magn. Mater. **212**, 251 (2000).

[20] P. B. and M. H. Jensen, J. Phys. C **13**, 881 (1980).

[21] Landau L D, *Statistical Physics* (New York: Pergamon, 1977).

[22] S. Mühlbauer, B. Binz, F. Jonietz, C. Pfleiderer, a Rosch, a Neubauer, R. Georgii, and P. Böni, Science **323**, 915 (2009).

[23] Soshin chikazumi, *Physics of Ferromagnetism* (Oxford University press, 1997).

[24] H. Wong, **43210**, 1 (2002).

[25] a. Neubauer, C. Pfleiderer, B. Binz, a. Rosch, R. Ritz, P. Niklowitz, and P. Böni, Phys. Rev. Lett. **102**, 186602 (2009).

[26] S. Seki, X. Z. Yu, S. Ishiwata, and Y. Tokura, Science **336**, 198 (2012).

[27] X. Yu, J. P. DeGrave, Y. Hara, T. Hara, S. Jin, and Y. Tokura, Nano Lett. **13**, 3755 (2013).

[28] a. Bauer and C. Pfleiderer, Phys. Rev. B **85**, 214418 (2012).

[29] S. X. Huang and C. L. Chien, Phys. Rev. Lett. **108**, 267201 (2012).

[30] H. Wilhelm, M. Baenitz, M. Schmidt, U. K. Rößler, a. a. Leonov, and a. N. Bogdanov, Phys. Rev. Lett. **107**, 127203 (2011).

[31] X. Z. Yu, N. Kanazawa, Y. Onose, K. Kimoto, W. Z. Zhang, S. Ishiwata, Y. Matsui, and Y. Tokura, Nat. Mater. **10**, 106 (2011).

[32] X. Z. Yu, N. Kanazawa, W. Z. Zhang, T. Nagai, T. Hara, K. Kimoto, Y. Matsui, Y. Onose, and Y. Tokura, Nat. Commun. **3**, 988 (2012).

[33] J. Iwasaki, M. Mochizuki, and N. Nagaosa, Nat. Nanotechnol. **8**, 742 (2013).

[34] F. Jonietz, S. Mühlbauer, C. Pfleiderer, a Neubauer, W. Münzer, a Bauer, T. Adams, R. Georgii, P. Böni, R. a Duine, K. Everschor, M. Garst, and a Rosch, Science **330**, 1648 (2010).

[35] G. Meier, M. Bolte, R. Eiselt, B. Krüger, D.-H. Kim, and P. Fischer, Phys. Rev. Lett. **98**, 187202 (2007).

[36] R. Allenspach, in *MRS Bull.* (2006).

[37] S. S. P. Parkin, M. Hayashi, and L. Thomas, Science **320**, 190 (2008).

[38] A. Fert, V. Cros, and J. Sampaio, Nat. Nanotechnol. **8**, 152 (2013).

[39] N. Romming, C. Hanneken, M. Menzel, J. E. Bickel, B. Wolter, K. von Bergmann, A. Kubetzka, and R. Wiesendanger, Science **341**, 636 (2013).

[40] S. S. P. Parkin, M. Hayashi, and L. Thomas, Science **320**, 190 (2008).

[41] L. Angeles, Sci. Am. 50 (1994).

[42] G.Gruner, Rev. Mod. Phys. **60**, 1129 (1988).

[43] G.Gruner, Rev. Mod. Phys. **66**, 1 (1994).

[44] H. Search, C. Journals, A. Contact, M. Iopscience, and I. P. Address, J. Physics-Condensed Matter **1347**, (1997).

[45] T. E. Mason, C. P. Adams, S. A. M. Mentink, E. Fawcett, A. Z. Menshikov, and C. D. F, Phys. B **238**, 449 (1997).

[46] L. M. Corliss, J. M. Hastings, W. Kunnmann, R. Thomas, and J. Zhuang, Phys. Rev. B **31**, (1985).

[47] A.Z.Menshikov, J. Magn. Magn. Mater. **73**, 211 (1988).

[48] E. Fawcett, Rev. Mod. Phys. **66**, 25 (1994).

[49] E. Fawcett, Rev. Mod. Phys. **60**, 209 (1988).

[50] G.Gruner, *Density Waves in Solids* (Westview Press, 2000).

[51] C. P. Adams, J. Physics-Condensed Matter **9**, (1997).

[52] K. Seo, H. Yoon, S. Ryu, S. Lee, Y. Jo, M. Jung, J. Kim, Y. Choi, and B. Kim, ACS Nano **4**, 2569 (2010).

[53] J. M. Higgins, R. Ding, J. P. DeGrave, and S. Jin, Nano Lett. **10**, 1605 (2010).

[54] A. Pokhrel, Z. P. Degregorio, J. M. Higgins, S. N. Girard, and S. Jin, (2013).

[55] R.-Q. Zhang, Y. Lifshitz, and S.-T. Lee, Adv. Mater. **15**, 635 (2003).

[56] J. Niu, J. Sha, and D. Yang, Phys. E Low-Dimensional Syst. Nanostructures **23**, 131 (2004).

[57] L. Z. Pei, Y. H. Tang, Y. W. Chen, C. Guo, W. Zhang, and Y. Zhang, J. Cryst. Growth **289**, 423 (2006).

[58] S. A., ASM Alloy Phase Diagr. Database (2008).

[59] G. K. Celler and L. E. Trimble, Appl. Phys. Lett. **54**, 1427 (1989).

[60] M. Uematsu, H. Kageshima, Y. Takahashi, S. Fukatsu, K. M. Itoh, and K. Shiraishi, Appl. Phys. Lett. **85**, 221 (2004).

[61] M. Uematsu, H. Kageshima, Y. Takahashi, S. Fukatsu, K. M. Itoh, K. Shiraishi, and U. Gösele, Appl. Phys. Lett. **84**, 876 (2004).

[62] N. Wang, Y. F. Zhang, Y. H. Tang, C. S. Lee, and S. T. Lee, Appl. Phys. Lett. **73**, 3902 (1998).

[63] S. Jin, M. J. Bierman, and S. a. Morin, J. Phys. Chem. Lett. **1**, 1472 (2010).

[64] E.Yablonovitch, Phys. Rev. Lett. **57**, (1986).

[65] Z. T. Zhang, D. A. Blom, Z. Gai, J. R. Thompson, J. Shen, and S. Dai, J. Am. Chem. Soc. **125**, 7528 (2003).

[66] Z. Gai, X.-G. Zhang, I. Kravchenko, S. Retterer, and J. Wendelken, Phys. Rev. B **85**, 024401 (2012).

[67] S. M. Stishov, Physics-Uspekhi **54**, 1117 (2011).

[68] K. Seo, H. Yoon, S. Ryu, S. Lee, Y. Jo, M. Jung, J. Kim, Y. Choi, and B. Kim, ACS Nano **4**, 2569 (2010).

[69] R. Ritz, M. Halder, C. Franz, A. Bauer, M. Wagner, R. Bamler, A. Rosch, and C. Pfleiderer, Phys. Rev. B **87**, 134424 (2013).

[70] C. Thessieu, J. Physics-Condensed Matter **6677**, (1997).

[71] B. Lebech, P. Harris, J. S. Pedersen, K. Mortensen, C. L. Gregory, N. R. Bemhoeft, M. Jermy, and S. A. Ibrown, J. Magn. Magn. Mater. **144**, 119 (1995).

[72] a. Bauer, M. Garst, and C. Pfleiderer, Phys. Rev. Lett. **110**, 177207 (2013).

[73] H. Yoon, J. Phys. Chem. Lett. 956 (2011).

[74] H. Yoon, J. Am. Chem. Soc. 17447 (2010).

[75] D. D. V. Ii, D. Sun, J. A. Moyer, A. J. Biacchi, R. Misra, P. Schi, and R. E. Schaak, (2013).

[76] M. Richardson, Acta Chem. Scand. **21**, 2305 (1967).

[77] K. E., ASM Alloy Phase Diagr. Database (1990).

[78] K. Kanematsu, J. Phys. Soc. Japan **20**, (1965).

[79] K. Kanematsu, J. Phys. Soc. Japan **20**, (1965).

[80] T. Sekine, N. Satoh, M. Nakazawa, and T. Nakamura, Phys. Rev. B **70**, 214201 (2004).

[81] G. Blumberg, P. Littlewood, a. Gozar, B. S. Dennis, N. Motoyama, H. Eisaki, and S. Uchida, Phys. C Supercond. **388-389**, 227 (2003).

[82] R. K. Kummamuru and Y.-A. Soh, Nature **452**, 859 (2008).

[83] K. W. Kim, a Pashkin, H. Schäfer, M. Beyer, M. Porer, T. Wolf, C. Bernhard, J. Demsar, R. Huber, and a Leitenstorfer, Nat. Mater. **11**, 497 (2012).

[84] S. Tan, Y. Zhang, M. Xia, Z. Ye, F. Chen, X. Xie, R. Peng, D. Xu, Q. Fan, H. Xu, J. Jiang, T. Zhang, X. Lai, T. Xiang, J. Hu, B. Xie, and D. Feng, Nat. Mater. **12**, 634 (2013).

[85] J. Chang, E. Blackburn, a. T. Holmes, N. B. Christensen, J. Larsen, J. Mesot, R. Liang, D. a. Bonn, W. N. Hardy, a. Watenphul, M. V. Zimmermann, E. M. Forgan, and S. M. Hayden, Nat. Phys. **8**, 871 (2012).

VITA

Siwei Tang, his parents only child, was born in Cili, ZhangJiajie city, Hunan province, China. In 1999, he attended the high school of MingZu in Zhangjiajie and then graduated at 2002. He obtained his bachelor degree of Measurement and Control Technology and Instrumentation Program from Information College of Central South University in 2006. He changed his major to materials science in 2006 and joined the department as a graduate student. In 2009, he went abroad to United States and studied as a graduate research assistant. He got his master of science in 2011 and joined Dr Mandrus group as a Ph.D student. He spent a lot of time doing research with Dr Zheng Gai in Center for Nanophase Materials Science, Oak Ridge National Lab.